공학박사 학위논문

Effect of Microstructure and Microtexture on the High Temperature Oxidation Behavior of Heat Resistant Stainless Steels

내열 스테인리스강에서 고온 산화 거동에 미치는
미세조직 및 집합조직의 영향 고찰

2015년 8월

서울대학교 대학원
재료공학부
김 주 헌

Effect of Microstructure and Microtexture on the High Temperature Oxidation Behavior of Heat Resistant Stainless Steels

내열 스테인리스강에서 고온 산화 거동에 미치는
미세조직 및 집합조직의 영향 고찰

지도교수 이 경 우

이 논문을 공학박사학위논문으로 제출함
2015년 8월

서울대학교 대학원
재료공학부
김 주 헌

김주헌의 박사학위논문을 인준함
2015년 6월

위	원 장	김 영 운 (인)
부 위	원 장	이 경 우 (인)
위	원	한 흥 남 (인)
위	원	김 희 산 (인)
위	원	김 동 익 (인)

Abstract

Effect of Microstructure and Microtexture on the High Temperature Oxidation Behavior of Heat Resistant Stainless Steels

Kim Ju-Heon
Department of Materials Science and Engineering
The Graduate School
Seoul National University

Despite enormous research efforts into the renewable energy technologies, conventional thermal power plants are still by far the most important power generation source worldwide; thermal power plants are expected to maintain this position for at least several decades. All power generation sources based on the fossil fuel burning inevitably produce CO_2, one of the major causes of global warming. Considering the contribution to the total CO_2 emission, improving fossil fuel-based energy conversion efficiency to 60% by increasing the reaction temperature is the most efficient way to reduce total CO_2 emissions by up to 30%.

Generally, the austenitic steels demonstrate excellent high temperature

creep properties, making them a promising candidate for use in steam tubes for superheaters and reheaters of ultra-super-critical (USC) power plants. Previous studies have shown that adding Cu to austenitic stainless steels increases the creep rupture strength and enhances high temperature corrosion resistance. To examine the oxidation behavior of Cu added austenitic stainless steels in a water vapor atmosphere, we observed the oxidation behavior at 700 ℃ in air with 20 % water vapor. Samples were prepared by thermo-mechanical treatment to have similar $\sum 3$ grain boundary fraction and different grain size, to eliminate the grain boundary characteristics effect.

The early stages (< 12 h) of the oxidation behavior of Cu added austenitic stainless steels with various grain sizes was investigated using atom probe tomography (APT), transmission electron microscopy (TEM), scanning electron microscopy (SEM), electron backscattered diffraction (EBSD), electron probe microanalyzer (EPMA) and X-ray diffraction (XRD). A thin Cr-rich oxide layer is formed over the entire surface of a small grain (8 μm) sample, which is similar to that formed near grain boundaries of medium grain (17 μm) and large grain (27 μm) samples. Oxidation of all samples proceeds via the lattice and grain boundary diffusion of Cr, leading to the formation of a protective Cr-rich oxide first at the grain boundaries and then via lateral growth toward the grain interiors. APT and TEM studies on the initial stage of oxidation clearly reveal that within 4 μm of the grain boundaries, the oxide layer exhibits a duplex-layer structure consisting of a thin Fe-rich $(Fe,Cr)_3O_4$

oxide (~55 nm) above and a protective Cr_2O_3 oxide (~40 nm) below as a diffusion barrier. In contrast, further away from the grain boundaries, a non-protective Fe-rich $(Fe,Cr)_3O_4$ oxide (~160 nm) and a Cr-rich $(Fe,Cr)_3O_4$ oxide (~40 nm) are formed as the outer and inner layers, respectively. The oxidation kinetics was studied in terms of mass gain measurements. The critical grain size (< 8 μm) to prevent the formation of fast-growing, non-protective Fe-rich oxides is discussed based on the experimental findings. Through the calculation and experimental analysis, a critical grain size for the high oxidation resistance is suggested.

During the later stages (< 500 h) of the oxidation of Cu added austenitic stainless steels with grain size smaller than 8 μm, uniform Cr_2O_3 layer was formed, which increased the overall oxidation resistance. Whereas in samples with grain size larger than 17 μm, Fe_2O_3 layer was formed on the Cr-rich oxide layer, which resulted in a relatively high oxidation rate. It can be inferred that the grain boundaries act as rapid diffusion paths for Cr and provide Cr enough to form Cr_2O_3 oxide at the area near to the grain boundary.

Also, the oxide scales of high-alloyed steel are composed of complex phases that are difficult to differentiate. Here, we used electron backscatter diffraction (EBSD)-electron dispersive spectroscopy (EDS) simultaneous analysis technique to analyze the complex oxide layers formed on Cu added austenitic stainless steels. Multi-layered oxide scales composed of external Fe_2O_3, external Fe_3O_4, internal $FeCr_2O_4$, and internal Cr_2O_3 oxide were well

distinguished. The addition of Cu to the austenitic stainless steel induced spinel structured oxide formation at the top surface of the external oxide.

We have studied the phase transformation behavior of the austenite (γ) to ferrite (α) in Cu added austenite stainless steel after oxidation at 700 ℃ in air with 20% water vapor. Identification and observation of the phase transformation have been carried out on this steel by means of SEM, XRD, TEM and APT with Thermo-Calc program, respectively. The results of SEM, XRD and TEM reveal that α-BCC phase formed along the prior γ-FCC grain boundary after oxidation. According to the APT result, Fe and Ni are strongly concentrated and Cr is depleted in α-BCC phase.

Oxidation behavior of ferritic stainless steels with 22 wt.% Cr was also investigated. The ferritic stainless steels have been preferred as a material for interconnects in solid oxide fuel cells (SOFC) because of their high electrical and thermal conductivity, good mechanical properties, good formability, cost effective and similar thermal expansion coefficient (TEC) to the other cell components. The SOFCs usually operate in the temperature in an intermediate range of 650~800 ℃.

The aim of this part is the study of the effect of crystallographic orientation on the high temperature oxidation behavior of ferritic stainless steels including Crofer 22 APU. Crofer 22 APU, specially developed for SOFC interconnect, was tested in an air atmosphere at 800 ℃. To gain a better understanding of the relation between oxidation resistance and electrical

conductivity, the oxide scales formed on surface was analyzed in terms of orientation, structure, composition and phase in the {100}, {110}, {111} and {112} substrate planes. Also, a nano-indenter with nanoscale electrical contact resistance (nano ECR) measurements has been used to study the changes in contact resistance during an oxidation. Oxide thickness and electrical contact resistance results showed that the surface orientation can have an effect on the oxidation resistance and electrical conductivity.

Keywords: Austenitic stainless steel, Ferritic stainless steel, Heat resistant steel, High temperature oxidation, Oxidation resistance, Grain size effect, Orientation effect, Material characterization, Electron backscatter diffraction, Atom probe Tomography

Student Number: 2010-20589

Contents

List of Tables

List of Figures

Chapter 1

Literature Review of High Temperature Oxidation

1.1 General mechanism of oxidation

1.1.1 Principles of oxidation

The general total chemical equation for an oxidation reaction between a metal (*M*) and oxygen (O_2) gas is shown below;

$$M(s) + 1/2O_2(g) \rightarrow MO(s) \qquad \text{(Equation 1.1)}$$

It is the simplest equation but it depends on a variety factors and can become more complex [1].

The initial step in the metal-oxygen reaction involves the adsorption of gas on the clean metal surface. During the reaction, the adsorbed oxygen dissolves in the metal and the oxide forms as a continuous oxide film or as separate oxide nuclei. The solid reaction product (metal oxide) divides the two reactants, and for the reaction to continue further, one or both reactants have to

penetrate the oxide layer (scale) by solid-state diffusion. This can happen by either oxygen going through to the oxide-metal interface and reacting there or the metal being transported through the oxide to the oxide-gas interface and reacting there as shown in Figure 1.1 [2]. For thin compact scales, the reason for transport through the oxide may be due to the electric fields across the film, and for thick films it is due to chemical potential gradient across the scale. Porous oxides scales are limited by solid-state diffusion and can be restricted to diffusion occurring at phase boundaries or mass transport occurs through gas diffusion. Oxide layers at high temperatures may be volatile or liquid [1].

1.1.2 The initiation of oxidation

The adsorption of gas onto the metal surface is the initial stage of oxidation. This process involves a decrease in free energy and entropy which means enthalpy decreases and makes this process normally exothermic. There are two adsorption, physical adsorption and chemical adsorption. Physical adsorption involves physical or van der Waals forces bonding the gases to the surface and is reversible [3]. Chemical adsorption (chemisorption) involves the adsorbed species forming a chemical bond with surface atoms via the transfer of electrons. Chemisorption tends to take place at higher temperatures and may involve an activation energy. Very rapid chemisorption can be seen with gases and clean metals where there appears to be no activation energy. It continues only until a monolayer of the adsorbent is created on the surface [1].

After the adsorption where the surface has been covered by chemisorbed oxygen, isolated oxide nuclei nucleate at random points for instance at impurity atoms, surface imperfections etc. on the metal surface. The growth of individual crystallites enables the oxidation of the surface to continue until oxide patches grown from individual nuclei connect and the entire surface is covered with oxide which acts as a diffusion barrier [1, 4].

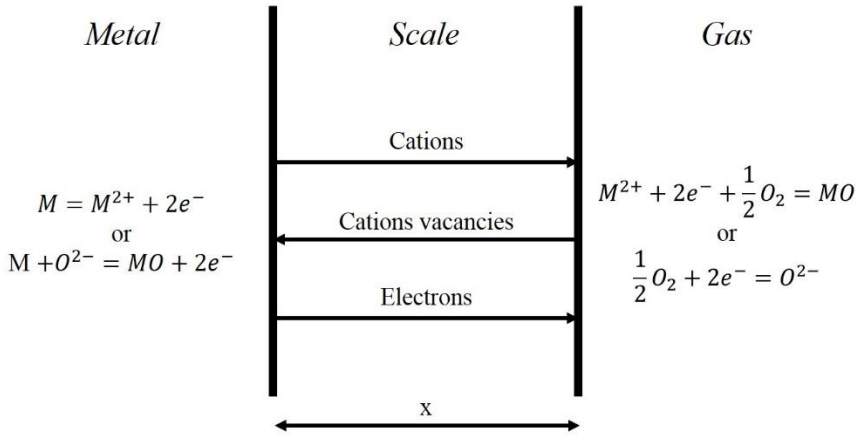

Figure 1.1 Schematic illustration of a simplified model for diffusion-controlled process of oxidation where the cations and cation vacancies have to penetrate the oxide scale for the reaction to continue [2].

1.1.3 Transport mechanisms

The formed oxide separates the metal from the gas and the only way for oxidation to proceed is via solid-state diffusion of the reactants. This type of diffusion can only take place due to the presence of defects in the oxide structure. Point defects such as vacancies, interstitial atoms and misplaced atoms are required for solid-state diffusion in the oxide [1, 4]. Scale growth occurs by the cations and anions diffusion. Cation diffusion causes oxide formation at the oxide-gas interface whereas anion diffusion leads to oxide formation at the metal-oxide interface as shown in Figure 1.2. Oxides can show non-stoichiometry and either mainly contain cation defects or mainly contain oxygen defects.

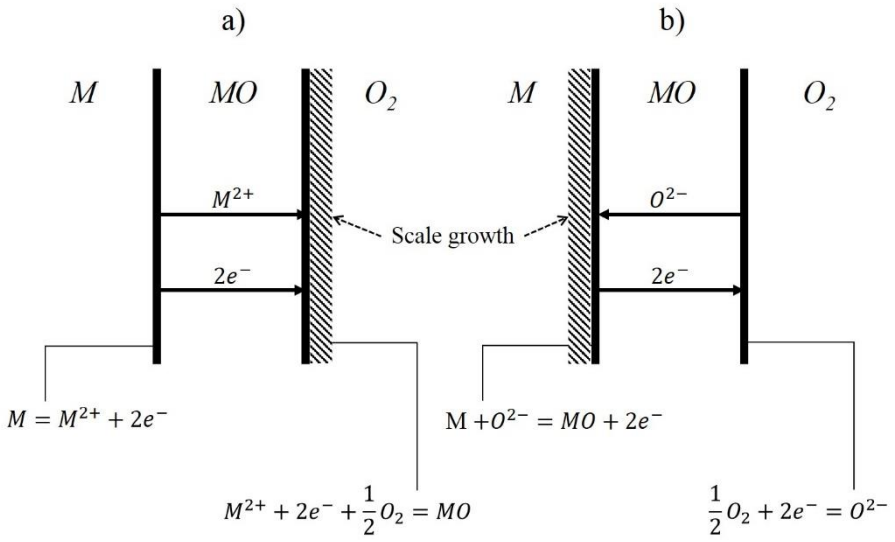

Figure 1.2 Schematic illustration of high temperature oxidation mechanisms, showing the reactions at the metal interface and transport routes of ions; a) cation mobile, b) anion mobile [2].

1.1.4 Rate of oxidation

The rate of oxidation can be measured experimentally by using three methods. These involve measuring the amount of metal consumed oxygen consumed, the amount of oxygen consumed and the amount of oxide produced. The method used to find the amount of metal consumed is the least preferable as it is a destructive method which is indirect and not continuous. The method chosen in this study is to record the amount of oxide produced by observing the weight of oxide formed or measuring the oxide thickness. All of these variables are measured as a function of time to show the rate of oxidation [2]. From experimental data three main rate laws have been observed as follows;

1) The linear rate law: this is where the rate of reaction is constant with time and independent of the quantity of metal or gas consumed up to that time. The initial surface reaction step (adsorption) or the diffusion through the gas phase controls the oxidation process. The linear rate law can be observed at the very initial stages of oxidation when the metal surface is exposed to the atmosphere for the first time. It can be described by the following equation;

$$x = k_l t \qquad \text{(Equation 1.2)}$$

where x is the scale thickness, k_l is the linear rate constant and t is the time [2].

2) The parabolic rate law: this is where the rate of reaction is inversely proportional to the square root of time [2]. At high temperatures many metals show this rate law where the diffusion of ions, either metal or gas, through the compact scale is the rate determining process [1]. The parabolic law can be described by the following equation;

$$x^2 = 2k't \qquad \text{(Equation 1.3)}$$

where k' is the scaling constant [2].

These two laws can be displayed graphically so the oxidation kinetics can be observed easily as shown in Figure 1.3.

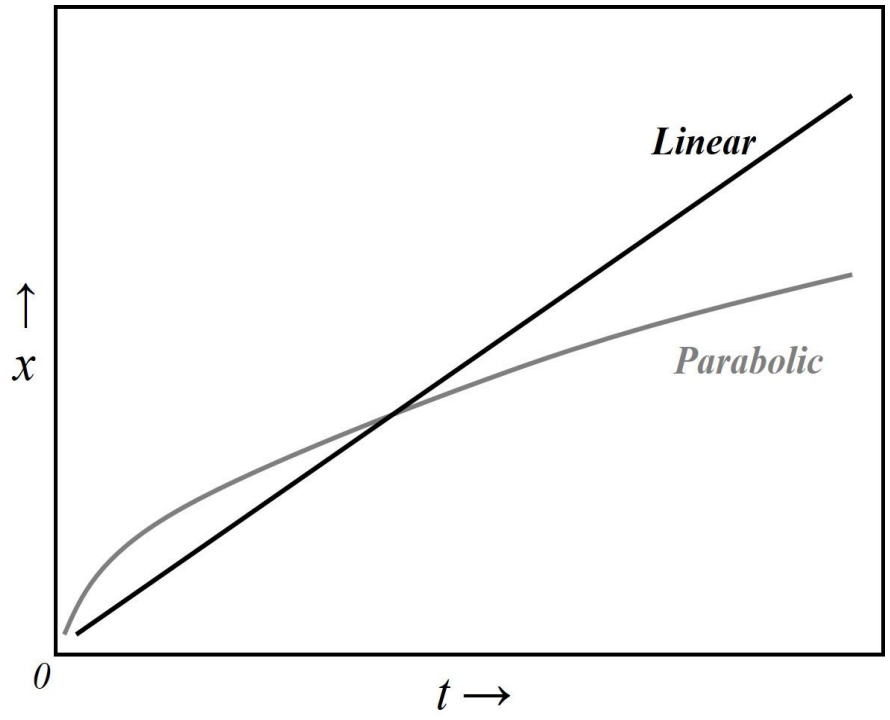

Figure 1.3 The linear and parabolic oxidation where oxide growth (x) as a function of time (t) [1].

3) The logarithmic rate law: this is characteristic of the oxidation of a lot of metals at low temperatures (up to about 400 ℃) and for the formation of very thin oxide films (up to 100 nm thick) [3]. The rapid reaction starts off and then slows down as it proceeds, this rate law can be described by two equations;

Direct log law: $x = k_{log}\, log(t + t_0) + A$ (Equation 1.4)

Inverse log law: $\frac{1}{x} = B - k_{il} log t$ (Equation 1.5)

where k_{log} and k_{il} are rate constants and *A* and *B* are constants [1].

These laws can also be shown graphically as seen in Figure 1.4.

Oxidation reactions frequently tend to follow a mixture of different rate laws as described above. This is due to the rate determining mechanisms changing during the reaction due to the scale itself changing or the reaction having simultaneous mechanisms and one dominating at the initial stage and

then the other mechanism taking over later on [1]. For example, this is the transition from linear to parabolic law. The reaction starts at constant rate when the oxide is just forming and is diffusion through the thin film is very fast. Here the surface reaction is the rate determining mechanism. As oxidation continues and the scale becomes thicker there is less ion flux through the scale and the reaction rate decreases. The diffusion of ions through the oxide is now the rate determining step and the rate decreases as the reaction proceeds displaying the parabolic law [2].

The parabolic relationship is the most desirable as the oxide formed is slow growing and less likely to spall. This relationship is shown by 'OAD' curve in Figure 1.5. However, depending on conditions (alloy composition, time and environment) breakaway oxidation can occur where there is a sudden increase in the growth rate shown by 'AB' curve [5]. In the case of stainless steels, this is where Fe-rich oxides are forming instead of chromia (Cr_2O_3) due to alloy depletion as discussing later. The growth of oxide can continue shown by 'BE' curve, possibly due to the volatilization environment of the oxide occurs or from cracking in the scale leading to additional outbursts of quick oxidation [5]. Alternatively, if a protective oxide reforms, the oxidation rate can decrease again by 'BC' curve.

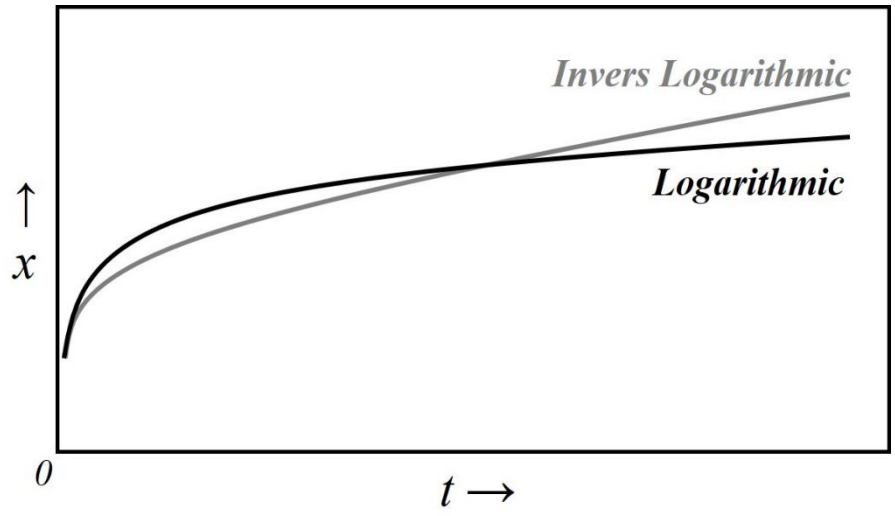

Figure 1.4 The logarithmic and inverse logarithmic oxidation kinetics where oxide growth (x) as a function of time (t) [1].

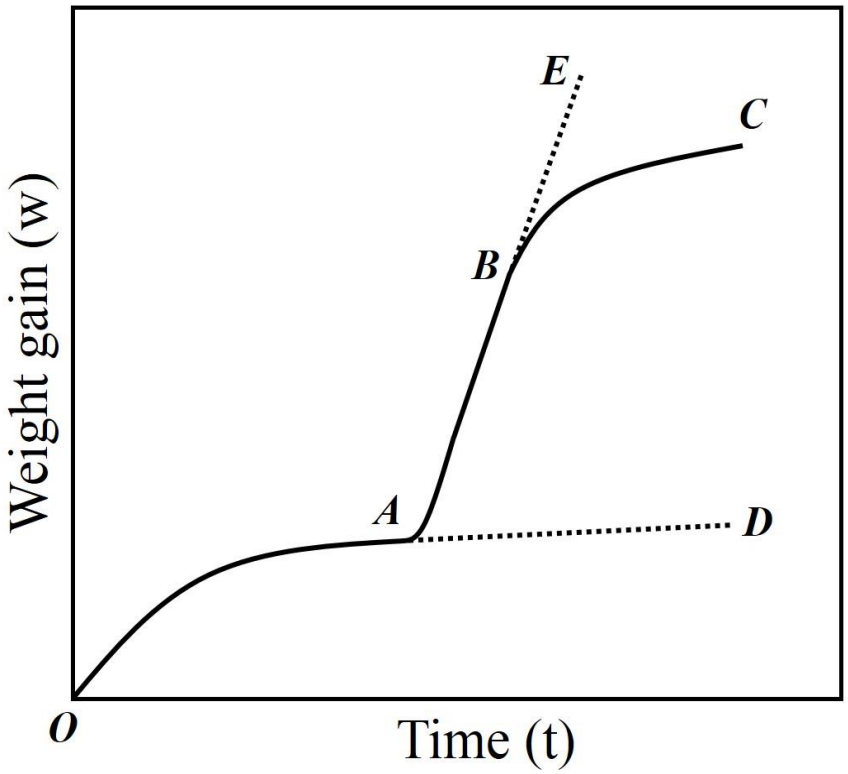

Figure 1.5 Typical Fe-Cr alloys and stainless steels oxidation kinetics [6].

1.1.5 Oxidation of alloys

All of the principles that have been described previously have been for oxidation of pure metals but this theory can also be applied to the oxidation of alloys. However, alloy oxidation can be a lot more complex due to the metals in the alloy having different affinities to oxygen because of the different free energies of formation of the oxides. The different metals will also show various diffusivities in the alloy and their ions will have different mobilities in the oxide phases [2]. This makes the prediction of oxidation behavior much more difficult for alloys.

To have effective oxidation resistance the alloy needs to form a continuous scale by outer oxidation. Ineffective protection can occur by precipitates forming inside the alloy during oxidation, this is called inner oxidation [3]. To achieve effective oxidation resistance, alloys aim to form compact scales with small rates of diffusion of the reactant ions [1].

The oxidation of alloys generally produces more than one oxide. Selective oxidation occurs where the least noble constituent of alloying components in the alloy is oxidized first to form the outer protective layer [1]. The alloying components have oxides which demonstrate large differences in stability; however, the temperature, partial pressure of the oxygen and concentration of the active alloying components also affect selective oxidation

[1]. Selective oxidation has led to alloys being designed to have certain alloying additions in them to increase their oxidation resistance in high temperature applications. However, adding components that help form protective oxide scales tends to have a negative effect on other alloy properties such as mechanical properties and so these element additions need to be as low as viably possible [2]. Cr (chromia scale), Al (alumina scale) and Si (silica scale) are the three main elements that when added constantly form protective scales. Their oxides have the lowest diffusion rates making them the optimum protective oxides [2]. For most commercial high temperature alloys, the base metal consists of Fe, Ni or Co which all form moderately stable oxides, and additional alloying elements such as Cr, Al and Si which form highly stable oxides [2]. Si additions have been found to reduce the weld ability and toughness of steels and Ni-based alloys, and so its concentration has to be limited to reduced levels where the formation of silica alone cannot be attained [7].

Fe-Cr alloys are a very common commercial alloy for high temperature applications. When there are small concentrations of Cr in the alloy both Fe and Cr-rich oxides form on the surface. The Cr solubility in the FeO phase is limited and so only some Cr will enter this phase [2]. If the Cr content is increased in the alloy the Fe^{2+} ions are blocked by the $FeCr_2O_4$ islands so the FeO layer gets thinner compared to the Fe_3O_4 layer. At low Cr concentration, the reaction rate

is still quite low [2]. If the Cr content is further increased then the parabolic rate constant is lowered due to a scale of mixed spinel $Fe(Fe,Cr)_2O_4$ forming. Fe ions appear to be more mobile than Cr ions in this oxide because at longer durations pure Fe oxides are formed on the outer surfaces of the scale [2]. When the Cr content increases to a critical concentration the scale formed initially is Cr_2O_3 which reduces the parabolic constant further. This protective scale can only be formed at Cr concentrations which exceed this point. This is taken into consideration when designing heat resistant alloys such as stainless steels [2].

When designing the alloy and its composition for oxidation resistance the Ellingham diagram can be very helpful as it displays and compares the stability of the possible oxides forming under stated conditions. This helps show which elements in the alloy will oxidize preferentially over the others and which will oxidize next when the initial element becomes depleted. The Ellingham diagram shown in Figure 1.6 has different lines for different oxidation reactions. The lines represent the standard free energy of oxidation of pure metals versus time [3]. The lower the line on the diagram, the more stable the oxide formed is and the lower its dissociation partial pressure [2]. Cr, Si and Al are all low down in the diagram, below the Fe oxides, and they are all capable of forming stable protective oxides when present in the right concentrations in the alloys.

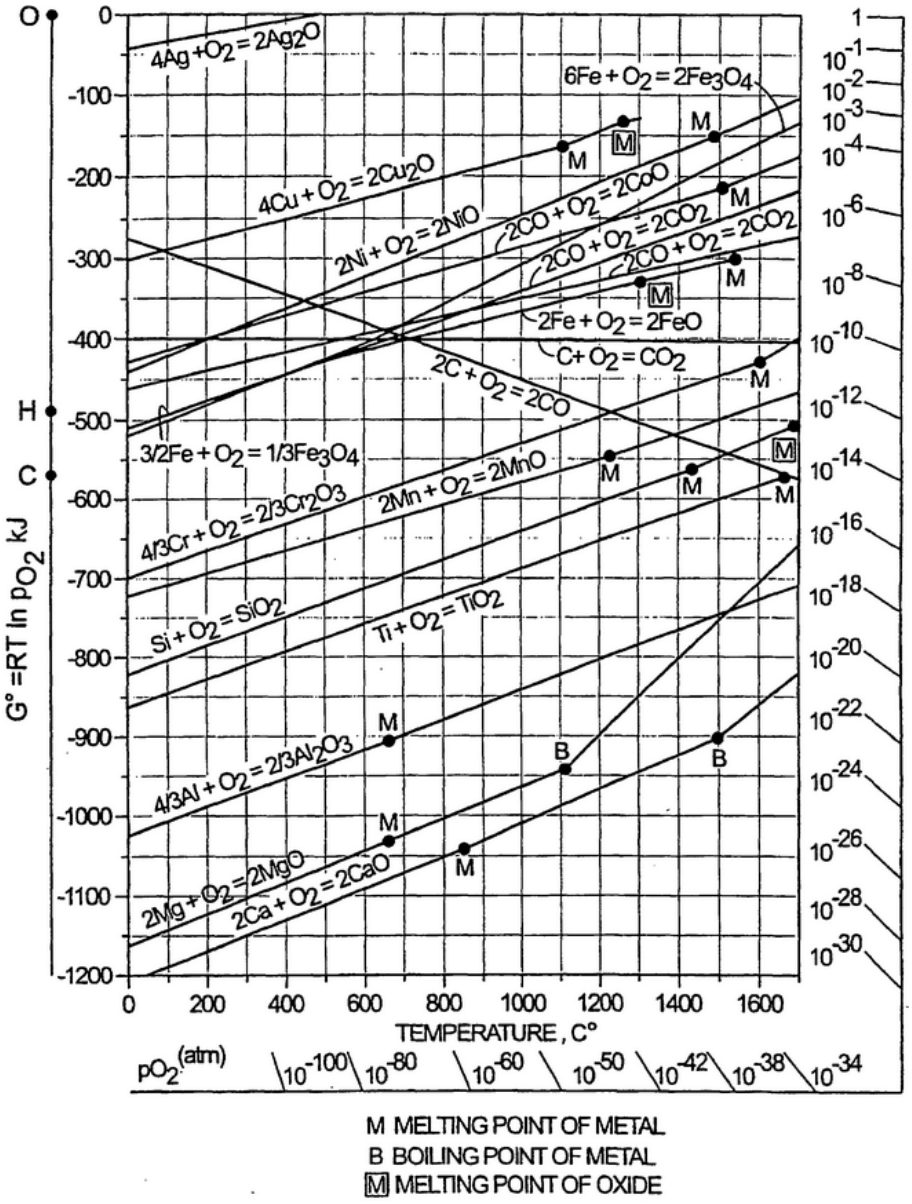

Figure 1.6 Ellingham diagram displaying standard free energy of common oxides [8].

1.1.6 Alloy depletion

As the oxidation reaction occurs at high temperature the oxide formation needs to be provided with a supply of the active elements from the substrate. If the active element is not in the adjacent area to the oxide then this will become the rate determining factor. The active element is consumed in the substrate during the reaction via diffusion towards the oxide. The region of substrate beneath the oxide layer then becomes depleted of this active element. Further depletion could lead to the protective oxide being unable to be maintained due to concentration of the active element becoming too low. This can lead to breakaway oxidation [9, 10].

The Cr depletion zone can have a positive effect on spallation resistance as this alloying can change the microstructure and therefore mechanical properties. If the depleted zone is weaker than the substrate then creep will occur here and reduce stresses built up from thermal cycling and thermal expansion coefficient mismatches. These relaxed stresses help prevent spallation [9].

1.2 Oxidation in water vapor and steam

Oxidation also occurs at high temperatures in water vapor and steam where the rate of reaction is greater than oxidation in air [4, 5]. The morphology of the scales has also been found to differ from air oxidation. Water vapor has been shown to encourage a more porous scale to form, which is linked to an increased cation diffusion, resulting in vacancy condensation forming the pores [11]. Water vapor has also been found to reduce the plasticity of these scales, but due to controversy in the literature the exact mechanism is unclear. The reduction in plasticity would make them more prone to spallation as they cannot relieve the induced stresses [5]. Another major difference from oxidation in air is the formation of the scale hydroxides (OH^-) and oxyhydroxides which are more volatile than the normal oxide causing the oxide to shrink and lose its protective properties [11, 12].

Water vapor affects the oxide growth at all stages of the oxidation process such as adsorption, dissociation and diffusion. Adsorption and dissociation of the water vapor occurs on the surface of the growing oxides and results in a more permeable scale forming. The pores in the oxide structure assist the rapid inward diffusion of oxygen to form oxide at the metal-scale interface and so the pores gradually move outwards to the scale-gas interface [11]. The presence of water vapor can also affect the mechanical properties of the scale such as increasing the oxide adhesion in Fe oxides and reducing it in

Al_2O_3 and Cr_2O_3. The reduced scale adherence of Al_2O_3 and Cr_2O_3 scales could be down to a change in growth processes or may just be down to increased scale thickness from the increased kinetics of oxidation [11]. Further understanding on steam oxidation is limited as the atmospheres required for the test are very hard to maintain and reproduce and in-service conditions such as those in a power plant are very hard to replicate [13].

1.2.1 Water vapor and steam oxidation mechanisms

As already stated, the oxidation of alloys in steam varies significantly in both kinetics and morphology to alloy oxidation in air or oxygen. The following five main mechanisms have been frequently used to explain the effect of water vapor on oxidation [13];

1. Dissociation mechanism
2. Oxidant-gas penetration mechanism
3. Formation and volatilization of iron (II) hydroxide ($Fe(OH)_2$)
4. Formation and volatilization of $CrO_2(OH)_2$
5. Proton dissolution induced changes in the oxide defect structure

However, any single mechanism alone cannot explain all of the observed metal oxidation behavior in the presence of water vapor [13].

1.2.1.1 The dissociation mechanism

This mechanism of oxidation in steam was proposed by Fujii and Meussner in 1964 [14, 15]. Reactions occur at interfaces 'II' and 'IV' seen in Figure 1.7, where metal ions are generated. Theses ions then diffuse to the outer interface between the oxide scale and wet atmosphere 'I'. Water vapor is adsorbed on the surface from the atmosphere and the resulting reactions with the metal ions produce FeO (wüstite), absorbed hydrogen and defects in the oxide. Some hydrogen dissolves but most of the hydrogen desorbs in the oxide [13].

The reactions from the adsorbed water vapor and metal ions at the oxide-atmosphere interface can be seen below

$$H_2O_{(g)} \rightarrow H_2O_{(ads)} \qquad \text{(Equation 1.6)}$$

$$H_2O_{(ads)} + Fe^{2+} + 2e^- \rightarrow {'FeO'} + Fe_{vac} + 2\oplus + H_{2(ads)} \qquad \text{(Equation 1.7)}$$

$$H_{2(ads)} \rightarrow H_{2(g)} \qquad \text{(Equation 1.8)}$$

$$H_{2(ads)} \rightarrow 2H^*_{(ox)} \qquad \text{(Equation 1.9)}$$

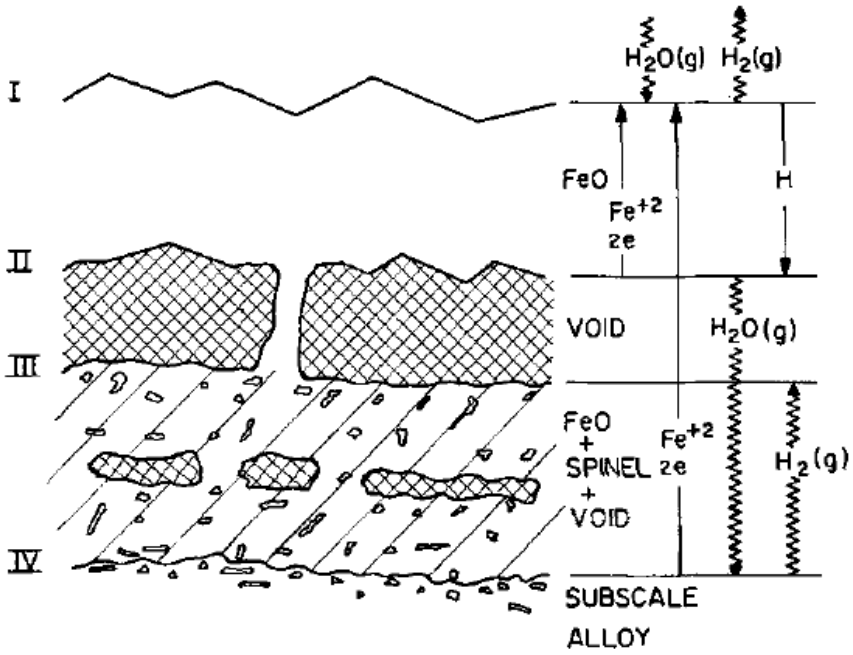

Figure 1.7 The dissociation mechanism for oxidation of Fe-Cr alloys in water vapor [14].

where the symbols Fe_{vac} and $\oplus$ signify a vacant Fe ion site and an electron defect respectively, and H^* is symbol for a hydrogen atom dissolved in the oxide [14].

At interface 'II', the dissociation of Fe oxide is thought to occur to produce an oxide ion as an absorbed species. The permeating hydrogen enables these adsorbed species to react to form the carrier gas for oxygen transport to the void [14]. This dissociation and gas formation is shown below;

$$FeO + Fe_{vac} + 2\oplus \rightarrow Fe^{2+} + O^{2-} \qquad \text{(Equation 1.10)}$$

$$2H^*_{(ox)} \rightarrow H_{2(ads)} \qquad \text{(Equation 1.11)}$$

$$H_{2(ads)} \rightarrow H_{2(gas)} \qquad \text{(Equation 1.12)}$$

$$H_{2(ads)} + O^{2-}_{(ads)} \rightarrow H_2O_{(g)} + 2e^- \qquad \text{(Equation 1.13)}$$

The resultant atmosphere and the reactions occurring at interfaces 'I' and 'II' cause wüstite layers to form on the outer scale, Figure 1.7. The wüstite reacts with spinel changing the composition of the spinel phase as seen below;

$$FeCr_2O_4 + 4FeO \rightarrow 2Fe_2CrO_4 + Fe^{2+} + 2e^- \qquad \text{(Equation 1.14)}$$

These observations and suggested mechanisms for the inner scale were made by Fujii and Meussner in 1964 from oxidation tests on Fe-Cr alloys up to 25 wt.% Cr in Ar-10%H_2O at temperatures of 700~1100 ℃ [14]. Figure 1.7 illustrates the one or multi-layered scale with the outer layer of wüstite, a middle porous scale containing wüstite and an Fe-Cr spinel oxide, and then an inner subscale of Fe-Cr spinel [13].

1.2.1.2 Oxidant-gas penetration mechanism

Another study compared the oxidation characteristics of Fe-Cr alloys containing up to 30 wt.% Cr, in dry and wet (O_2-10% H_2O) oxygen at 750 ℃ and 900 ℃. Ikeda and Nii performed this study in 1982 [16, 17] and found that the mass gain in wet oxygen was significantly greater than that in dry oxygen when the alloys had Cr contents of greater than 15 wt.%. They compared two possible reaction, i.e. the dissociation mechanism and the oxidant-gas penetration mechanism with the simple gas kinetics based calculation that the latter mechanism was more appropriate explanation. This more appropriate mechanism involves the oxygen and water vapor passing directly to the metal surface due to the development of microcracks and pores in the scale, assuming the numbers and size of cracks are numerous and large [13].

Initially, oxidation begins with a Cr_2O_3 layer forming and covering the surface of the alloy. Cracks and pores in this oxide enable gas to penetrate into a void which could increase the oxygen partial pressure within the void that oxidizing the Fe. The production of a mixed oxide scale which not be able to prevent outward diffusion of iron ions, which enables a fast growing Fe-rich outer oxide to form [13]. Gas penetration was also found to be more common in wet oxygen conditions rather than dry, and water vapor was suggested to increase oxidation by causing more common scale cracking and preventing it from healing [17].

1.2.1.3 Formation and volatilization of $Fe(OH)_2$

An alternative mechanism for the increased oxidation of Cr steels in the presence of steam and water vapor was suggested by Surman and Castle in 1969 [18, 19]. It involves the formation and volatilization of $Fe(OH)_2$. They suggested that the rate determining process could be one of three things;

1) The outward diffusion of iron cations to the oxide-gas interface

2) The inward diffusion of oxygen anions to the metal-oxide interface

3) Vapor-phase diffusion of $Fe(OH)_2$ to the oxide-gas interface [13]

The model was assumed that the phase boundary reactions, shown below, occur for the formation and dissociation of this volatile hydroxide.

At the metal-oxide interface;

$$Fe_{(s)} + 2H_2O_{(g)} \rightarrow Fe(OH)_{2(g)} + H_{2(g)} \qquad \text{(Equation 1.15)}$$

$$3Fe_{(s)} + 4H_2O_{(g)} \rightarrow Fe_3O_{4(s)} + 4H_{2(g)} \qquad \text{(Equation 1.16)}$$

At the oxide-gas interface;

$$Fe(OH)_{2(g)} \rightarrow Fe_3O_4 + 2H_2O_{(g)} + H_{2(g)} \qquad \text{(Equation 1.17)}$$

The experimental value and theoretical value were compared for the temperature dependence of the parabolic rate constant for each of the suggested rate determining processes. The vapor model gave the best agreement between theoretical and actual values and therefore considered as the most likely mechanism [13]. However, this Fe (II) hydroxide volatilization mechanism has caused some dispute over its validity due to similar work done on Ni and Co containing steels. Ni and Co containing outer oxides were expected due to the volatility of these element hydroxides being similar to that of iron hydroxide. However, neither of these elements was found in these outer oxides [13].

1.2.1.4 Formation and volatilization of $CrO_2(OH)_2$

It is proposed in this mechanism that the scale cracking and spallation of oxide scales in the presence of water vapor is due to the evaporation of volatile Cr species mainly along the grain boundaries [13]. A study was performed on Ni-Cr alloys in air and wet air by Armanet [20]. In both conditions Ni-20Cr formed three oxides; Cr_2O_3, NiO and $NiCr_2O_4$ spinal oxide. In the dry air, the NiO was gradually consumed in the reaction with Cr_2O_3 to form the spinel. In wet air, the NiO remained without reacting and considerable cracking and spalling was observed. It is suggested that the oxide layer bursts because of compounds rich in chromium exerting an over-pressure during volatilization [13]. Compressive stresses occur when the Cr_2O_3 layer is continuous causing failure in the NiO and $NiCr_2O_4$ layers. The Cr_2O_3 layer will now be in contact with the atmosphere and volatilize to CrO_3 and $CrO_2(OH)$ which depletes the alloy of Cr and now re-oxidizes as NiO and eventually spinel [13]. This process is continuous resulting in rapid oxidation. The following volatilization reactions take place and deplete the alloy of Cr [13].

$$Cr_2O_3 + 3/2\ O_2 \rightarrow 2CrO_{3(g)} \qquad \text{(Equation 1.18)}$$

$$Cr_2O_3 + O_2 + H_2O \rightarrow 2CrO_2(OH)_{(g)} \qquad \text{(Equation 1.19)}$$

$$2CrO_3 + H_2O \rightarrow 2CrO_2(OH) + 1/2\ O_{2(g)} \qquad \text{(Equation 1.20)}$$

1.2.1.5 Changes in the oxide defect structure via proton dissolution

The presence of water vapor could also affect the defect structure and properties of the oxide systems. Hydrogen source from the water vapor dissolves as protons in the metal oxide. Also, this affects majority-defect dominated properties, such as diffusion-controlled transport of reactants in the oxide layer and creep [13].

A study by Galerie also compared metals oxidized in air and water vapor, with the focus on the effect of major point defects and the effect that the acidity of the oxide surface had [21]. Water vapor was again found to enhance the metal oxidation when oxygen was the most mobile species in the oxide. Hydrogen solubility was also important in the metallic substrate as the metals most affected by water vapor had the greatest hydrogen solubility [21]. The rate-determining step is the transport of oxygen through the scale via hydroxyl defects. In steam the oxide surface is covered in hydroxyl species but has few oxygen species [22, 23]. Oxygen species are formed from surface OH species which become disassociated at the O-H bond. For this to occur the surface needs acidic properties and this study has shown that pure metal species that did not have an acidic oxide had very slow oxidation rates in water vapor [13]. Therefore it has been suggested that the decomposition of OH species controls the oxidation rate. For acidic oxides the rate of surface OH decomposition was

high enough to provide oxide ions to the scale as fast as they were being used up so decomposition rate does not limit oxidation rate [13].

1.2.2 Steam oxidation as a function of steel composition and alloy type

The oxidation of steels and other alloys can vary a great deal depending on composition of the alloy. Increasing the Cr content of steel can improve the oxidation resistance by enabling a protective oxide scale to form. During oxidation, carbon steels oxidize to form layers of wüstite (FeO), hematite (Fe_2O_3) and magnetite (Fe_3O_4) depending on the environment it is exposed to [13]. When Cr is added to the alloy, an Fe-Cr inner spinel layer is formed rather than an inner Fe oxide layer. This occurs for ferritic (< 3 wt.% Cr) and martensitic (9~12 wt.% Cr) steels. When the Cr content increases even further, such as austenitic stainless steels, an inner Cr_2O_3 layer is formed which is very protective against oxidation and reduces oxide growth [13]. However, the presence of water vapor slightly reduces this increased oxidation resistance effect of Cr additions. This reduction is due to the different morphology of the oxide scales produced in water vapor such as macroscopic defects like pores and cracks [13]. Studies have shown that if the Cr content is increased to up to 25 wt.% Cr, then an inner Cr_2O_3 layer is formed at a fast rate, which slows the diffusion of Fe through the scale to form magnetite at the gas-oxide interface [24]. However, it has been found that there is an upper limit for the amount of Cr additions that is favorable to oxidation resistance as the effect reaches a table with increasing Cr content [13].

1.3 Stainless steel

1.3.1 Properties

Stainless steel contains at least 11 wt.% of Cr [25]. The amount of Cr depends on the specific usage of every type of stainless steel. They are solid with high strength of covalent bond. Stainless steel which is not a good conductor has a high resistant to corrosion by forming a passive film. Since this layer is very thin, it is not very visible. When this passive film is scratched, it will reform quickly. The passive film avoids the diffusion of oxygen so that it is not easy to corrode when compared with iron and carbon steel. Carbon steel will form oxide easily when exposed in air and humidity condition.

Different from stainless steel, stainless alloy consists of two or more elements. Some stainless alloys with higher resistance to corrosion consist of elements such as Ni, Mo and Al which form the stable oxide or hydroxide that can enhance the corrosion resistance of stainless alloys [26]. For alloys with the addition of Al, a good passive film of Al_2O_3 or aluminum hydroxide ($Al(OH)_3$) will be formed. . The advantage of the passive film is its low growth rate that makes stainless alloys stable enough to avoid the diffusion of oxygen with high efficiency. Thus, it is not easy for stainless alloys to corrode.

1.3.2 Classification

There are four types of stainless steel: austenitic stainless steel, ferritic stainless steel, martensitic stainless steel and duplex stainless steel [25]. They are classified by their crystalline structure. The details of only two kind of stainless steel are shown next page.

1.3.2.1 Austenitic stainless steels

Austenitic stainless steel contains at least 16 wt.% Cr and 7~20 wt.% Ni, and the crystal structure is a face-centered cubic (FCC) [25]. The presence of Ni is to retain its structure at room temperature. Resistance corrosion is the highest when comparing with other types of stainless steel. Also, it is formable and widely used in food processing industries, power plants, chemical industries and paper industries. The common type is 304 (Fe-18Cr-8Ni) and 316 (Fe-16Cr-8Ni-2Mo) stainless steel. They have a high strength and corrosion resistance.

The austenitic stainless steels are more expensive than the ferritic stainless steels due to the increased alloying additions. They have poor thermal conductivity and larger thermal expansion coefficients which restricts their applications, and so they are mainly used in the hotter sections of the superheater and reheater tubes in the high temperature boiler [13]. Fatigue cracking can result from high thermal stresses and oxide scale spallation can occur due to their thermal expansion coefficients. They are also used in the areas where corrosion induces problems to repair and provide protection for low alloy steels. The increased Cr in the matrix provides enhanced oxidation/corrosion resistance [13].

The steels with higher Cr contents exhibit lower parabolic rate constants

[13]. The calculations were made assuming that Cr_2O_3, Fe_3O_4 and FeO were all formed and then this theoretical data was compared with the actual experimental values [27]. Environments with high pressure cause increased oxidation rates as the reliability of the oxide is injured due to voids and cavities forming. Similar to martensitic alloys, increased Si content enhances oxidation resistance by forming an inner SiO_2 layer which has a slow growth rate and reduces Cr diffusion acts as a diffusion barrier and therefore Cr consumption decrease and Cr depletion formed slowly in the substrate [13].

The influence of grain size of the steam oxidation of austenitic steels has also been investigated [28, 29]. Fine grained steels have enhanced oxidation resistance over the equivalent course grained steels. As stated previously, this effect is down to the faster diffusion of Cr ions along the grain boundaries to the surface which reduces local depletion below the scale [13].

1.3.2.2 Ferritic stainless steels

Ferritic stainless steels contains 12~30 wt.% Cr and very little NI, and the crystal structure is body-centered cubic (BCC) [25]. Sometimes, Mo, Al or Ti can be included in ferritic stainless steel.

Low alloy ferritic steels have good tensile strength at lower temperatures (< 450 ℃), good creep strength at temperatures below 550 ℃ and outstanding weldability with no need for post heat treatment [13]. These properties make them useful for tubing alloys in pressurized applications such as boilers and heat recovery steam generators (HRSGs). They are used in the cooler regions of superheater and reheater pipes [13]. The main downfall in their material properties is the poor oxidation resistance in steam. Therefore, ferritic steels can only be used at lower temperatures which reducing plant efficiency.

Steam oxidation of ferritic stainless steels produces three oxide layers; a subscale region with internal oxide precipitates, a thick compact outer layer and a thin layer between the two [13]. Steam side oxidation of ferritic boiler tubes has produced multilayered scales on the inner side of the tubes. Scales consisting of Fe_3O_4 and Fe_2O_3 form at temperatures below 560 ℃. At increased temperatures FeO is formed and when the steel is alloyed a spinel oxide will form $(Fe, Cr, Mo)_3O_4$ [13].

$$2Fe_{(s)} + O_{2(g)} = FeO_{(s)} \qquad \text{(Equation 1.21)}$$

$$6FeO_{(s)} + O_{2(g)} = Fe_3O_{4(s)} \qquad \text{(Equation 1.22)}$$

$$4Fe_3O_{4(s)} + O_{2(g)} = 6Fe_2O_{3(s)} \qquad \text{(Equation 1.23)}$$

The flow rate of the steam is also found to affect the oxidation rate of the ferritic steels. When in contact with flowing steam a parabolic growth rate was observed at temperatures below 600 ℃, but in stagnant steam the followed a cubic rate law [13]. The kinetics were also seen to vary with temperature. The growth rate obeys the parabolic law below 600 ℃ which show the steel is self-protecting. When the temperature increases above this the scale is no longer protective as the oxidation rate turns linear [13], which is why this type of steel is not used at these high temperatures. Another factor affecting the oxidation of these alloys is the method used to create the steam environment as it has been found to both increase or decrease the corrosion rate [13].

Chapter 2

Characterization Techniques for Oxidation Analysis

2.1 Scanning electron microscope

The scanning electron microscope (SEM) image is formed using a focused electron beam that scans over the surface area of a sample. When a solid sample is irradiated by an electron beam in the SEM (usually in the voltage range of 1 to 30 kV), different kinds of signals are generated as shown in Figure 2.1 a), for example, secondary electrons (SEs), backscattered electrons (BSEs) and characteristic X-rays, which are utilized to obtain different information of the sample. SEs are the collection of the escaping electrons which were originally bounded as the outer shell electrons of the atoms in the sample, which receive sufficient kinetic energy during inelastic scattering of the incident electrons and are ejected from the atom. In practice, SEs signals are adopted to achieving the topographic contrast in the SEM.

BSEs are incident electrons which are elastically scattered by the atoms in the sample. As shown in Figure 2.1 b), the capability of BSEs to escape from the sample depends on the atomic numbers of the irradiated atoms. The number

of BSEs increases monotonically with the atomic number. Therefore BSEs image can show the chemical composition contrast in which the brighter area contains atoms with higher atomic numbers.

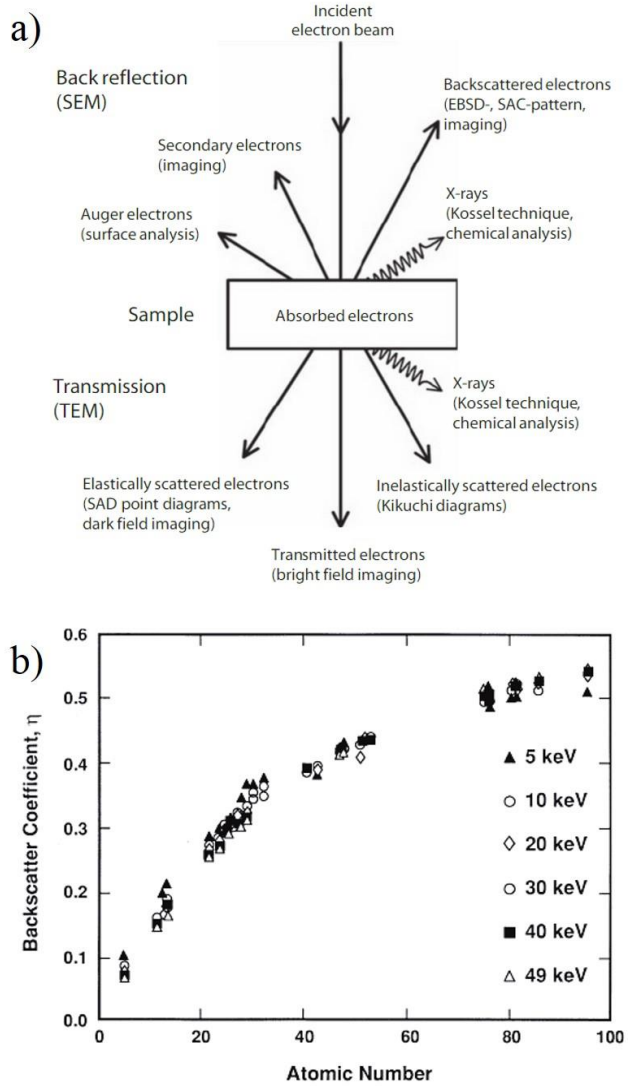

Figure 2.1 a) Schematic illustration of the various signals obtained by interaction from the impact of electron-matter [30], b) the backscattered electron coefficient η as a function of atomic number for different electron beam energies from 5 to 49 kV [31].

2.2 Energy dispersive X-ray spectroscopy

The energy dispersive X-ray spectroscopy (EDS) is a technique of using characteristic X-rays to identify the elements which consists of the sample. Figure 2.2 schematically illustrates the generation of characteristic X-rays when an atom is irradiated by electrons in the SEM which have high enough energy to knock out an electron in the inner-shell of the sample atom. Then the knocked-out electron leaves the atom as a 'free' electron and the atom becomes ionized. Because an absence of the inner shell electron is an excited state, the atom will quickly return to a more stable state after refilling the inner electron vacancy with an outer shell electron. In the meantime, the characteristic X-rays can be generated by the energy difference between an outer-shell electron and an inner-shell electron. By analyzing the energy of this characteristic X-rays, the atomic information of the elements can be identified [32].

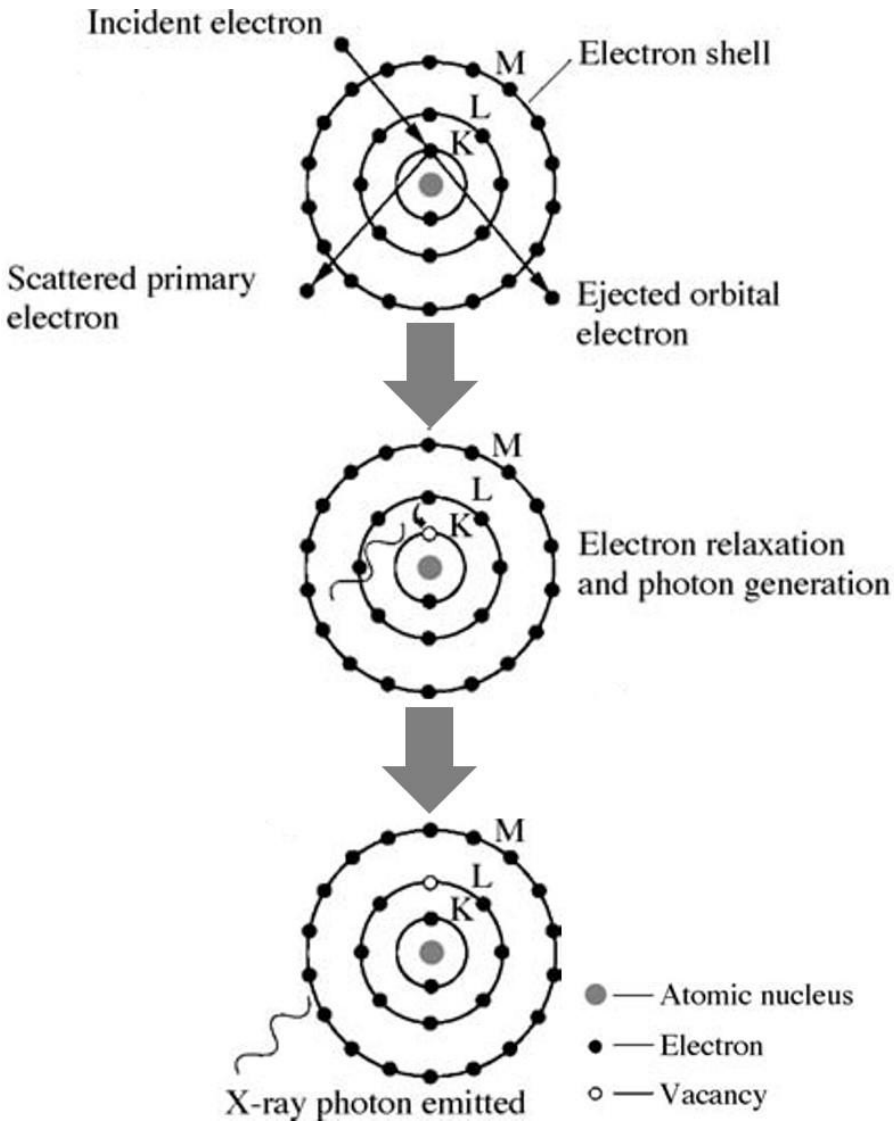

Figure 2.2 Schematic illustration of the process of inner-shell ionization and excitation of a characteristic X-ray photon [32].

2.3 Electron backscattered diffraction

2.3.1 Fundamentals of the electron backscattered diffraction

The electron backscattered diffraction (EBSD) technique relies on the acquisition of electron backscatter patterns (EBSP) and indexing them in a fast manner. EBSPs are obtained in the SEM by focusing a stationary electron beam on the sample, as shown in Figure 2.3. The sample is tilted to the CCD camera along the axis transverse the incident beam and camera. The diffraction pattern is imaged on a phosphor screen. The image is captured using a low-light CCD camera.

Based on the electron diffraction, EBSD [30] offers information of grain orientation, grain boundary misorientation, phases, accumulated strain, etc. in a crystalline material. Figure 2.4 a) illustrates the formation of EBSD patterns (Kikuchi bands). In order to maximize the yield of BSEs, the sample is normally tilted by 70°. Among the randomly scatted BSEs, some are always in Bragg condition and form a diffracted cone. Incoherent scattering of primary electrons can occur at the front and back side between two equivalent crystallographic planes and therefore two cones (Kossel cones) are generated for one set of planes [33]. Given that the Bragg angle is usually very small (~ 0.5° estimated by the electron wavelength and interplanar spacing), the cones are almost flat and displayed as two straight parallel lines when extended to the phosphor

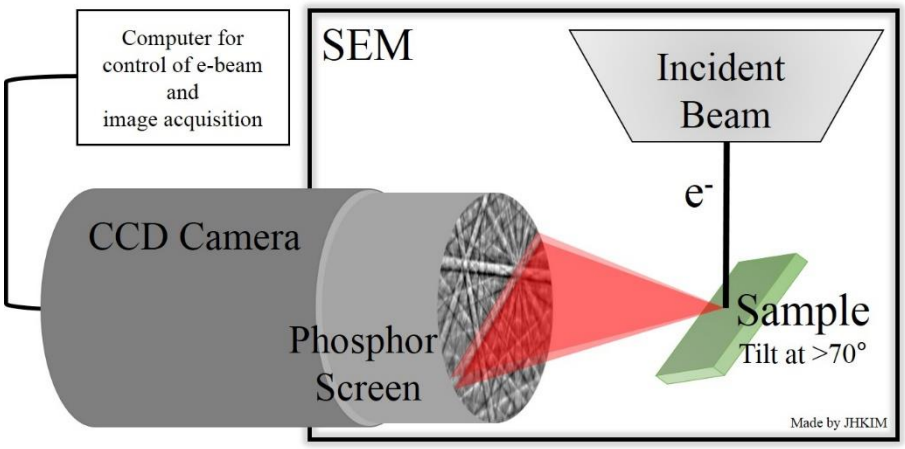

Figure 2.3 Schematic illustration of electron backscatter diffraction (EBSD) set up.

screen. The width between this pair of Kikuchi lines $2\theta_B$ corresponds to the interplanar spacing of this plane family by Equation 2.1.

$$2dsin\theta_B = \lambda \qquad \text{(Equation 2.1)}$$

From the relationship among the Kikuchi bands of lattice planes, we can extract the crystallographic orientation information of the sample. The Kikuchi lines/poles can be indexed to determine the relative orientation of the crystal with respect to a reference sample coordinate system, as shown in Figure 2.4 b).

Nowadays in the automatic computational quantification of EBSD pattern, Hough transform is commonly adopted, where Kikuchi lines are transformed into points in the following method. Each point (x_i,y_i) is transformed into a sinusoidal curve in Hough space (Figure 2.5) by the equation of

$$\rho = x_i \cdot cos\varphi + y_i \cdot sin\varphi \qquad \text{(Equation 2.2)}$$

The Kikuchi line defined by three points in Figure 2.5 a) is then transformed to a point in Hough space which is the interception of three

sinusoidal lines and defined by ρ and φ. Then the detected Hough peaks (Kikuchi bands) are indexed by comparing to the crystallographic database and finding the most probable solution through a voting algorithm. Once the Miller indices of bands in EBSP are determined, the crystal orientation of the corresponding electron beam irradiating position can be calculated. With the crystallographic orientation information, an EBSD scan delivers abundant information on the material, such as average of grain size, grain boundaries characteristic, microtextures, etc. Similar to the XRD pattern, EBSD can also be used to distinguish phases using the characteristic diffraction parameters.

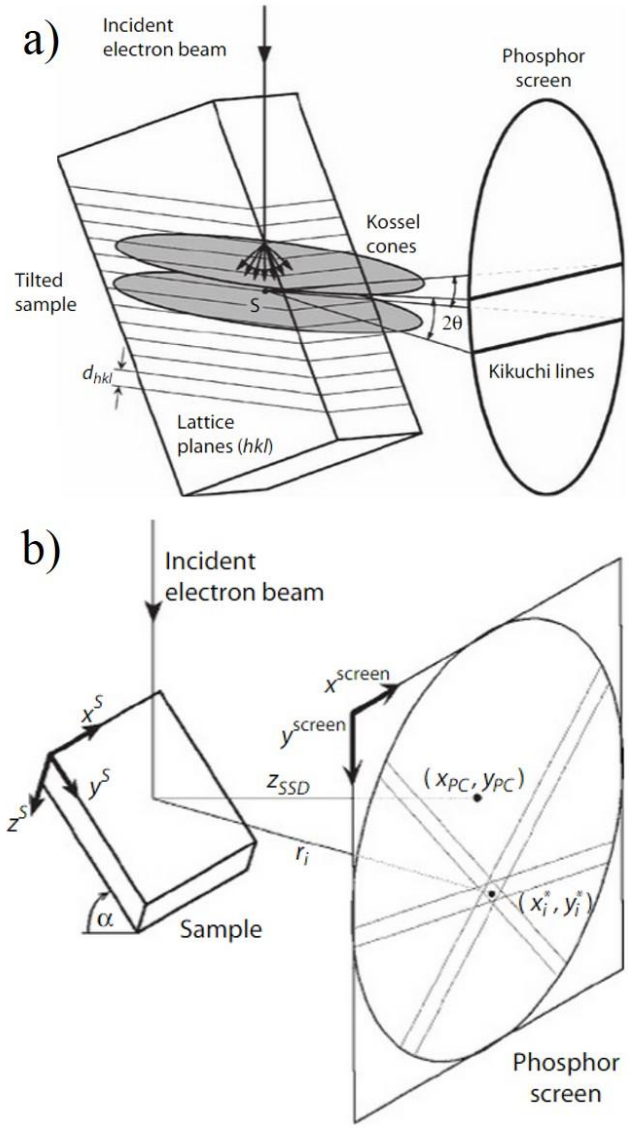

Figure 2.4 a) The formation of Kikuchi lines by EBSD in the SEM, b) Evaluation of indexing of EBSD pattern [30].

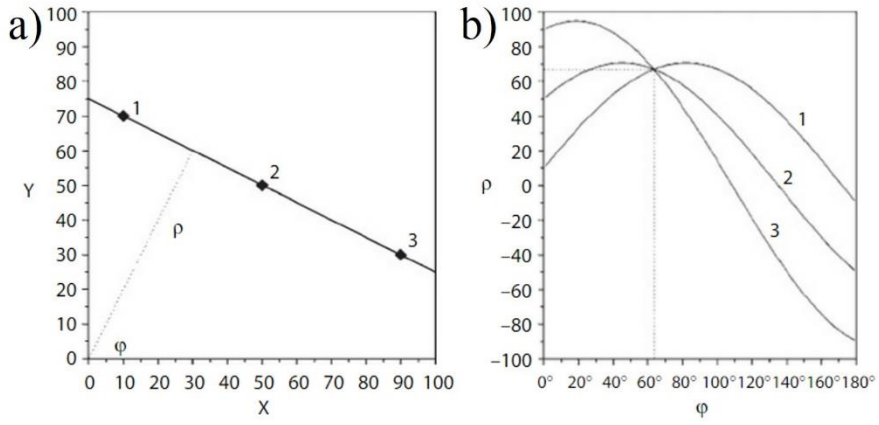

Figure 2.5 Scheme of the Hough transform; a) the Kikuchi line in original pattern, b) the intersection of sinusoidal curve in Hough space b) [30].

2.3.2 EBSD sample preparation (mechanical polishing)

For EBSD observation, first of all, sample surface was prepared by grinding. Grinding was done using rotating discs covered with silicon carbide paper and water. There were a number of grades of paper, with 100, 240, 600, 1000, 1500, and 2000, grains of silicon carbide per square inch. 100-grade therefore represents the coarsest particles and this was the grade to begin the grinding operation. Grinding on one paper was continued until a flat surface was obtained and all the scratches were in one single direction. Then the sample was washed under running water and moved to the next grinding paper grade, by orienting the scratches from the previous grinding paper grade normal to the rotation direction. The previous grinding mark was removed when changing the grinding papers. After the final grinding operation on 2000-grade paper, the sample was cleaned by ultrasonic machine, washed with alcohol and then dried before moving to the polishers.

The polishers consist of rotating discs covered with magnetic polishing disk impregnated with diamond particles (3 and 1 μm) and a lubricant solution. Polishing was started with the 3 μm grade and continued until all the grinding scratches have been removed. Appropriate pressure was added to the sample during polishing on cloth on rotation wheels. It is very important that the sample is thoroughly cleaned using water, followed by alcohol, and dried. Then polishing was continued with 1 μm grade. Finally, the sample was cleaned by

ultrasonic machine, washed with alcohol and dried before EBSD observation.

Also, sample preparation of electro polishing for EBSD observation will be discussed experimental part of next chapters in more detail.

2.4 X-ray diffraction

The X-ray diffraction (XRD) was employed for the phase identification. In the crystal diffraction technique [34, 35], monochromatic x-rays of a specific wavelength is used (in our case Cu k_α radiation: λ= 0.154 nm). Constructive interference x-rays can only occur if there is a set of crystallographic planes that satisfies the Bragg condition (Figure 2.6) as

$$2d' sin\theta_B = n\lambda \qquad \text{(Equation 2.3)}$$

where d' represents the interplanar spacing, θ denotes the incident angle, λ stands for the wavelength of the X-ray and n is the order of reflection. Usually only first order diffraction (n=1) is considered, namely Equation 2.1

The interplanar spacing d depends on crystal structures, lattice parameters and Miller indices {hkl} of the crystallographic planes. For cubic structures, d reads

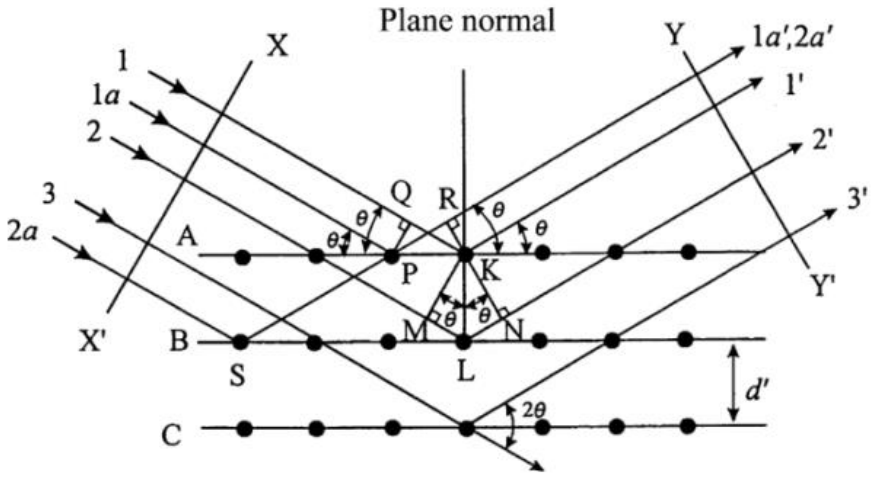

Figure 2.6 X-ray diffraction by a crystal following Bragg's law [34], Parallel lattice planes A and B showing the constructive interference of a front wave of parallel X-ray beam, 1 and 2.

$$d = a/\sqrt{h^2 + k^2 + l^2} \qquad \text{(Equation 2.4)}$$

where a is the lattice parameter. From Equations 2.1 and 2.3, it is indicated that a XRD spectrum (diffracted x-ray intensity vs. 2θ) serves as the fingerprint of the investigated crystal structure. A given wavelength reflection at 2θ corresponds to a specific set of {hkl} planes. However, since reflection in a unit cell does not occur only on a sole set of crystallographic planes but reflections of specific planes can be offset by others with a phase shift, the structure factor should be taken into consideration. There are extinction rules, forbidding the occurrence of certain reflections in body-centered cubic (BCC) and face-centered cubic (FCC) structure. In brief, the conditions for appearance of reflections in common cubic structures are listed below in Table 2.1 [30].

Table 2.1 Conditions to observe reflections in common cubic structures [30].

Crystal structure	Observed reflections	Possible present planes {hkl}
Simple cubic	all h, k, l	{100}, {110}, {111}, {200}, {210}, {211} {220}, {300}, {221}
Body-centered cubic (BCC)	(h+k+l)=even	{110}, {200}, {211}, {220}, {310}, {222} {321}, {400}, {411}
Face-centered cubic (FCC)	h, k, l all odd or even	{111}, {200}, {220}, {311}, {222}, {400} {331}, {420}, {422}

2.5 Focused ion beam

2.5.1 Fundamentals of the focused ion beam

The focused ion beam (FIB) equipment utilized in this study is FEI Helios NanoLab 600/600i, FIB/SEM dual beam instruments. As shown in Figure 2.7 a), in both of these instruments, SEM column is mounted vertically and the FIB is mounted at 52° with respect to SEM column. To make use of the ion beam properly, a vacuum system is necessary. During working, the sample chamber is in a high vacuum environment to avoid contamination of the source by air molecules.

The FIB system is very similar to SEM, except that an accelerated and focused ion beam is used instead of electron beam. The source of ions used is liquid metal ion source (LMIS). The LMIS provides the brightest and most highly focused beam and has a very long life time. There are several metallic elements or alloy sources that can be used in a LMIS sources. Currently the most widely used one is gallium (Ga) for its low melting point (T_m=29.8 ℃), low vapor pressure, relatively unreactive nature and also because Ga is positioned in the center of the periodic table (element number 31), its ions are heavy enough in milling wide range of elements. A Schematic illustration of a Ga LMIS is shown in Figure 2.7 b). During operation, Ga is heated by the coil heater and becomes liquid, then it flows from the reservoir to the W needle tip

which having a radius of less than 10 μm. A large negative potential between the needle and the extraction electrode generates an electric field of magnitude 1010 v/m at the needle tip which causes the liquid Ga to form a point source on the order of 2~5 nm in diameter in the shape of a “Taylor cone”. Once force balance is achieved, the extraction voltage can pull Ga from the W tip and efficiently ionize it by field evaporation at the end of Taylor cone. When the Ga+ ions are extracted from the LMIS, they are accelerated through a potential down to the ion column. Typical FIB accelerating voltage ranges are 2~30 kV. The ion column contains two lenses which are used to define the beam and focus it on the sample. A set of apertures with various diameters are also applied to define the sizes and currents of the ion beam [36-38].

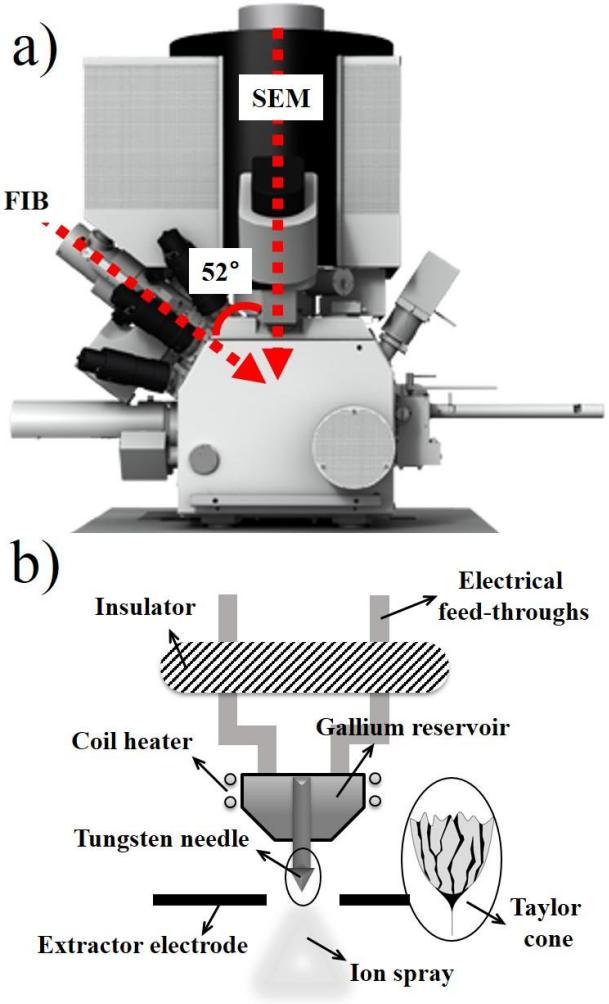

Figure 2.7 a) Helios NanoLab 600i (courtesy of FEI Company) [39], b) Schematic illustration of a liquid metal ion source (LMIS).

2.5.2 FIB milling

Compared with electrons, ions are much larger, heavier and positively charged which make the interactions between ion beam and sample surface are different from that of electron beams. Because of the large size, Ga^+ ions cannot easily penetrate through the individual atoms of the sample, result in a much smaller penetration depth. When an ion hits a sample atom, since its mass is comparable to the mass of the atom, it will transfer a large amount of its momentum to the atom, provide the atom a sufficient kinetic energy to overcome the surface binding energy, and consequently to move away from the surface [38]. This phenomenon is known as sputtering or milling. Figure 2.8 schematically illustrates a sputtering process. Since the primary ion loses its kinetic energy during collision, it may not be able to leave out of the sample surface and eventually stay inside the target material, implanted at some depth (R_p in Figure 2.8). The lower the accelerating voltage the smaller the implantation depth, therefore the low energy beam can be utilized to 'clean' the sample surface at the final stage [36].

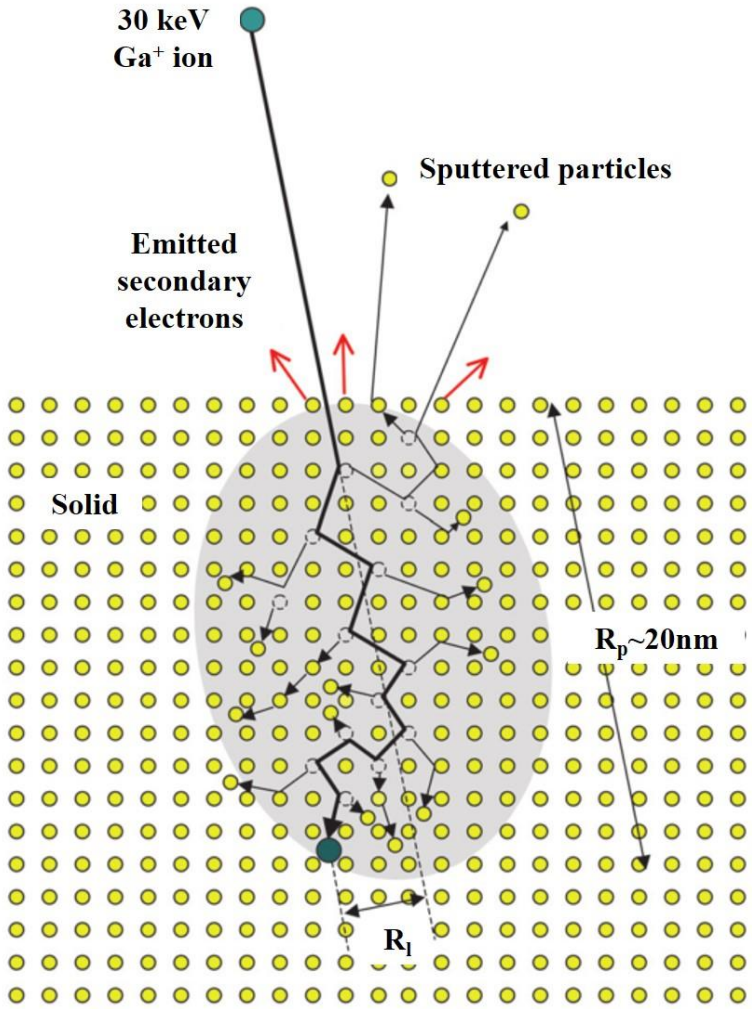

Figure 2.8 Schematic illustration of a collision cascade generated by a 30 kV Ga^+ ion incident on a crystal lattice, showing the damage created in the collision cascade volume, and the projected range R_p and lateral range R_l of the implanted ion [36].

2.5.3 FIB deposition

Gas injection systems (GIS) can be applied in combination with the ion beam to achieve the site specific chemical vapor deposition (CVD) of materials. The schematic illustration of the experimental arrangement is shown in Figure 2.9 a). During deposition the precursor gas is introduced by the GIS nozzle which is positioned properly with respect to the sample surface, usually a few hundreds of microns above the target area. Then the gas molecules are adsorbed on the surface and agglomerate there. When the FIB hits the surface, the molecules are decomposed into volatile and non-volatile components. The non-volatile component remains on the surface as deposition while the residual volatile gas is pumped out. Figure 2.9 b) schematically illustrates the atomic process of this ion beam assisted CVD process. However if the primary ion beam current is too high, the freshly deposited material will be sputtered away. Normally the ion current density is set as 5 $pA/\mu m^2$. In this study, Pt deposition is used for which the precursor gas is $(CH_3)_3(CH_3C_5H_4)Pt$.

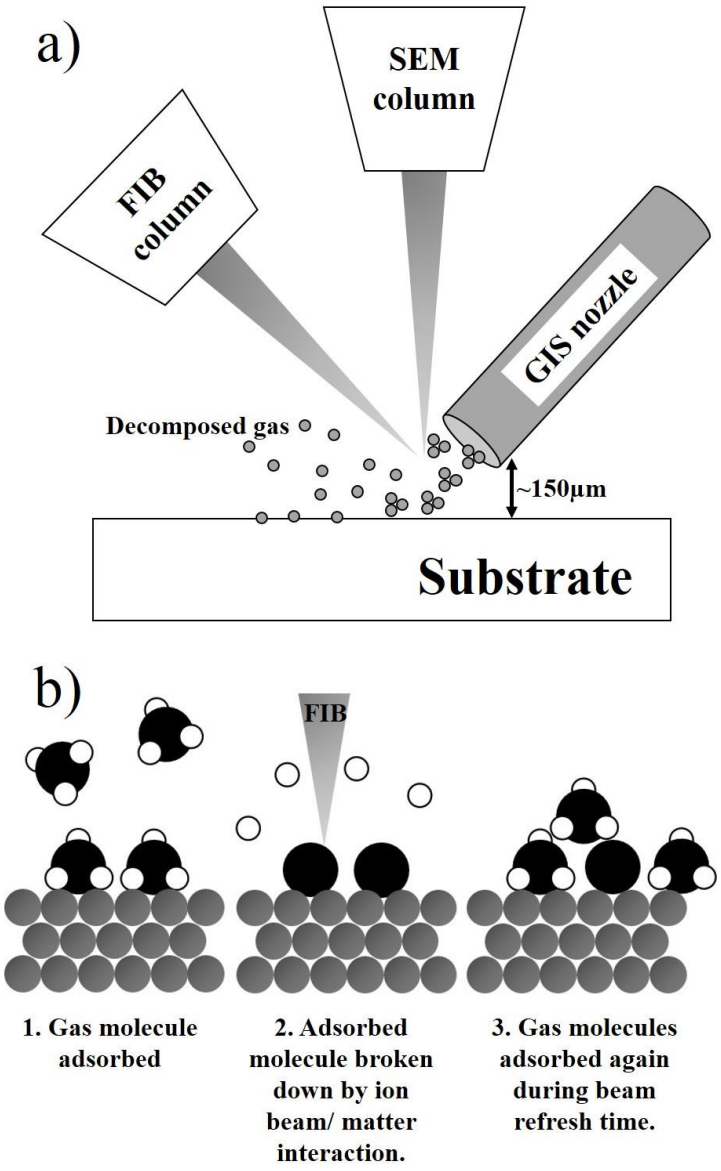

Figure 2.9 a) Schematic illustration of FIB instrument with gas induction system for material deposition, b) Schematic illustration of atomic process during ion-beam assisted gas deposition.

2.6 Transmission electron microscopy

2.6.1 Fundamentals of the transmission electron microscopy

The transmission electron microscopy (TEM) images are formed due to the interaction between very thin sample and transmitted electrons. The electrons emitted from electron source can either be transmitted through the thin sample or be diffracted by atom lattices of the sample. Figure 2.10 shows the schematic of TEM. The electrons are emitted from the cathode and then accelerated by a high voltage towards the anode. After emerging from condenser, the electron beam is focused on the surface of sample. The small thickness of TEM sample and high acceleration voltage allow the electrons to pass through the sample. Because of the interaction between electrons and sample atoms, the electrons can be used as a source which can imply the structure of the sample. On the focal plane, an objective lens forms the diffraction pattern of the sample. The high acceleration voltage also results in a short wave length of the electron beams, thus yields a high magnification ability of the instrument.

The contrast of the TEM images is originated from the atomic and the thickness difference across the sample. The atoms of different elements show different scattering character of the electrons that passes through. Heavy elements scatter more electrons out of the aperture. Thicker sample absorbs

more electrons so that the electrons which run in to the apertures are less. The less electrons penetrate the aperture, the darker contrast is acquired at the corresponding area. The contrast in this case is founded to be in proportion to the square of atomic number, which is called Z contrast. Z contrast can be used to identify the elements.

Another contrast of TEM images is due to diffraction of different crystals. The orientations of neighboring crystals are different, which results in different angles of incidence and thus different intensity of transmitted electrons. This contrast can be used to identify the microstructure of sample.

The third kind of contrast of TEM images comes from phase difference of transmitted electrons when the sample is very thin. In this case, the electrons passing through different positions related to the atom core can rise to an energy difference of about 10~20 eV and thus change the frequencies and wave lengths of passing electrons. According to the phase difference, high resolution images can be produced on which the individual atoms are visible.

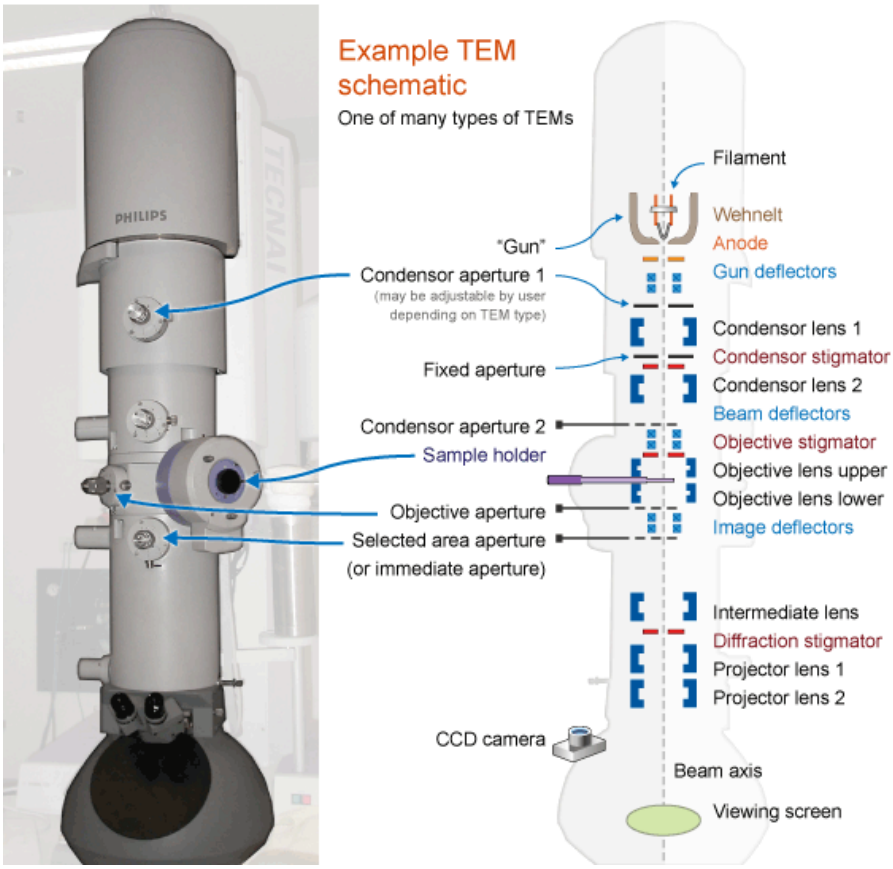

Figure 2.10 Generalised cut-away diagram of the internal structure of a transmission electron microscope alongside an example of a modern instrument [40].

2.6.2 Bright field/Dark field imaging

Typical TEM images are bright field images where the objective apertures are aligned through the diffracted beam. The dark field images are another imaging mode, in which the objective apertures are aligned under the transmitted beam. For imaging the matrix and oxide layer, two ways may be viable. If all apertures are aligned in the center of directed beam, a bright field image will be formed in the image plane of the lens (see Figure 2.11 a)). When the objective aperture is aligned in the position of the diffraction spot, only the diffracted beam that contributes to this spot would show the contrast in TEM. There are two different ways of making dark field images in TEM, either by aperture alignment or by beam tilting. Under the circumstances of aperture alignment, the aperture is aligned to the position where the selected spot is located (Figure 2.11 b)). In the condition of beam tilting, the beam is tilt so that the interesting spot and the objective aperture are exactly located at the optical axis (Figure 2.11 c)).

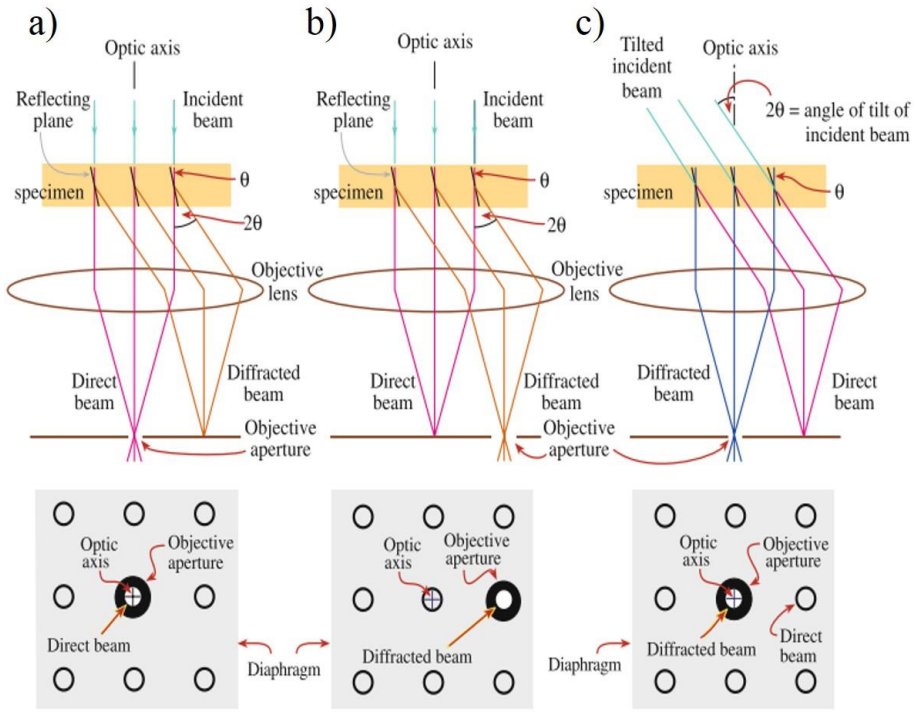

Figure 2.11 Electron beam path and objective aperture position for different imaging mode [41]; a) Bright field imaging, b) Dark field imaging, c) Center dark field imaging.

2.6.3 Selected area diffraction (SAD)

To utilize diffraction of electrons at the crystal lattice for crystal structure determination, the thin sample is irradiated with a parallel electron beam in TEM. By inserting an appropriate aperture, the area of interest can be selected. When the Bragg conditions ($n\lambda = 2dsin\theta$) are satisfied, constructive diffraction occurs and diffraction pattern appears in the back focal plane of the microscope, which is then focused onto the main viewing screen or the photographic plate. Because the wavelength of electron beam is very short, the diffraction angles between the reflecting lattice planes and the primary beam are very small, most approximately 2°. This means that all the reflecting planes are situated almost parallel to the primary beam or in other words, the primary beam is a zone axis of the reflecting planes (Figure 2.12 a)). Using the approximation $sin\theta \approx \theta$ for a small angle, the Bragg's law can be rewritten as

$$n\lambda \approx 2d\theta = \frac{2dR_{hkl}}{2L} \qquad \text{(Equation 2.5)}$$

where L is the camera length of a TEM, i.e. the distance between sample and photographic plate and R_{khl} is the distance between primary beam and diffraction spot hkl as shown in Figure 2.12 b). With n=1, it follows;

$$d = \frac{\lambda L}{R_{hkl}} \qquad \text{(Equation 2.6)}$$

The term λL is called camera constant, which can be known form experiment when the acceleration voltage is fixed. Consequently d can be calculated and then the crystal structure and orientation of the crystal can be decided.

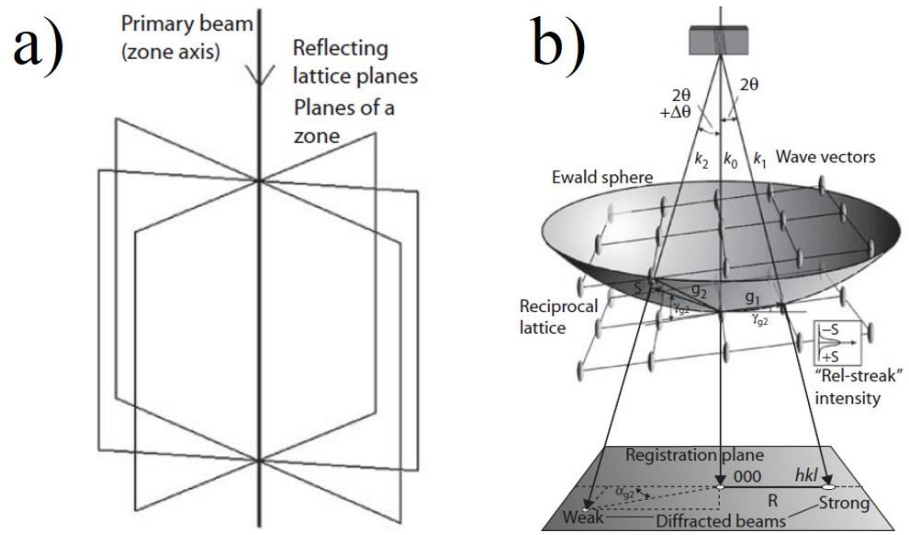

Figure 2.12 Schematic illustration of the formation of SAD patterns; a) Primary beam as a zone axis for several diffracting planes [42], b) Formation of diffraction spots [41].

2.7 Atom Probe Tomography

2.7.1 Fundamentals of the atom probe tomography

The origin of the atom probe technique can be traced back to 1929, when the Fowler and Northeim proposed a method to emit electrons from a solid by quantum mechanical tunneling, following Oppenheimer's calculation of the time to ionize an atom in vacuum [43]. In 1935, Erwin Müller invented a new type of microscope, which was the prototype of the field ion microscope (FIM), A field electron emission image from the sample was for the first time produced, when a suitable negative voltage was applied [43]. The image produced by this instruments contained both crystallographic and electron work function information with a spatial resolution of the order of 2 nm [43].

The principle of FIM is as follows; the sample has a radius of curvature of less than 50 nm and is maintained at a positive potential. It is cooled to 20~100 K and subjected to a high positive voltage V to generate a high electron field (15~60 V/nm) [44]. Imaging gases are field ionized in high electric field and then accelerated along the electric field lines toward a detector [43]. With these signals, the field ion image can be formed. In 1955, Müller and Bahadur observed single atoms for the first time with FIM when they employed He as image gas and cooled a W tip to 78 K [45]. If the specimen voltage is further increased, the surface atoms themselves can be field ionized and evaporated

from the sample [43].

The atom probe is a combination of a FIM and a mass spectrometer. The first generation of atom probe was introduced by Müller, Panitz and Mclane in 1967 and is named atom probe field ion microscope (APFIM) [46]. The principle is that a probe hole in front of the fluorescent screen provides an entrance to the detector to determine the field of analysis. After the ionization of surface atoms, they are accelerated through the ultra-high vacuum towards a time of flight detector. With the information of measured time of flight, the mass to charge ratio can be calculated, thus providing the chemical identification of detected elements.

In this study, the atom probe tomography (APT) analyses were conducted using a high mass resolution local electrode atom probe equipped with a large angle reflectron coupler (LEAP 3000X HR and LEAP 4000X HR, Cameca Instr.). The experimental setup is schematically shown in Figure 2.13. The sample is mounted on a cryogenically cooled stage, the position of which can be adjusted in three dimensions. The local electrode with a 40±10 μm aperture at the apex is placed in close proximity to the sample, within about 30 μm.

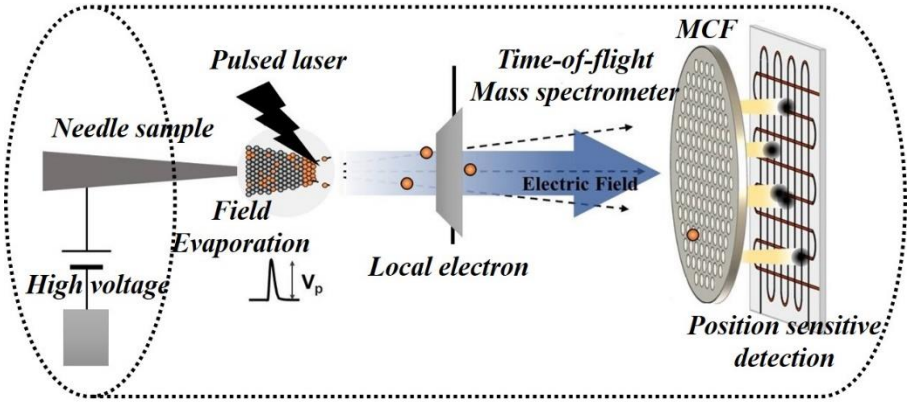

Figure 2.13 Schematic illustration of the experimental setup for a local electrode atom probe tomography system.

Principally, APT is an analysis technique combining FIM and time-of-flight mass spectrometry (TOF MS). The basic principle is that field evaporation of the surface atoms of the sample and then identifies them by the technique of time of flight mass spectrometry. During measurement, a moderate voltage (< 15 kV) is supplied to the nanometer-sized sharp needle sample. Since the radius of the curvature of the tip (R) is normally less than 100 nm, an enormous electric field strength of 1010 v/m or greater can be obtained. The formula that gives an estimation of the electric field (F) at the surface is [47];

$$F = V/k_f R \qquad \text{(Equation 2.7)}$$

Where V is the supplied voltage, k_f is a shape factor or field reduction factor. For a sphere shape, k_f=1, but for the needle shape, the electric field is reduced in magnitude, k_f is greater than 1.

Under such high field, electrons can be stripped from atoms on the surface and then the resultant positivity charged ions are accelerated towards the local electrode. A diagram for a model of the field ionization process is shown in Figure 2.14 a). The barrier for an atom to ionize and evaporate is strongly reduced by the presence of an electric field, allowing the atom to ionize. As schematically illustrated in Figure 2.14 b), there are two ways to control the

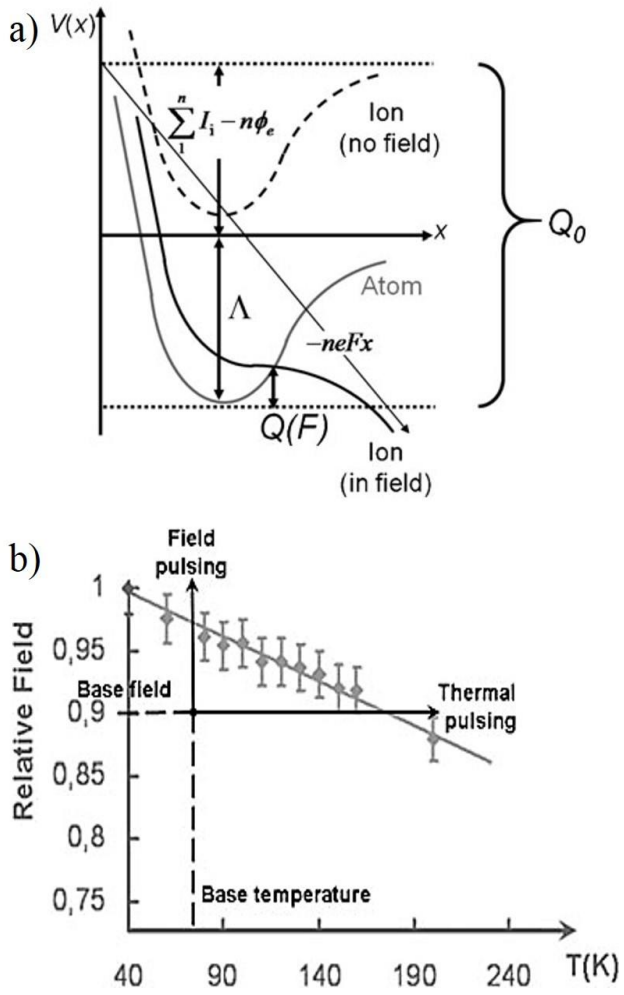

Figure 2.14 a) Atomic and ionic potential energy diagram with and without electric field. V is the potential, Λ is the sublimation energy, n is the degree of ionisation, I_i is the I_{th} energy and ϕ_e is the work function of the surface emitting the ion, Q_0 and $Q(F)$ are the energy barrier without and with electric field respectively, b) The relationship between electric field and temperature to achieving the same evaporation rate [47].

field evaporation; HV-pulsing and laser-pulsing, i.e. the sample is kept at a base voltage meanwhile a local electrode is given a pulsed voltage or the tip of the sample is given a laser pulse. The base voltage is kept close to the voltage needed for field evaporation and the voltage or laser pulse is applied to increase the field just enough to induce field evaporate a single atom [47].

The ions will continually fly through the hole of the local electrode and finally hit the position sensitive detector which equipped with a TOF MS with single atom sensitivity, where the X-Y position of the atom is represented by the hit position and the Z position is determined from the sequence of evaporation events. This process is repeated until either a suitable amount of ions are detected or the sample fractures. The identity of an atom uses the technique of TOF MS. After ionization of surface atoms, atoms are accelerated through the ultra-high vacuum towards a time-of-flight detector. With the time measured (time delay between pulse application and ion detection), the mass to charge ratio can be calculated via

$$\frac{1}{2}mv^2 = neV \qquad \text{(Equation 2.8)}$$

and

$$v = L/t_{flight} \qquad \text{(Equation 2.9)}$$

where m is the mass of the ion, ne is its charge, V is the applied voltage, v is the velocity, L is the distance between sample and detector and t_{flight} is the time of flight measured by the delay between pulse application and ion detection. Correlating Equation 2.8 with Equation 2.9, the description of mass to charge ratio m/n can be obtained

$$\frac{m}{n} = M \approx 2eV\left(\frac{t_{flight}}{L}\right)^2 \qquad \text{(Equation 2.10)}$$

It gives the mass-to-charge state ratio of the M ion, which allows the identification of its elemental nature, taking into account the natural isotope abundance of elements.

Finally, the collected ions are reconstructed in 3D, in order to visualize the field evaporated part of the original sample. It is a process of reconstructing a virtual sample atom-by-atom by reversely projecting the detected coordinates back onto the sample surface. Two coordinates - lateral coordinates and depth coordinate - are necessary for the determination of ion position. The lateral coordinates are obtained via reverse point projection approximation, assuming

that the flight route of ion is a straight line from its original position to the point that it hits detector. Due to the layer-by-layer evaporation, the evaporation sequence yields the position of ions in depth direction.

2.7.2 APT sample preparation

The ‘Lift-out’ method was employed to fabricate the APT samples. As demonstrated in Figure 2.15, there are two main essential steps; sample cut and lift-out of the wedge, annular milling (sharpening) the wedge block to the APT needle. At first the sample surface is imaged under electron beam to find the regions of interest (ROI), i.e. oxide layer nearby grain boundary. Then the materials on both sides of ROI are milled away at the angle of 30° with respect to the normal of the sample surface, leaving the ROI having a shape of a uniform triangular prism with the edge length of 2 μm. This triangle-shaped bar of the material is often referred to as a wedge. Afterwards a free cut is made at one end of the wedge. Micromanipulator is then inserted and positioned very close to this free side and Pt deposition is used to bind the wedge tightly to the micromanipulator. Subsequently the second free cut is made at the other end of the wedge to completely release it from the underlying material. By carefully move the micromanipulator and sample stage, the wedge is transferred to the Si coupon and bounden on one of the Si posts in a microtip array by Pt deposition. It is then cut off by Ga^+ ion beam to be released from the wedge.

On the next step a series of annular milling is performed with progressively smaller inner diameter of the doughnut pattern and ion current. Commonly a last low-energy (2 kV) ion beam milling step is necessary to clean the damaged surface of the tip. To be successfully measured in the APT, the

final radius of the tip should smaller than 100 nm and the feature of interest should not be far away from the apex.

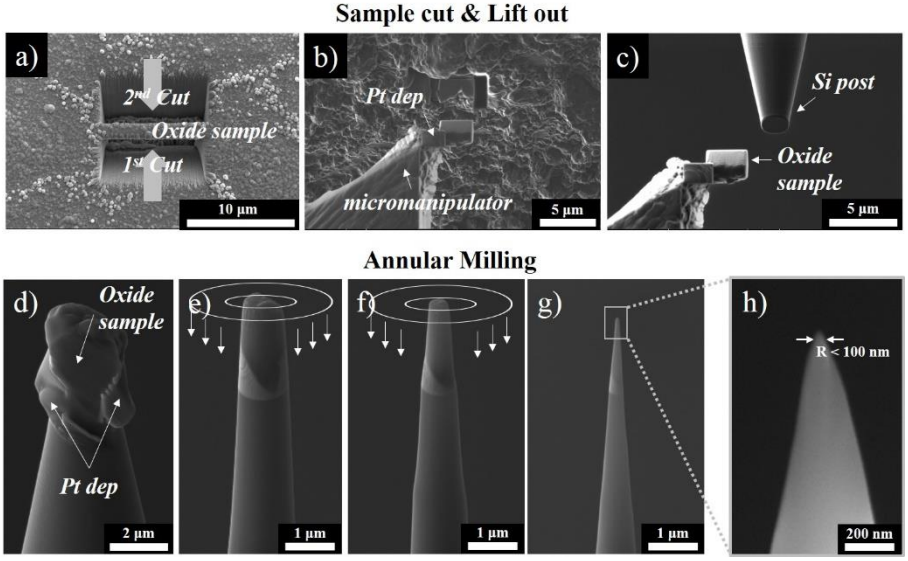

Figure 2.15 Steps of 'sample cut and lift out' of the wedge and 'annular milling' it into the APT sample. a) An SEM image of ROI and oxidation sample around ROI are removed by the trench milling, b) The wedge is transferred by attached to a micromanipulator, c) The wedge is bounden on the top of the Si microtip, d) A block of wedge is cut off by the Ga^+ ion beam, e), f), g) and h) Procedures of annular milling of the APT needle, the inner diameter of the doughnut ring pattern becomes smaller and smaller (the downward arrows indicating the Ga^+ ion beam direction).

Chapter 3

Effect of Grain Size on the Oxidation Resistance

: High temperature oxidation behavior of Cu added austenitic stainless steels (Super304H) for the advanced thermal power plant applications

3.1 Introduction

Ultra Super Critical (USC) coal fired thermal power plants are operated at a steam pressure of ≥ 246 kgf/cm^2 and a steam temperature of ≥ 593 °C [48, 49] in the boiler tube main line, such as in the superheater and reheater. These operating conditions require new boiler tube materials that can resist these extreme temperature and pressure conditions. In the context described there are two main requirements for boiler tube materials, namely, creep strength and oxidation resistance. Austenitic stainless steels are considered as candidate alloys for the boiler tubes owing to their higher strength at operating conditions compared to the previously used ferritic stainless steels [49, 50]. Cu added austenitic stainless steels were developed in the 1990s on the basis of conventional 304 stainless steels, where Cu was added to form stable copper precipitates in the matrix [48, 51, 52]. Similar lattice parameters and a small interfacial energy between the copper precipitates and the austenitic matrix

retard precipitate growth at high temperature [53], enabling the material to maintain its high creep strength [54, 55].

Steam side oxidation of the boiler tube is one of the main mechanism of power plant failure besides creep rupture, where the failure occurs due to poor adhesion of the oxide. In particular, Fe-rich oxides are considered to be poorly adhesive and non-protective, rendering the alloy susceptible to cracks and spallation during operation. The lifetime of boiler tube materials hence strongly depends on their oxidation resistance.

Oxidation of austenitic stainless steel has already been studied by several authors as a function of alloy composition [56], surface treatment and preparation [57-65], temperature [56, 57, 63, 64, 66-68], flow rate [69-71] and oxygen partial pressure [57, 69, 72]. These works document that such steels can form a stable, dense, continuous, adherent and protective oxide layer, containing oxides such as Cr_2O_3, SiO_2 or Al_2O_3 above 700 °C [73-75]. The initial stages of oxidation of Cr containing alloys such as the AISI 304 stainless steels involve formation of a protective oxide layer, normally Cr_2O_3, followed by formation of a spinel type oxide [57, 76-78]. Protective Cr_2O_3 oxide layers on stainless steel considerably reduce the oxidation rate in very aggressive environments [79, 80] and their formation requires a Cr concentration of > 18 wt.% in order to prevent oxidation of stainless steels [6, 25, 81] during the initial oxidation stage, characterized by the growth of Cr-rich oxides, the Cr that is

required for the formation of a protective layer is provided by the fast outward flux of Cr along the grain boundaries. As a result, the grain size [57, 63, 74, 80, 82-85] should play an important role for the supply of Cr to the matrix/oxide interface, since the diffusivity of Cr along grain boundaries is much higher than that inside the bulk grain.

For characterization of thin oxide layers X-ray photoemission spectroscopy (XPS) [71, 85], auger electron spectroscopy (AES) [66, 69-72], secondary ion mass spectroscopy (SIMS) [64, 71], transmission electron microscopy (TEM) [58, 86, 87] and atom probe tomography (APT) [87-89] have been applied. Each of these methods faces its specific problems when it comes to acquiring quantitative data, but they can provide very useful information about thin surface oxide layers when being jointly used. In this work, we studied the oxidation characteristics of a Cu added austenitic stainless steel. Complementary APT, TEM, EBSD, EPMA and XRD analyses were performed to elucidate compositional and structural changes upon oxidation at 700 °C in air with 20% water vapor with a particular focus on the role of grain boundaries during the initial/early stages (30 min~12 h) and long term (~500 h) of oxidation.

3.2 Experimental

3.2.1 Alloy processing

An austenitic stainless steel containing about 18% Cr, 9% Ni, 0.1% C, and 3% Cu (in wt.%) was produced by vacuum induction melting. The nominal composition of the alloy is given in Table 3.1. Chemical analysis was carried out by inductively coupled plasma mass spectrometry (ICPMS).

The ingot was solution treated for 24 h at 1200 ℃, forged at 1200 ℃ and cooled in air. Subsequently, the sample was hot rolled at 1150 ℃ to 75% reduction in thickness. Further thermo-mechanical processing steps were applied in order to obtain various average grain sizes [84].

The processing basically involved cold rolling and annealing cycles. The first sample was only solution treated, which the sample was annealed at 1150 ℃ for 30 min and then water quenched which is referred to as "large-grained (LG)" sample (grain size 27 μm) in the following. The second sample was multi step and annealed, which the sample was deformed to 5% reduction per pass and annealed at 1000 ℃ for 30 min between subsequent passes, where the total reduction was 80% which is referred to as "medium-grained (MG)" sample (grain size 17 μm). The last sample was one step and annealed, which the sample was deformed by cold rolling to 80% reduction per pass and annealed at 1000 ℃ for 1 min which is referred to as "small-grained (SG)"

sample (grain size 8 μm). For oxidation studies, rectangular samples of 10 mm in length, 7 mm in width and 2 mm in thickness were cut from the center of the bulk material.

Table 3.1 Bulk chemical composition of the Cu added austenitic stainless steel (in wt.% and at.%).

	Fe	***Cr***	***Ni***	***Mn***	***Cu***	***Nb***	***Si***	***C***	***N***
wt.%	Bal.	18.2	9.28	0.78	2.96	0.41	0.20	0.11	0.11
at.%	Bal.	19.3	8.71	0.78	2.57	0.24	0.39	0.51	0.43

3.2.2 High temperature oxidation experiments

Before oxidation testing, the surfaces and edges of samples were mechanically and electrolytically polished for electron back scattered diffraction (EBSD) analysis. The electrolyte was used consisted of methanol 590mL, methyl propanol 350mL and perchloric acid 60mL under conditions of -30 ℃ and 18 V for 30 s using Electropolisher (LectroPol-5, Struers, USA). The oxidation tests were performed at 700 ℃ in air with 20% water vapor for 30 min to 500 h. These temperature values are high as compared to the usual USC power plant operating conditions and have been selected to simulate a severe environment and to accelerate the degradation of material. Figure 3.1 shows the set-up chosen for oxidation test under water vapor conditions, which consists of three main parts. An air-H_2O mixture was produced by passing synthesized air (99.9%) at a stable flow rate of 0.6 L/min (air supplement) through deionized water maintained at 75 ℃ (water vapor controller) and a tubular furnace fitted with a 70 mm diameter quartz tube. The horizontal furnace temperature was kept constant to ±2 ℃ as measured by a calibrated type K thermocouple. The furnace was set to the required temperature before inserting the samples. The samples were placed in a high purity alumina (Al_2O_3) crucible. After 1, 2, 6, 12, 28, 56, 80, 100, 200, 300, 400 and 500 h of oxidation, the samples were removed from the furnace and weighed using a high sensitive microbalance with a resolution of $\pm 10^{-5}$ g after room temperature cooling.

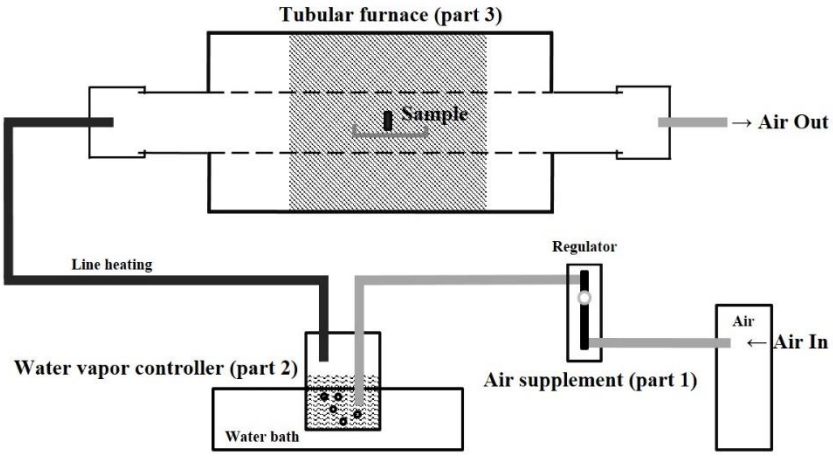

Figure 3.1 Experimental set-up for oxidation testing in flowing atmosphere containing H_2O vapor.

3.2.3 Initial (~30 min) oxidation stage analysis

3.2.3.1 Atom probe tomography and Transmission electron microscopy

Atom probe tomography (APT) analyses of the oxides formed during the initial stages was conducted using a local electrode atom probe (LEAP 3000X HR, Imago Scientific Instrument, USA). The cross-sectional morphology and diffraction patterns of the oxide layers were observed using transmission electron microscopy (TEM, FEI Tecnai F20, USA).

APT and TEM samples were prepared from the identical grain and grain boundaries, where the regions analyzed with APT and TEM were separated by ~4 µm. Site-specific sample preparation is illustrated in Figure 3.2. A Ni layer was sputter-deposited to protect the brittle oxide layer on the substrate. Both, APT and TEM samples were prepared using a dual-beam focused ion beam (FIB) device (FEI Helios Nanolab 600i, USA), using the lift-out method. The TEM lamella was attached to a Cu grid and thinned by FIB milling to a thickness of ~50 nm. Needle-shaped APT samples were prepared by a lift-out procedure similar to TEM sample preparation, mounting to an array of Si microtips and annular FIB milling [90-92]. To reduce the Ga^+ ion beam damage, both the APT and TEM samples were FIB milled using 5 kV ion energy in the final preparation steps. The applied acceleration voltage for TEM analysis was

200 kV. Based on the results obtained in previous studies [87, 89], APT analysis was performed in laser mode, applying laser pulses of 532 nm wavelength with 200 kHz pulse frequency and 0.6 nJ pulse energy at ~60 K sample temperature. APT data reconstruction and analysis were carried out using the IVAS 3.6.6 software of Cameca Instruments.

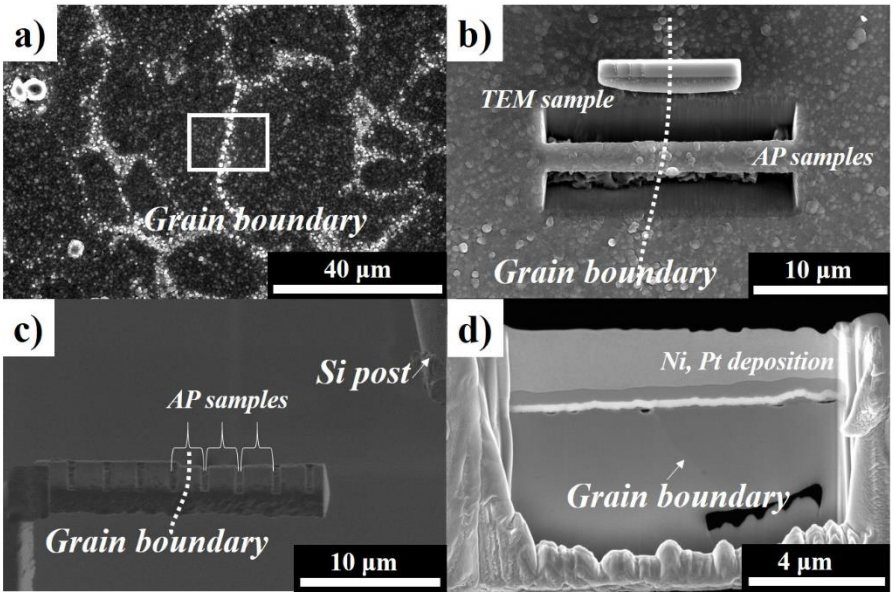

Figure 3.2 Site-specific APT/TEM sample preparation method to jointly map the structure and composition of the selected regions, e.g., at grain boundaries in the MG sample after 30 min of oxidation at 700 ℃ in air with 20% water vapor; a) Ni-coated surface to protect the oxide layer and selected region of interest (white box) containing a random grain boundary, b) Pt electron-beam and ion-beam deposition for TEM sample preparation and 1st/2nd mill cut for APT sample preparation, c) The APT samples with positions away from the actual grain boundary were lifted out using a micromanipulator, d) The thin TEM lamella sample containing the grain boundary.

3.2.4 Early (~12 h) and long term (~500 h) oxidation stage analysis

3.2.4.1 Scanning electron microscopy, electron backscattered diffraction and electron probe microanalysis

Oxide layers were also analyzed by scanning electronic microscopy (SEM, Hitachi SE-4300E, Japan) in combination with electron backscattered diffraction (EBSD) system (*e*-FlashHR, Bruker, Germany). The EBSD experiments were carried out at a 20 kV accelerating voltage and a 4 nA probe current. In order to quantitatively analyze the average grain size and number fraction of CSL grain boundaries, ideally more than 100 grains per map were analyzed using EBSD with a step size of 0.1 to 0.5 μm (CSL: Coincidence Site Lattice). The grain size distribution and number fraction of CSL grain boundaries were analyzed using the Esprit 1.9.4 software of Bruker. Grains were reconstructed using a misorientation angle of 5°. Grains were reconstructed both, by considering and by neglecting the Σ3 grain boundaries. Additionally, the surface oxide composition and elemental distributions were determined using electron probe microanalysis (EPMA, JEOL JXA-8500F, Japan).

3.2.4.2 X-ray diffraction

Phase analyses of the oxide layers was carried out by X-ray diffraction (XRD, Bruker D8 advance diffractometer, Germany, Cu kα radiation: λ=0.154 nm). The XRD data was obtained by point scanning in the 2θ angular range from 15° to 80° with a step size of 0.02° (2θ) and a scan time of 2s per step at room temperature. Diffraction patterns were indexed by using the X'Pert HighScore Plus of PANalytical with the JCPDS database.

3.3 Results

3.3.1 Initial oxidation (~30 min) stage

3.3.1.1 Initial stage of oxidation behavior of Cu added austenitic stainless steel

In ferritic stainless steels, selective oxidation occurs, depending on grain orientation and grain boundary characteristics [93, 94], whereas in austenitic stainless steels selective oxidation depending on grain size was reported [84].

Back scattered electron (BSE) images (composition contrast) and EBSD band contrast maps obtained from identical regions of the MG sample are shown in Figure 3.3 before and after 30min oxidation at 700 ℃ in air with 20% water vapor. As shown in Figure 3.3 a), selective oxidation is observed at a certain distance from the grain boundaries. The light gray regions mark a grain boundary, while the dark gray regions correspond to the grain interior. The identified grain boundaries are random high-angle grain boundaries (see Figure 3.3 b)). Σ3 CSL grain boundaries that exist inside grains are mostly coherent and do not show selective oxidation. The particles imaged with bright contrast in Figure 3.3 a) can be attributed to Nb-containing carbide precipitates [52]. Figure 3.3 c) shows an EPMA map acquired from the same sample. It shows the presence of O, Fe, Cr, Ni, Mn and Cu. According to the EPMA data, two

types of oxides are formed on the outer surface. A Cr-rich oxide is detected at the grain boundaries, where Fe, Mn, and Ni are also found to be enriched. The dark gray regions in Figure 3.3 a) are depleted of Cr when compared to the grain boundary region, whereas the intra grain region shows a higher concentration of O. The Cr and Fe content are ~40 wt.% Cr and ~52 wt.% Fe, respectively, in the surface oxide layer.

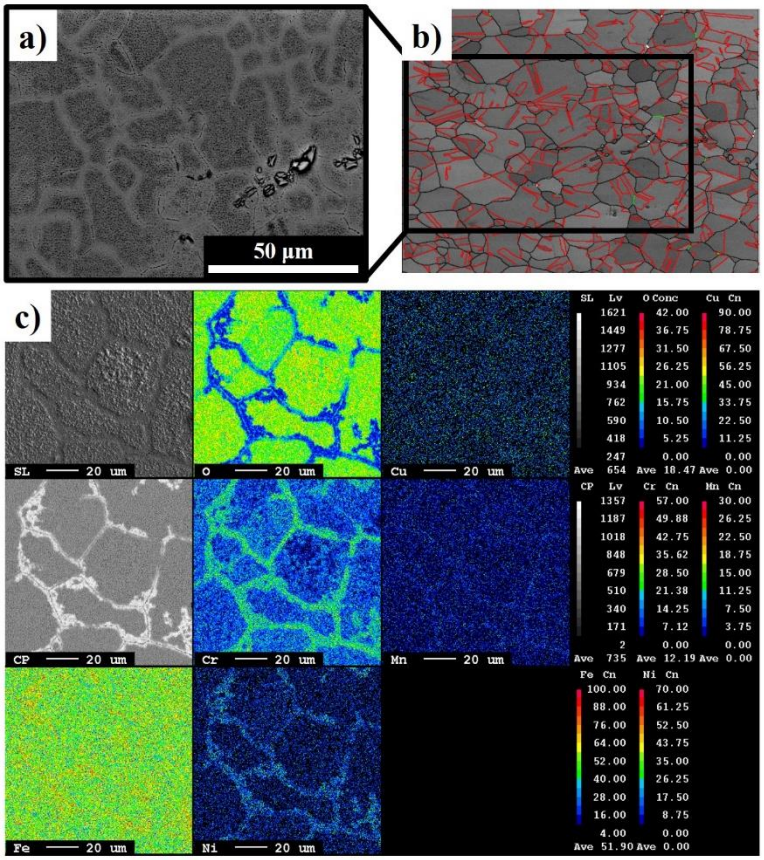

Figure 3.3 a) Back scattered electron (BSE) image in the SEM obtained on the surface of the oxide layer formed in the medium grain sample after 30 min of oxidation at 700 ℃ in air with 20% water vapor. b) EBSD band contrast map overlaid with grain boundaries, including special boundaries (red: Σ3, green: Σ5, white: Σ7, and black: random boundaries) obtained on the surface before oxidation on the medium grain sample. c) EPMA mapping obtained on the surface before oxidation obtained on the medium grain sample after 30 min of oxidation at 700 ℃ in air with 20% water vapor.

3.3.1.2 Oxide composition analysis using atom probe tomography

Figure 3.4 a) shows cross-sectional SEM micrographs of the oxide layer in the MG sample after 30 min oxidation. The thicker oxide forms in intra grain regions whereas the thinner oxide tends to be formed near grain boundaries. The oxide thickness is about 50~100 nm near grain boundaries and ~200 nm in the intra grain region. The outward diffusion of Cr can generate Kirkendall voids at the matrix/oxide interface, which agrees with the surface morphologies reported previously [95-98]. Three locations for the APT analysis presented in Figure 3.4 a) are schematically marked as Figure 3.4 b), c) and d). The grain boundary correspond to the boundary given in Figure 3.2 d). Same area was studied using both APT and TEM. 3D elemental maps acquired by 3DAPT results and schematics drawing to highlight matrix and oxide region are presented in Figure 3.4 b), c) and d). The distribution and enrichment regions of the different elements clearly reveal the outer oxide, the inner oxide and the matrix regions, respectively. Tips 1 and 2 have the outer oxide at the top and the matrix at the bottom. Tip 3 has the outer oxide at the top while the inner oxide and the matrix are located at the bottom. It is well known that a similar dual-layer structure is formed in the intra grain region of large-grained Fe-Cr-Ni austenitic stainless steels during long-term oxidation and the original surface before oxidation is located at the outer/inner oxide interface [99].

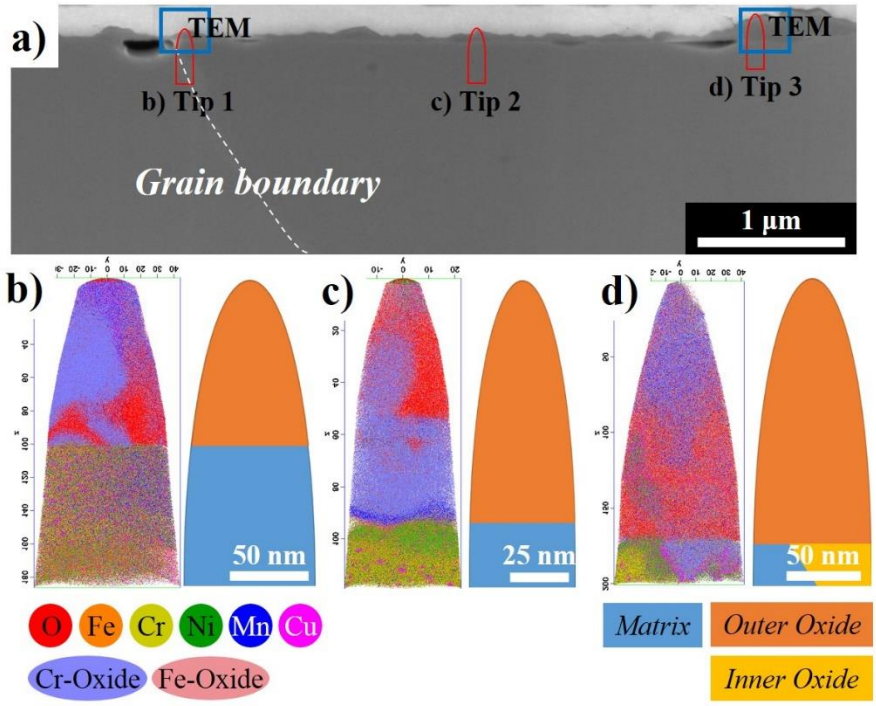

Figure 3.4 a) Cross-sectional view of the oxide and matrix formed in the medium grain sample after 30 min of oxidation at 700 ℃ in air with 20% water vapor, b) 3D atom elemental map displaying the overall distribution and schematic drawing of the regions found in tip 1 (~0.3 µm away from the grain boundary containing over 27 million ions within a volume of 44x44x186 nm^3), c) Tip 2 (~2 µm away from the grain boundary containing over 14 million ions within a volume of 22x22x118 nm^3), d) Tip 3 (~4 µm away from the grain boundary containing over 23 million ions within a volume of 40x40x200 nm^3).

Therefore, we suggest that the outer and inner oxide layers grow by outward diffusion of metal atoms and inward diffusion of oxygen atoms, respectively.

APT maps of all three tips are shown in Figure 3.4 e). First of all, the O/O_2 map shows the distribution of oxygen and confirms the presence of outer and inner oxide layers. Moreover the Cr/Cr oxide and Fe/Fe oxide maps clearly show Cr and Fe enrichments in the outer oxides. Also, the Cr oxide map of Tip 3 shows that a Cr-rich oxide layer formed in the inner oxide [75]. Ni is present on the top region in Tip 1 and 2 as part of the protective Ni-coating. Mn is present on the top region, as it has diffused through the oxide to the surface to form an external spinel layer [74]. Spherical Cu-rich precipitates of uniform size and homogeneous distribution are detected in the matrix and it is correspond to the observation of previous studies [51, 52, 100]. Near the surface the number of Cu-rich precipitates decreases due to diffusion of Cu to the oxide/gas interface during oxidation. With further oxidation, the Cu-containing spinel structured oxide, Fe_2CuO_4 is formed at the top surface of the outer oxide [101].

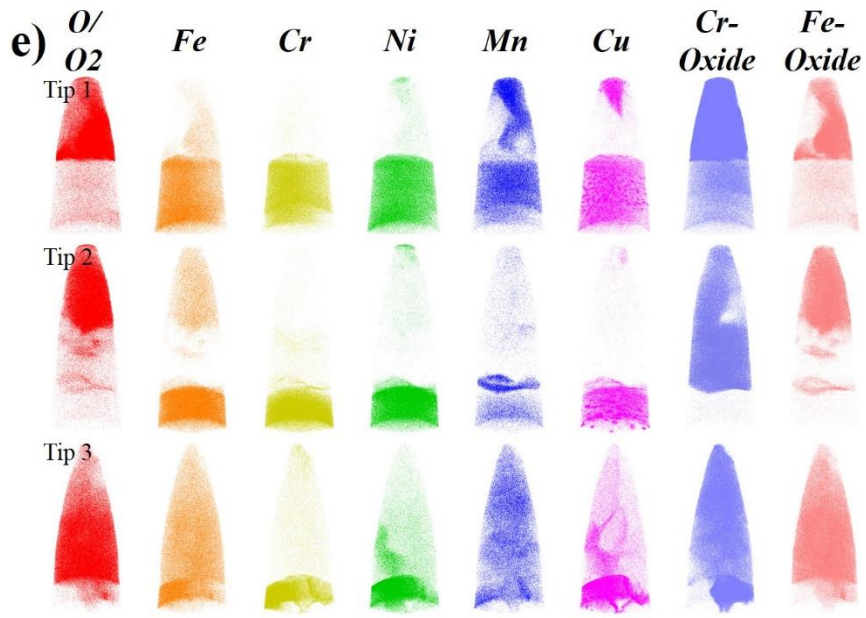

Figure 3.4 e) 3D reconstruction of individual O, Fe, Cr, Ni, Mn, Cu, Cr-oxide (CrO, CrO_2, CrO_3) and Fe-oxide (FeO, FeO_2) ions from all of the tips. (The red (●) dots, orange (●) dots, dark yellow (●) dots, green (●) dots, blue (●) dots, magenta (●) dots, light violet (●) dots and light magenta (●) dots represent oxygen (7.3~100% shown), iron (1.7~10% shown), chromium (30~50% shown), nickel (12~40% shown), manganese (100% shown), copper (52~100% shown), chromium-oxide (10~50% shown), iron-oxide (50~100% shown), respectively.)

Regions of interest (ROI) were clipped from the original APT maps by defining iso-concentration surfaces in order to perform refined phase analyses. Figure 3.5 a), b) and c) show such phase analyses for all three tips. Iso-concentration surfaces of 30 at.% O were chosen to separate the oxide from the matrix region. Subsequently, these oxide and matrix regions were further divided into parts of different compositions to identify individual phases comprising the oxide and matrix, respectively. The mass spectra of the clipped ROI were analyzed in order to determine overall compositions of the phases, where the values are listed in Table 3.2. Although the analyses were conducted on the same grain boundary, oxides near grain boundary and inter grain regions show different compositions. Figure 3.5 a) shows the outer oxide and matrix region of Tip 1. The outer oxide consists of three different phases. Only the outer oxide #1 consists of Cr-rich (Fe,Mn,Cu) and Fe-rich (Fe,Cr) outer oxide. The composition of the Cr-rich (Fe,Mn,Cu) oxide in the outer oxide #1-1, which was found near the grain boundary, amounts to 51.5 at.% O, 17.2 at.% Fe, 22.9 at.% Cr, 3.1 at.% Mn and 2.7 at.% Cu. The diffusion of Mn and Cu atoms along the grain boundary is faster than the bulk diffusion in the intra grain regions. The composition of the Fe-rich (Fe,Cr) oxide in the outer oxide #1-2 is 48.7 at.% O, 38.9 at.% Fe, and 8.23 at.% Cr. The composition of the Cr-rich oxide in the outer oxide #2 is 58.2 at.% O and 38.9 at.% Cr. While the nominal matrix composition of the Cu added austenitic steel is 18%Cr-9%Ni, the matrix #1 composition is determined to be 64.8 at.% Fe, 16.8 at.% Cr and 12.1 at.% Ni.

This slight depletion of Cr and enrichment of Fe and Ni in the matrix #1 region is noticeably enhanced at matrix #2 region. The Cr depletion and Ni enrichment at grain boundary area and phase transformation according to that will be discussed in preparation [102]. Figure 3.5 b) shows the outer oxide and matrix region observed in Tip 2. The outer oxide consists of two different oxide regions. The outer oxide #1 is a Fe-rich (Fe,Cr) oxide of 50.3 at.% O, 39.8 at.% Fe, and 8.05 at.% Cr composition. The outer oxide #2 is Cr-rich oxide with 58.6 at.% O and 39.2 at.% Cr. The matrix composition of Tip 2 is almost identical to the composition of matrix #1 of Tip 1. Figure 3.5 c) shows the outer oxide, the inner oxide and the matrix region observed in Tip 3. The outer oxide of Tip 3 consists of two different oxide phases. Both of them are (Fe,Cr) oxide, but one is a Cr-rich (Fe,Cr) oxide and the other is Fe-rich (Fe,Cr) oxide. The composition of these oxides are 55.9 at.% O, 19.1 at.% Fe and 23.3 at.% Cr for outer oxide #1 and 52.4 at.% O, 32.4 at.% Fe and 12.0 at.% Cr for outer oxide #2. The Cr-rich oxide found in Tips 1 and 2 is not found in the outer oxide in Tip 3. The inner oxide which composed beneath the original matrix surface is Cr-rich (Fe,Cr) oxide with 51.8 at.% O, 14.7 at.% Fe, and 28.4 at.% Cr. The matrix composition is 63.8 at.% Fe, 7.27 at.% Cr and 22.0 at.% Ni.

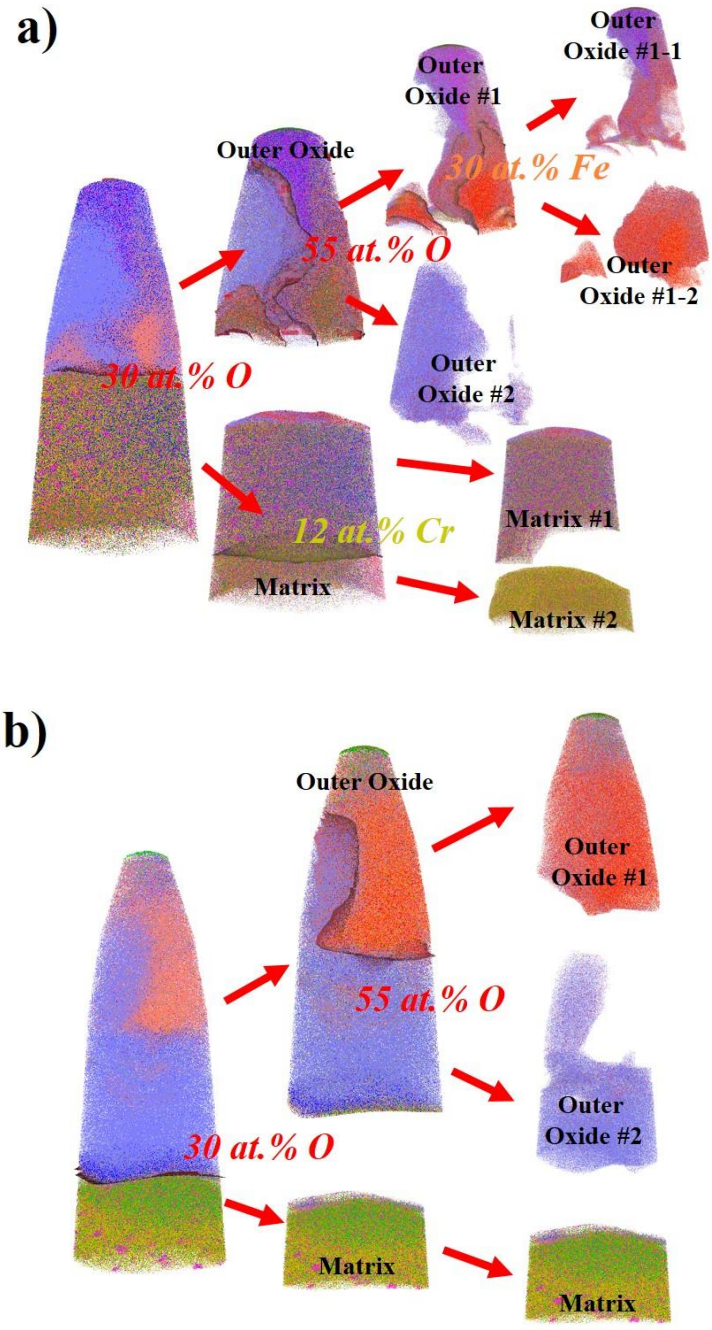
a)
Outer Oxide
Outer Oxide #1
Outer Oxide #1-1
30 at.% Fe
55 at.% O
Outer Oxide #1-2
Outer Oxide #2
30 at.% O
12 at.% Cr
Matrix
Matrix #1
Matrix #2
b)
Outer Oxide
Outer Oxide #1
55 at.% O
Outer Oxide #2
30 at.% O
Matrix
Matrix

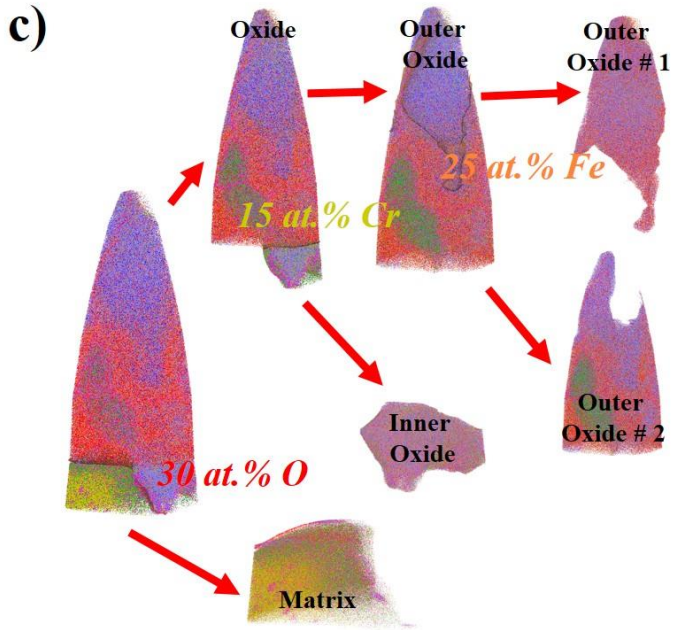

Figure 3.5 3D elemental maps of the iso-concentration surface acquired from the original data set a) Tip 1, b) Tip 2 and c) Tip 3. O (red), Fe (orange) and Cr (dark yellow) iso-concentration surfaces are introduced to visualize the positions of the matrix/oxide interface region and the different outer oxide types.

Table 3.2 Chemical composition (at.%) of the oxides and matrix in each tip shown in Figure 3.5 as measured using APT. The error bars represent 2σ standard deviation.

		O	***Fe***	***Cr***	***Ni***	***Mn***	***Cu***
Tip 1	Outer Oxide #1-1	51.52 ±0.062	17.25 ±0.033	22.97 ±0.045	2.04 ±0.010	3.10 ±0.013	2.66 ±0.012
	Outer Oxide #1-2	48.75 ±0.083	38.93 ±0.074	8.23 ±0.028	1.32 ±0.011	1.35 ±0.011	0.27 ±0.005
	Outer Oxide #2	58.27 ±0.091	1.79 ±0.012	38.91 ±0.071	0.15 ±0.004	0.23 ±0.004	0.14 ±0.003
	Matrix #1	1.81 ±0.004	64.88 ±0.032	16.87 ±0.013	12.17 ±0.011	0.89 ±0.002	2.68 ±0.005
	Matrix #2	0.68 ±0.005	78.96 ±0.072	4.53 ±0.012	13.35 ±0.024	0.16 ±0.002	1.71 ±0.007
Tip 2	Outer Oxide #1	50.31 ±0.092	39.84 ±0.087	8.05 ±0.031	0.99 ±0.011	0.26 ±0.005	0.25 ±0.005
	Outer Oxide #2	58.63 ±0.095	1.81 ±0.014	39.21 ±0.076	0.07 ±0.002	0.09 ±0.003	0.03 ±0.002
	Matrix	0.65 ±0.005	69.76 ±0.077	13.25 ±0.035	11.95 ±0.036	0.47 ±0.004	2.58 ±0.012
Tip 3	Outer Oxide #1	55.96 ±0.047	19.15 ±0.021	23.34 ±0.035	0.46 ±0.003	0.34 ±0.003	0.21 ±0.002
	Outer Oxide #2	52.46 ±0.025	32.46 ±0.022	12.03 ±0.014	1.40 ±0.003	0.23 ±0.001	0.50 ±0.002
	Inner Oxide	51.84 ±0.051	14.74 ±0.027	28.45 ±0.043	2.19 ±0.009	0.19 ±0.003	1.01 ±0.006
	Matrix	2.01 ±0.009	63.84 ±0.074	7.27 ±0.018	22.05 ±0.033	0.24 ±0.003	3.55 ±0.012

Figure 3.6 shows 1D composition profiles across the interfaces between the oxides and the matrix in Tips 1~3. The profiles are plotted along cylinders of 15 nm diameter in the directions indicated by the red arrow in Figure 3.6. Figure 3.6 a) and c) show that a thin Cr-rich oxide (both outer oxide #2) with around 40 nm thickness was formed on the matrix. Although the depths of the observed matrix regions are different, the composition profiles are similar. No Ni can be detected, indicating that the oxide layer comprises an inner layer of Cr_2O_3. Thinner Fe-rich $(Fe,Cr)_3O_4$ oxide layers are formed at the top of the outer oxide (see Figure 3.6 b) and c)) and reveal a Cr_2O_3 oxide in the bottom of the outer oxide. In the matrix near the matrix/oxide interface, a strong enrichment of Ni (depletion of Cr) up to 20 nm from the interface is found. Ni enrichment at the matrix/oxide interface is correlated with a characteristic Cr depleted region. This Ni enrichment was previously observed [87] and predicted by quantum chemical molecular dynamics simulation [103].

In Tip 3, the formation of a thicker Fe-rich $(Fe,Cr)_3O_4$ oxide (outer oxide #1 and #2) is observed (see Figure 3.6 d)) because no protective Cr_2O_3 oxide is formed on the surface. The composition of the inner oxide layer in Figure 3.6 e) corresponds to Cr-rich $(Cr,Fe)_3O_4$, where a Ni-enrichment is also detected at the interface between the matrix and the inner oxide layer because of a selective dissolution reaction of Fe and Cr [104].

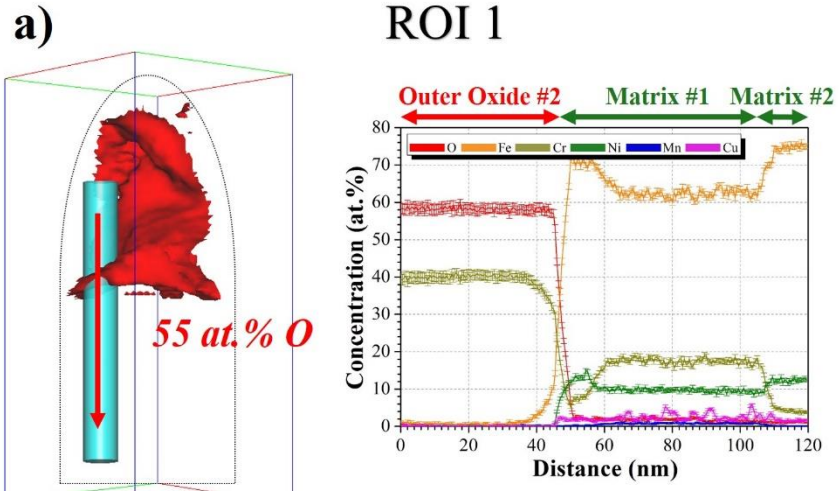
a)
ROI 1
55 at.% O
Outer Oxide #2
Matrix #1
Matrix #2
O
Fe
Cr
Ni
Mn
Cu
Concentration (at.%)
Distance (nm)

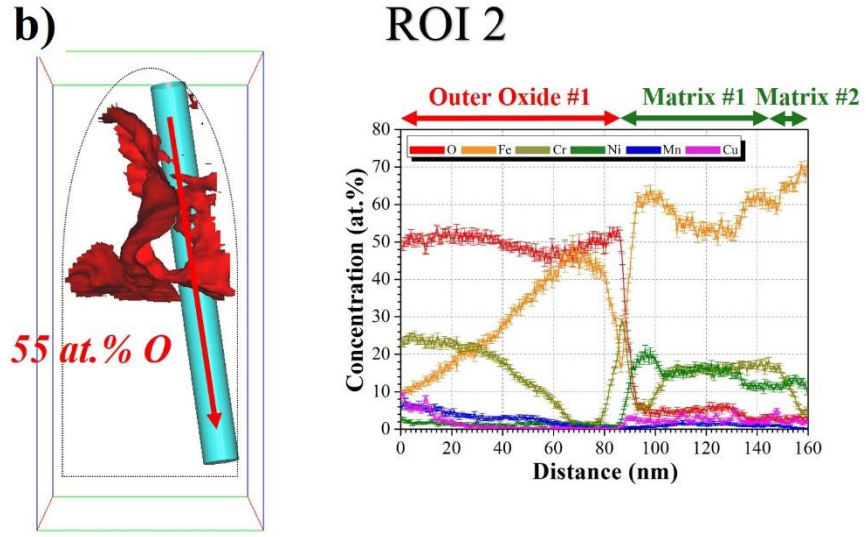
b)
ROI 2
55 at.% O
Outer Oxide #1
Matrix #1
Matrix #2
O
Fe
Cr
Ni
Mn
Cu
Concentration (at.%)
Distance (nm)

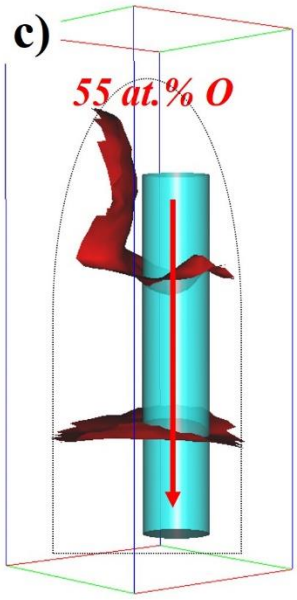
c)
55 at.% O

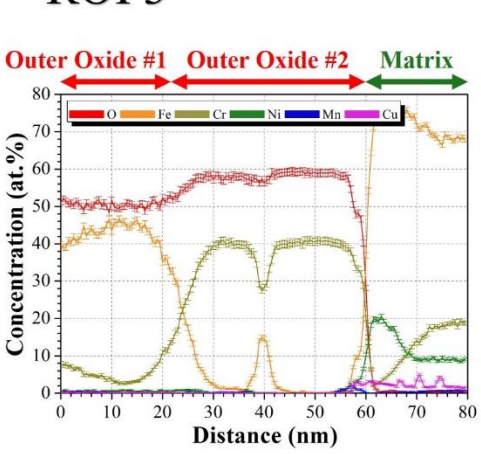
ROI 3
Outer Oxide #1
Outer Oxide #2
Matrix
O
Fe
Cr
Ni
Mn
Cu
Concentration (at.%)
Distance (nm)

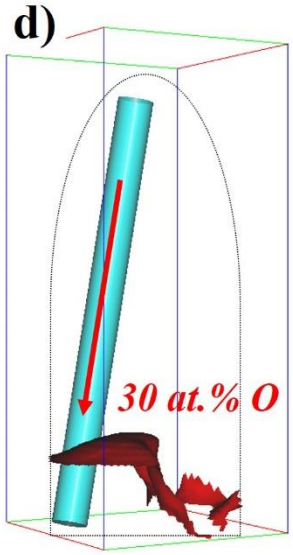
d)
30 at.% O

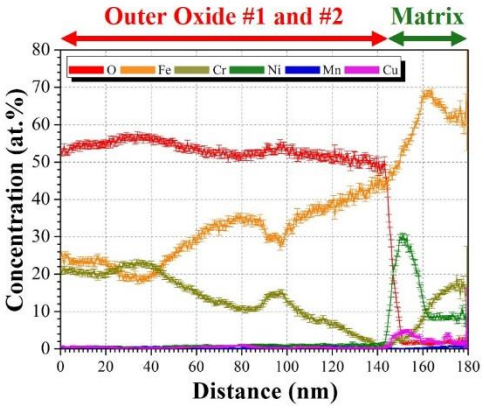
ROI 4
Outer Oxide #1 and #2
Matrix
O
Fe
Cr
Ni
Mn
Cu
Concentration (at.%)
Distance (nm)

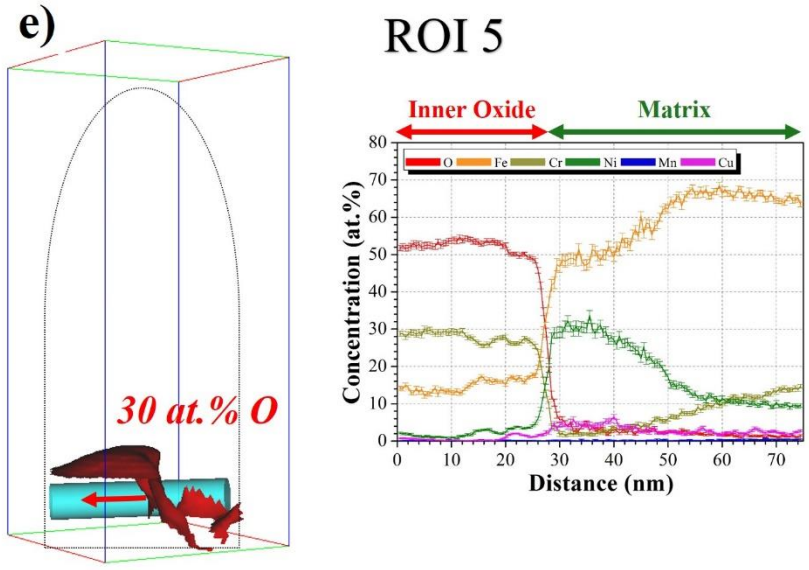

Figure 3.6 Elemental concentration 1D profiles (fixed bin width of 0.5 nm) along the region of interest (ROI) taken across the oxide and matrix from Tip 1 a) and b), Tip 2 c) and Tip 3 d) and e). O (red) iso-concentration surfaces are introduced to visualize the positions of the matrix/oxide interface region and the different outer oxide types. 1D profiles of all tips determined within a cylinder with a diameter of 15 nm. The red arrows mark the directions in which the concentration profiles are drawn. The error bars represent σ statistical error due to the limited number of atoms in the sample volume.

3.3.1.3 Oxide structure analysis using TEM

The local microstructure in the MG sample after 30 min oxidation was studied by TEM bright-field (BF) imaging (see Figure 3.7) and the corresponding selected-area diffraction patterns (SADP). Following the APT analysis presented above we emphasize here that the region, analyzed by TEM, includes both, the oxide and the original matrix. The region observed by TEM includes the same oxide and matrix grains analyzes by APT in the previous section (marked by blue boxes in Figure 3.4 a)). Also both methods probed the same grain boundary, however, the TEM sample was taken at a slightly different position along the same interface than the APT samples.

Figure 3.7 a) shows BF image and SADPs taken near the grain boundary. The BF image contains portions of the grain boundary, the matrix and the outer oxide. To prevent authors misunderstanding, the SADPs are numbered; as follows SADP 1 was taken from the outer oxide just beside grain boundary and SADP 2 was taken from the next outer oxide. The outer oxides near grain boundary have inhomogeneous thickness between 20 and 50 nm. Both SADPs indicate that the outer oxide layer consists of rhombohedral crystal structures with zone axis [210]. It corresponds to the chemical composition of Cr_2O_3 acquired by APT analysis of previous section.

Figure 3.7 b) shows a BF image and SADPs taken from an intra grain

region (4.4 μm away from the grain boundary). The oxide layer formed on this intra grain region had a double-layer structure, which is consistent with the result reported in the previous study [84]. The interface between the layers was clearly identified as an almost straight line between the two regions with different contrasts. SADP 3 was taken from the outer oxide 4.4 μm away from the grain boundary and SADP 4 was taken from the inner oxide beneath the oxide of SADP 3. The outer oxide formed at the intra grain has 100 nm thickness and shows spinel crystal structure with zone axis [111]. The chemical composition acquired by APT analysis corresponds to Fe_2CrO_4. The inner oxide formed beneath the outer oxide has thinner thickness (~50 nm) than outer oxide and shows same spinel crystal structure with zone axis [100]. The chemical composition acquired by APT analysis corresponds to $FeCr_2O_4$. This TEM results reveal that the outer and inner oxide of intra grain area has same spinel crystal structure in spite of that both oxides are difference in chemical composition.

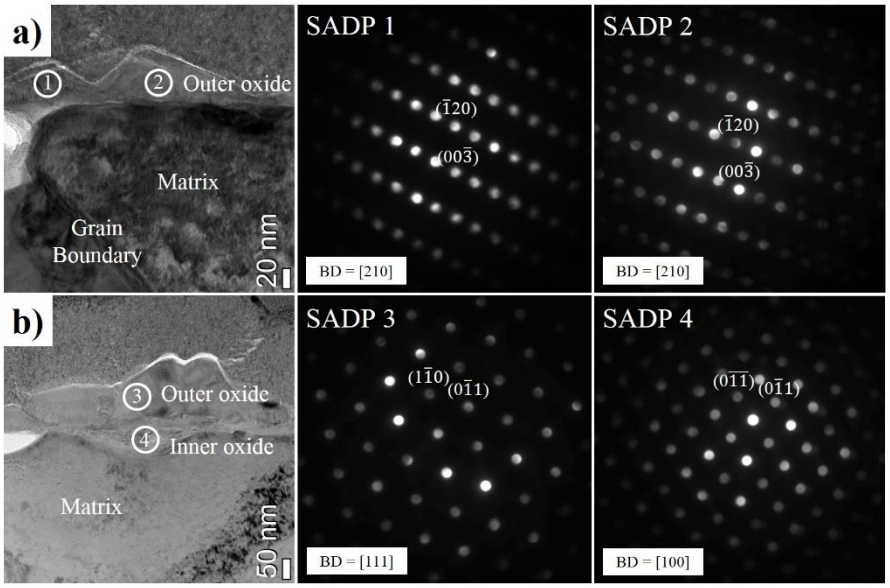

Figure 3.7 TEM micrographs and the corresponding SADP taken obtained in the medium grain sample after 30 min of oxidation at 700 ℃ in air with 20% water vapor; a) Cross sectional TEM image of the oxide layer composed on the near grain boundary region (SADP 1 and 2: Cr_2O_3 with zone axis of [210]), b) Cross-sectional TEM image of the oxide layer on the intra-grain region (SADP 3: Fe_2CrO_4 with zone axis of [111], SADP 4: $FeCr_2O_4$ with zone axis of [100]).

3.3.2 Early oxidation (~12 h) stage

3.3.2.1 Grain size & CSLBs analysis using EBSD

In Figure 3.8, average grain sizes of all samples before oxidation were determined from EBSD maps. Average grain size and number fraction of CSL grain boundaries were calculated by average of three different areas in each sample [84]. As seen in Figure 3.3, ∑3 CSL grain boundaries do not show any different oxidation behavior from the intra grain region. Furthermore, in the following discussion for the role of grain boundary for the oxidation kinetics, only high-angle grain boundaries will be taking into account. Therefore between the average grain sizes presented in Figure 3.8, neglecting ∑3 CSL grain boundaries are meaningful sizes values and the values are determined as 27 μm, 17 μm and 8 μm for the LG, MG and SG samples, respectively. The ∑3 CSL grain boundary fractions observed for all samples were kept similar and more than 50% of the total grain boundary line fraction.

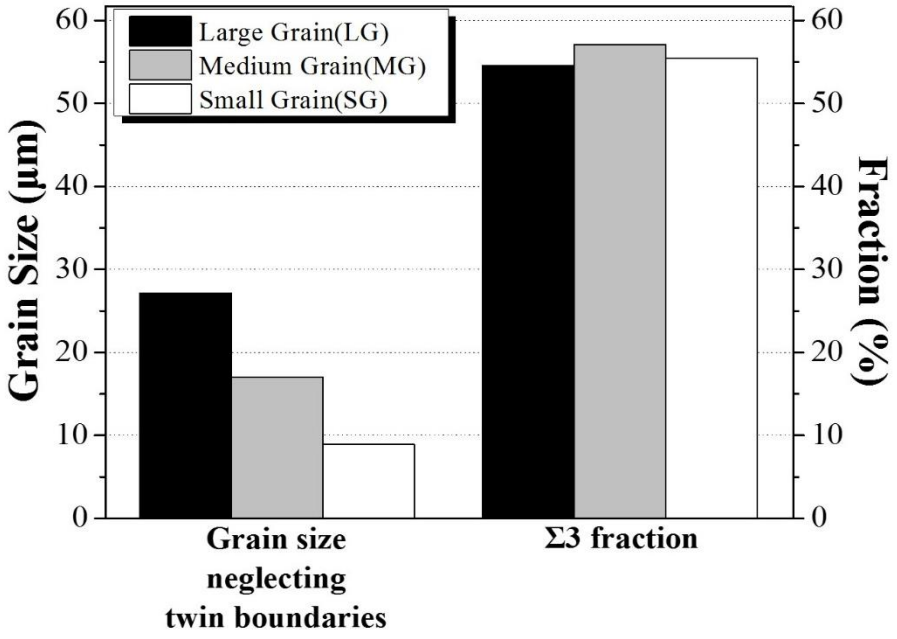

Figure 3.8 Comparison of the LG, MG and SG samples in terms of grain size and Σ3 boundary number fraction.

3.3.2.2 Mass gain analysis for the study of oxidation kinetics

The growth kinetics of the oxide layers formed on the steels was investigated by measuring the mass gain per unit area versus oxidation time. Figure 3.9 shows that there is a clear difference in the oxidation rates depending on the grain size of the samples.

Figure 3.9 a) shows the mass gain curves of Cu added austenitic stainless steels with different grain sizes oxidized at 700 °C in air with 20% water vapor for 28 h. Slight oxide spallation during cooling to room temperature occurred for the LG sample. The curves show that the SG sample, which has the smallest average grain size (8 µm) has the largest mass gain among all samples until 2 h oxidation. However, for times beyond 2 h the mass gain decreases drastically and approaches a saturation level, indicating a stable oxidation in the oxidation resistance. On the contrary, the LG and MG samples exhibit a lower mass gain as compared to SG sample for oxidation times ≤ 2 h, whereas beyond 2 h oxidation time the mass gain of both samples is larger compared to that observed for the SG sample. This large value is probably resulted from the formation of non-protective Fe-rich oxides at the intra grain region. Hence, in turn, a critical grain size seems to be required to cover the surface with a protective Cr_2O_3 oxide, which will be discussed later in more detail. All mass gain curves show a strong increase during the initial stage of oxidation (≤ 1 h), followed by a decrease in mass gain in the later stages of

oxidation.

In the previous study [84], we reported that the long-term oxidation (~500 h) mass gain observed for the SG sample was three times smaller than the mass gain values of MG sample and more than seven times smaller than LG sample.

The mass gain curves follow a parabolic rate law given by $(\Delta M/S)^2 = A + K_p t$ [105-107], where ΔM is the mass gain, S is the unit area, A is a constant, K_p is the parabolic rate constant and t is the time. We plotted the square of mass gain versus time to determine the parabolic rate constant which indicate the changes in the oxidation mechanism. Figure 3.9 b) shows that at the first regime (0~2 h), the parabolic rate constants K_p of the SG sample is similar to the values found for the growth of the Cr_2O_3 oxide in 18/8 type stainless steels [108]. In the SG sample, a straight line is found after the first regime (2 h~) and no evidence for a transition in the oxidation kinetics is found. In contrast, for the LG and MG samples, the parabolic rate constants K_P show continuously increasing slopes after the first stage. The early stage oxidation kinetics of both samples are very similar. The parabolic constants determined for the second regime (2~12 h) correspond well to the value of Fe-rich oxides reported in the previous study [78]. The rate constants K_p determined from the slope of the linear plots in the first and second stages are presented in Table 3.3. Between 2 h and 12 h oxidation, the plots in Figure 3.9 b) can be fitted by

straight lines, where rate constant values of 0.05018 $mg^2cm^{-4}h^{-1}$, 0.04868 $mg^2cm^{-4}h^{-1}$ and 0.00574 $mg^2cm^{-4}h^{-1}$ are calculated for the LG, MG and SG samples, respectively. Thus, the oxidation rates after 2 h of oxidation at 700 ℃ in air with 20% water vapor decrease in the following order; LG > MG > SG.

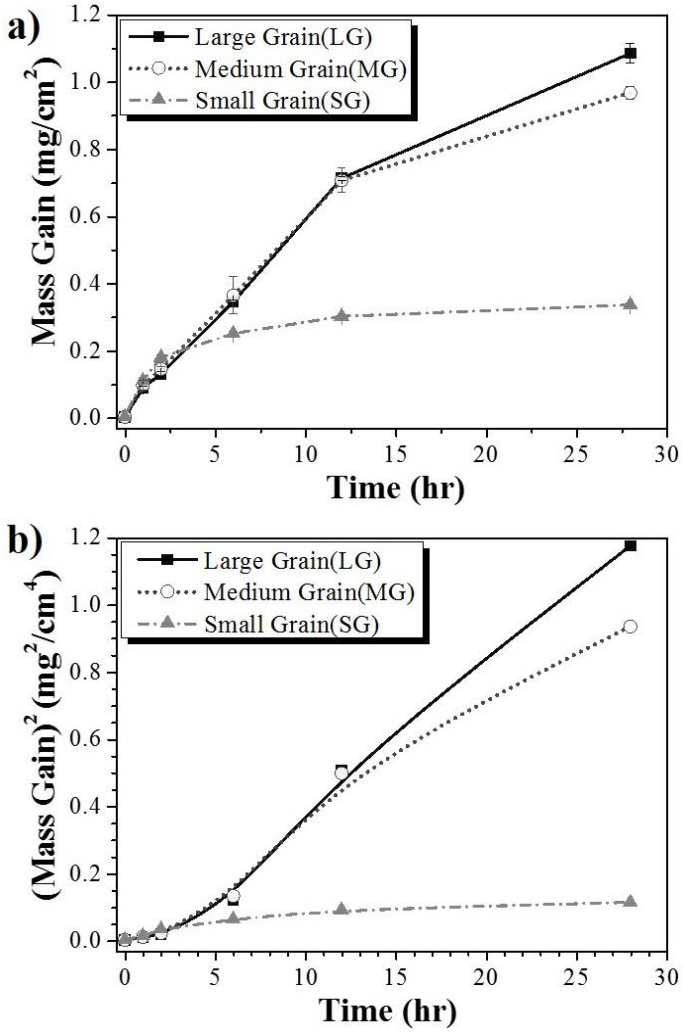

Figure 3.9 a) Mass gain vs. time curve, b) Quadratic function of the mass gain vs. time curve obtained for the large grain, medium grain and small grain samples over 28 h of oxidation at 700 ℃ in air with 20% water vapor. The average grain sizes of the samples (not including the ∑3 boundaries) were 27, 17 and 8 μm for the LG, MG and SG samples, respectively.

Table 3.3 Calculated parabolic rate constants.

Samples	Parabolic rate constant ($mg^2cm^{-4}h^{-1}$)
LG (27 μm)	0.00826 (0~2 h), 0.05018 (2~12 h)
MG (17 μm)	0.01022 (0~2 h), 0.04868 (2~12 h)
SG (8 μm)	0.01581 (0~2 h), 0.00574 (2~12 h)

3.3.2.3 Oxide Surface morphology analysis using SEM

The SEM images in Figure 3.10 show the surfaces of the MG and SG samples prior to oxidation and also after oxidation for 6 h and 12 h, respectively. For the MG sample, our previous investigation with EDS [84] showed that the oxide layer consists of two different oxide complex after 500 h oxidation. The overall oxide surface morphology of the MG sample seems to be very similar to that of the SG sample. The thicker nodule-like features on the surface of intra grain regions are Fe-rich oxides and the bottom regions near the grain boundaries are thin Cr-rich oxides. Such selective oxidation behavior was also reported by other authors [63, 64, 70, 72] in austenitic stainless steels by EDS analysis. It was found that the nodules also became progressively enriched in Fe and the number density of nodules that formed increased upon further oxidation.

Figure 3.10 a) shows that Fe-rich nodules only form on the intra grain regions. However, they did not form on every grain and they never formed on grain boundaries. This means that size and distribution of these nodules depend on the matrix grain structure. With increasing oxidation time, single nodules within the same intra grain region tend to agglomerate and merge. As mentioned before, the surface is not covered entirely by Fe-rich outer oxide nodules, but spallation occurs at some places. In contrast, the entire surface of the SG sample is covered with only Cr-rich oxides (see Figure 3.10 b)). The

oxide formed over the entire surface is a thin and adherent oxide layer similar to that formed over grain boundaries of the MG sample. There are no Fe-rich nodules that formed on the surface of the SG sample.

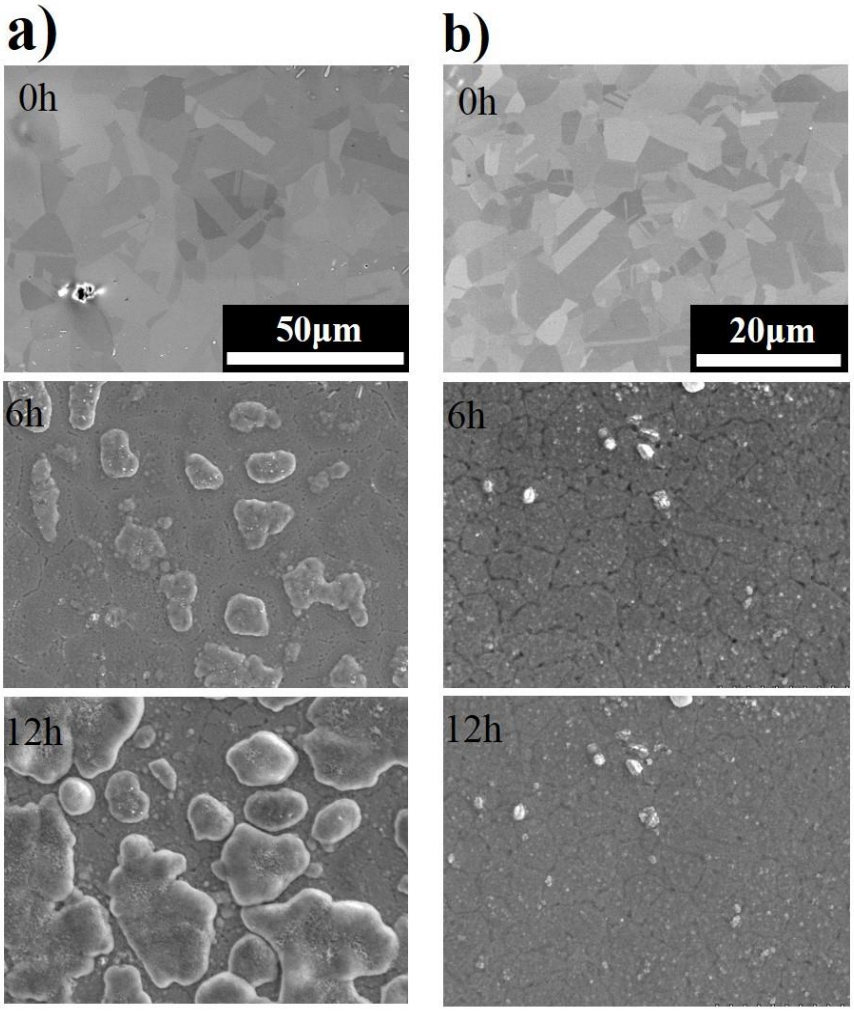

Figure 3.10 Secondary electron (SE) images obtained on the surface of the oxide layer formed after oxidation at 700 ℃ in air with 20% water vapor; a) MG and b) SG samples. The average grain sizes (not including the ∑3 boundaries) were 17 and 8 µm for the MG and SG samples, respectively.

3.3.2.4 Oxide phase analysis using EBSD

Figure 3.11 is the SE image acquired from the 1 h oxidized MG sample and the oxide phases identified by EBSD in the intra grain and grain boundary region. The oxides formed at the initial stage of oxidation of MG sample are quite different from site to site. At the intra grain region, where a certain distance away from the grain boundary, nodule type oxide forms. The EBSD point analyses reveal the abundance of thin Cr_2O_3 oxide with a small amount of $CrMn_2O_4$ spinel oxide at the grain boundary region. On the contrary at the intra grain area, nodule type thick oxides form, which are identified as Fe_3O_4 and Fe_2O_3 by EBSD. In coarse grains, iron oxide covers the grain interior region but is located about 4 μm from grain boundaries. The grain boundary region had a greater near-surface concentration of Cr compared to the grain interior. Cr_2O_3 is formed at the grain boundary region during the initial stages of oxidation. It increases oxidation resistance at high temperature when the grain size is below a critical value.

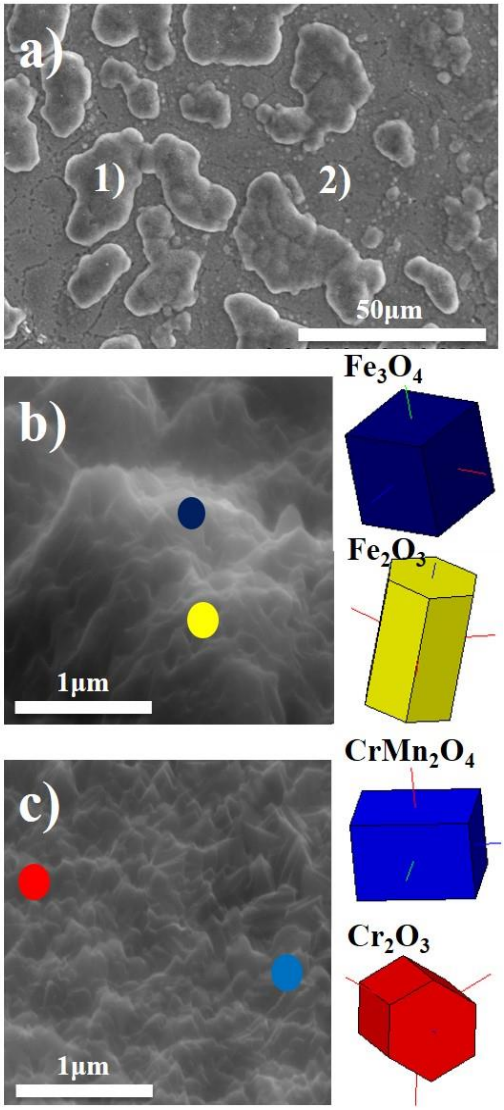

Figure 3.11 Surface of the scale formed on MG sample after 1 h oxidation at 700 ℃ in air with 20% water vapor; a) SE image, b) Oxide phases identified by EBSD from grain interior region (site 1 of a)), c) Oxide phases identified by EBSD from grain boundary region(site 2 of a)).

3.3.3 Long term oxidation (~500 h) stage

3.3.3.1 Phase analysis using X-ray diffraction

X-ray diffraction patterns of samples oxidized for 100 h are shown in Figure 3.12. By several previous studies, the presence of the austenite stainless steel AISI 304 (Joint Committee Powder Diffraction Standard file: JCPDS 33-0397), α-Fe (JCPDS 85-1410), Cr_2O_3 (JCPDS 38-1479), Fe_2O_3 (JCPDS 33-0664), $Mn_{1.5}Cr_{1.5}O_4$ (JCPDS 33-0892), $FeCr_2O_4$ (JCPDS 34-0140) and $CuFe_2O_4$ (JCPDS 25-0283) spinel phases during high temperature oxidation are confirmed [56, 62, 101].

Figure 3.12 a) shows Cr_2O_3 peaks, which appear together with the $Mn_{1.5}Cr_{1.5}O_4$ peaks from the beginning of the oxidation in the LG sample. Peaks belonging to the austenite matrix are still observed because of the low thickness of the oxide layers. After 6 h of oxidation, phase transition at the sample surface is observed. The initially formed oxides (Cr_2O_3 and $Mn_{1.5}Cr_{1.5}O_4$) have completely disappeared and only peaks belonging to Fe-containing oxides such as Fe_2O_3 and $FeCr_2O_4$ are observed.

Figure 3.12 b) shows that in the MG sample as well as the LG sample, Cr_2O_3 is initially formed followed by Fe_2O_3 occurring during the later stages. Also, a peak pertaining to austenite is observed, since the Fe-rich oxide does not cover the entire surface after oxidation for 12 h, as also shown in the SE

image in Figure 3.10 a).

Figure 3.12 c) shows that the XRD patterns of the SG sample reveal that a Cr_2O_3 layer is immediately formed with $Mn_{1.5}Cr_{1.5}O_4$ at the beginning of the oxidation. No Fe-containing oxides are formed until the end of the oxidation test.

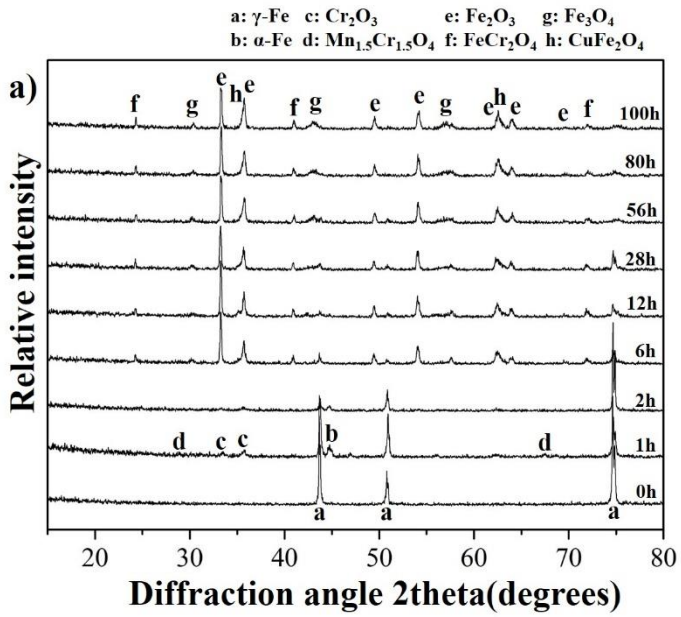
a: γ-Fe c: Cr_2O_3 e: Fe_2O_3 g: Fe_3O_4
b: α-Fe d: $Mn_{1.5}Cr_{1.5}O_4$ f: $FeCr_2O_4$ h: $CuFe_2O_4$
a)
Relative intensity
100h
80h
56h
28h
12h
6h
2h
1h
0h
20 30 40 50 60 70 80
Diffraction angle 2theta(degrees)

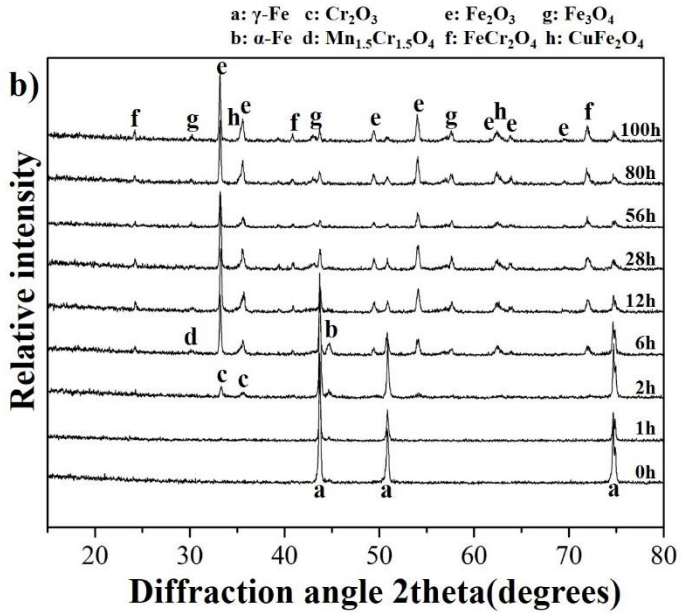
a: γ-Fe c: Cr_2O_3 e: Fe_2O_3 g: Fe_3O_4
b: α-Fe d: $Mn_{1.5}Cr_{1.5}O_4$ f: $FeCr_2O_4$ h: $CuFe_2O_4$
b)
Relative intensity
100h
80h
56h
28h
12h
6h
2h
1h
0h
20 30 40 50 60 70 80
Diffraction angle 2theta(degrees)

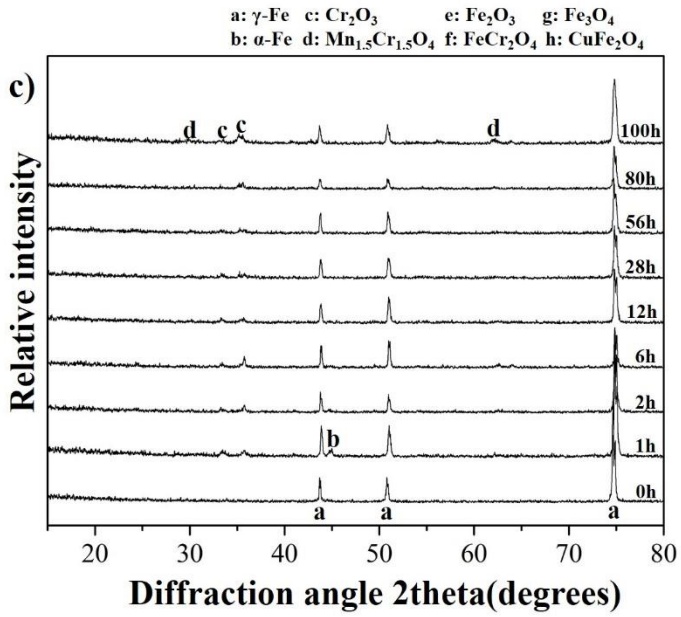

Figure 3.12 XRD analysis of the oxides performed on a) LG, b) MG and c) SG samples over 100 h of oxidation at 700 ℃ in air with 20% water vapor. The average grain sizes of the samples (not considering the ∑3 boundaries) were 27, 17 and 8 μm for the LG, MG and SG samples, respectively.

3.3.3.2 Surface and cross section of oxide composition analysis using EDS

The surface morphologies of the oxides formed on the Cu added austenitic stainless steels are shown in Figure 3.13. In LG sample, the entire surface was covered with Fe-rich oxides. In SG sample, the entire surface is covered with Cr-rich oxides. But, in MG sample, both Fe-rich oxides and Cr-rich oxides are mixed. In order to analyze the oxide composition, EDS analyses on the sample surface were performed in MG sample. Figure 3.14 shows EDS spectrums acquired from the region of Figure 3.13 b). It shows the presence of O, Cr and Fe. According to the EDS analyses, two types of oxides are formed on the outer surface; the Cr and Fe contents in scale on nodule is ~2 wt.% Cr and ~50 wt.% Fe (spectrum 1 and spectrum 2). It reveals that Fe-rich oxide has formed in the nodule area. While, the Cr and Fe contents of the bottom side oxide is ~18 wt.% Cr and ~20 wt.% Fe (spectrum 3 and spectrum 4) show that the bottom oxide is enriched in Cr. Size and distribution of these nodules depended on the grain size of the samples. The size of nodules increased with increasing oxidation time, on the coarse grained sample. During further oxidation, the nodules became progressively enriched in iron. The main oxide formed on the outer surface of the coarse grained is iron oxide while a Cr-rich oxide is formed on the fine grained sample. MG sample shows mixture of both oxides. Fe_2O_3 outer oxide has formed, but it did not cover the entire surface.

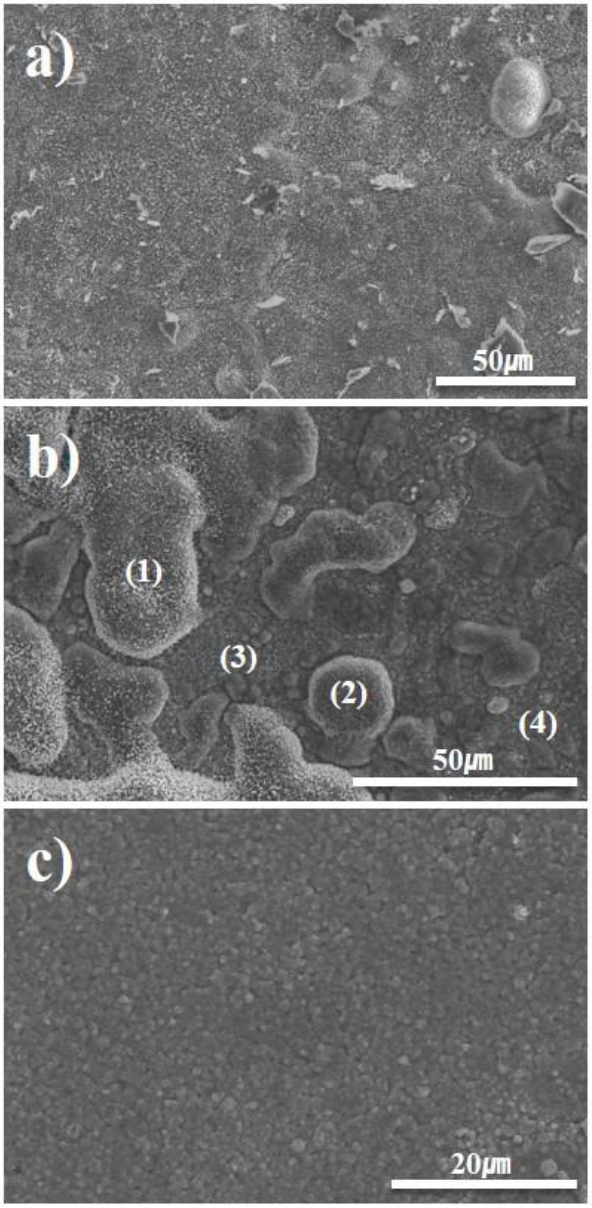

Figure 3.13 Secondary electron (SE) images obtained on the surface of the scale formed after 500 h oxidation at 700 ℃ in air with 20% water vapor. a) LG sample, b) MG sample, c) SG sample.

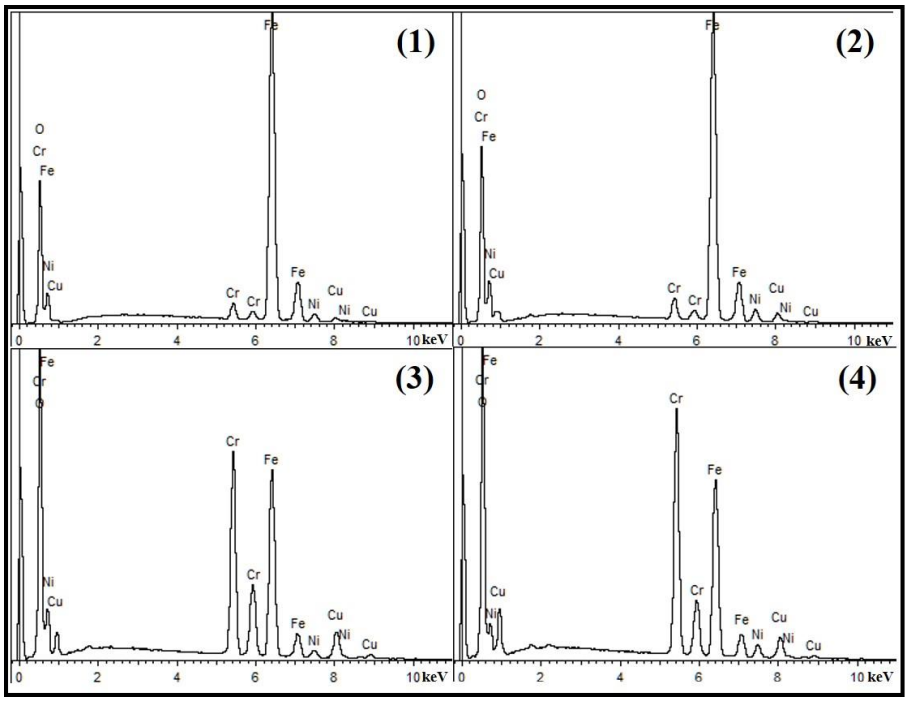

Figure 3.14 EDS spectrums acquired from the oxide scale formed on the MG sample surface (Figure 3.12 b) area) after 500 h oxidation at 700 ℃ in air with 20% water vapor.

The Cross sectional microstructure of oxide scale of different grain sized samples is shown in Figure 3.15. The contrast difference in BSE image reveals that the LG sample has outer/inner dual layer structure but that SG sample has single outer oxide. During oxidation, the inner and outer oxide becomes larger in size. After 500 h in LG sample, Fe_2O_3 outer oxide covers the entire sample surface but in one step and annealed sample, a thin Cr_2O_3 oxide layer covers entire surface of the sample. Figure 3.15 includes the through thickness EDS line profiles of O, Fe, Cr, Ni, Mn and Cu to identify the oxide phases. In LG sample, the outer layer composes of Fe_2O_3 and the inner layer composes of a $FeCr_2O_4$ spinel oxide. Also, there is thin Cr_2O_3 oxide in the adherent subscale. But in the SG sample, only a thin protective Cr_2O_3 scale is formed. In MG sample, at some site, this oxide layer is not totally protective. Then it is converted to an outer scale of iron oxide and an inner scale of mixed oxide phases of Fe, Cr, Mn and Ni similar to the oxide nodules formed in LG sample.

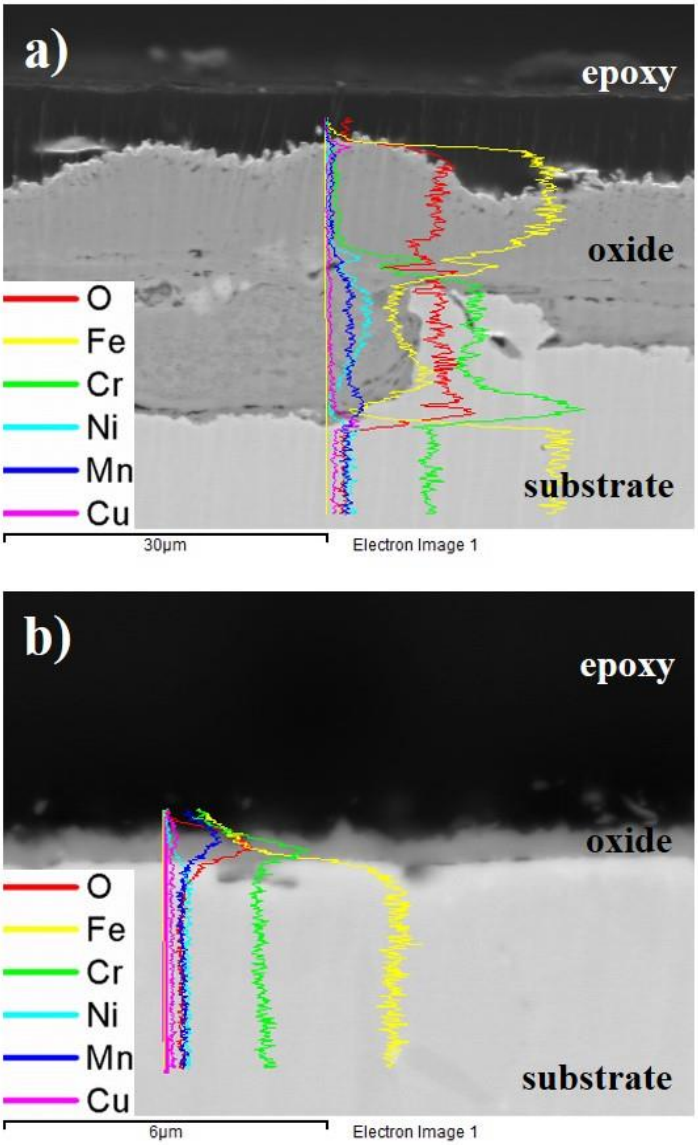

Figure 3.15 The BSE images and EDS line profile obtained from cross-sections of the scales formed after 500 h oxidation at 700 ℃ in air with 20% water; a) LG sample, b) SG sample.

3.4 Discussion

3.4.1 Initial oxidation (~30 min) stage

3.4.1.1 Oxidation of surface and grain boundary regions

The cross sectional oxide layer distribution in the MG sample after 30 min oxidation is schematically illustrated in Figure 3.16. APT (as shown in Figure 3.5 and 3.6) and TEM (as shown in Figure 3.7) analysis indicate that the outer oxide layer consists of Fe-rich oxide and Cr-rich oxide with rhombohedral crystal structure. The outer oxide layer probed near random high angle grain boundaries is very thin (90~100 nm thick as shown in Figure 3.4), but it still has a duplex-layer structure. The layers are mainly composed of protective Cr_2O_3 with Fe-rich $(Fe,Cr)_3O_4$, oxide on top, which contains small amounts of Ni, Mn and Cu. The formation of a uniform protective oxide can be clearly seen in Figure 3.3. This layer of protective oxides begins to form along the grain boundaries but not in the intra grain region. Furthermore, this layer prevents inner oxidation in the matrix, acts as a diffusion barrier against oxygen. On the other hand, the outer oxide layer that formed ~4 μm away from the random grain boundaries consists of a thick Fe-rich $(Fe,Cr)_3O_4$ oxide with a spinel crystal structure containing small amounts of Ni, Mn and Cu. Furthermore, an inner oxide layer with a stoichiometry of $FeCr_2O_4$ is formed beneath original surface, which has same spinel crystal structure. Since there is no protective

Cr_2O_3, these oxide layer grows continuously and forms a thicker outer oxide and inner oxide layer in the later stage of oxidation [84].

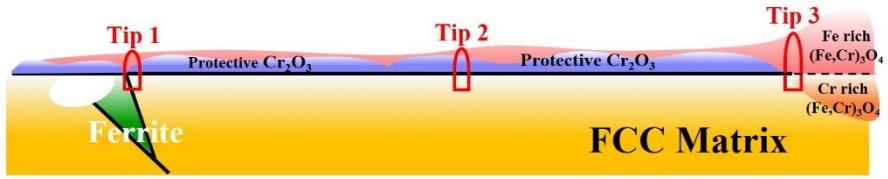

Figure 3.16 Schematic illustration of the oxide layer formed on the surface of the medium grain sample after 30 min of oxidation at 700 ℃ in air with 20% water vapor.

Ni is present in the entire oxide layer (as shown in Figure 3.4 e)) and is also enriched at the matrix/oxide interface (as shown in Figure 3.6). Wood [109] observed that small amounts of Ni enter the oxide layer in Ni-Cr alloys although it shows relatively weak chemical attraction to oxygen when compared to Cr. Ni enrichment at the matrix/oxide interface could be related to different diffusion rates, as the lattice diffusion rate of Ni is reported to be slower than that of Cr and Fe in Fe-Cr-Ni alloys ($D_{Cr} > D_{Fe} > D_{Ni}$) [110]. Although the origin of Ni enrichment is thus not clear, this result reveals that selective diffusion of Fe and Cr occurs at the matrix/oxide interface.

Minor amounts of Mn and Cu are also detected in the outer oxide layer. Mn is locally enriched in the outer oxide, as detected by APT. Caplan [111] showed that Mn has a detrimental effect on the oxidation resistance of ferritic stainless steels because of the formation of a $(MnCr)_3O_4$ spinel phase. Although the Mn content in Cu added austenitic stainless steel as studied here is relatively low, the presence of Mn in the outer oxide can be explained by relatively fast diffusion of Mn through the Cr_2O_3 oxide [112]. The formation of $(MnCr)_3O_4$ spinel oxide on top of a Cr_2O_3 oxide layer is generally observed due to the outward diffusion of Mn from the bulk through the Cr_2O_3 oxide [113]. According to the APT analysis results from the outer oxide #1 of Tip 1 in Figure 3.4 e) and 3.6 b), it is clear that Mn is enriched in the outer oxide especially along the grain boundary of oxide. This rapid Mn diffusion along grain

boundary of Cr_2O_3 layer elucidate the formation a Mn-rich oxide on the outer surface of the Cr_2O_3 layer.

The APT analysis result also shows the enrichment of Cu at the top surface of the outer oxide. It coincides with author's previous observation that the Cu addition in austenite stainless steel induces Cu-containing spinel oxide at top surface after long-term oxidation [101].

3.4.1.2 Initial oxidation mechanism

In the initial stage of oxidation, metal cations in the alloy and oxygen on the ambient gas react to form an oxide layer, where the oxidation mechanism is strongly dependent thermodynamic and kinetic boundary conditions. For the thermodynamic predictions, the relative thermodynamic stability of the oxides should be considered. Regarding the of ΔG^0-T curves obtained by Ellingham-Richardson (Figure 3.17 a)), the free enthalpy ΔG^0 for Cr_2O_3 is far more negative than ΔG^0 for FeO, Fe_2O_3 or Fe_3O_4 at temperatures below 1300 K. The Gibbs free energy of the oxides Fe_2O_3 and Cr_2O_3, are almost -310 and -580 kJ/mol at 973 K, respectively. Thus, formation of Cr_2O_3 is thermodynamically favored. The oxide layer formed on austenitic stainless steels is also predicted by thermodynamic calculations using the FactSage software with a database of the FactPS, FToxide and FTlite. Figure 3.17 b) shows the calculation results of phase stabilities for Fe-Cr-Ni steels at 700 ℃ according to the oxygen partial pressure and the Cr concentration. In this condition, Cr_2O_3 is present at the lowest oxygen potential, while Fe_3O_4 and $FeCr_2O_4$ become stable with increasing oxygen partial pressure and Fe_2O_3 and $FeCr_2O_4$ mainly exist at high oxygen partial pressure. It is evident that the layered structure of the oxide formed on the Fe-Cr-Ni steels. In terms of oxidation kinetics for such Cr-containing alloy, the outward diffusion of cation from the alloy and the inward diffusion of oxygen from the ambient gas compete against each other.

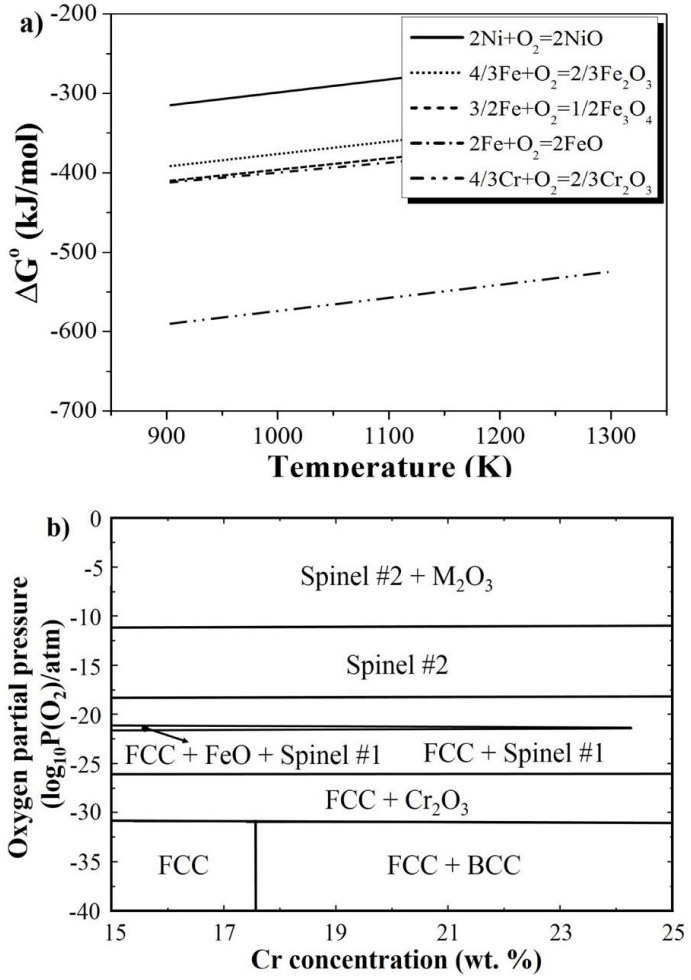

Figure 3.17 a) Ellingham diagram showing the standard free energy (ΔG^0) with temperature for the oxidation of Fe, Cr and Ni, b) The phase stabilities for Fe-Cr-Ni steels at 700 ℃ as a function of the oxygen partial pressure and corresponding Cr concentration (thermodynamic calculation using FactSage). Spinel #1: Fe_3O_4 and $FeCr_2O_4$, Spinel #2: Fe_3O_4, $FeCr_2O_4$ and $FeNi_2O_4$, M_2O_3: Cr_2O_3 and Fe_2O_3.

The bulk diffusion coefficient of O is close to that of Cr, but the grain boundary diffusion coefficient of Cr is some orders of magnitude higher than that of O in Cr_2O_3 [114]. These results are in good agreement with the observation that Cr_2O_3 exhibits outer growth at high temperatures. Since Cr_2O_3 formation is favored at all temperatures, the presence of an Fe-oxide in the top of the outer oxide layer in the initial oxidation stage at 700 ℃ needs to be explained.

The duplex-layer oxide is formed because the oxidation procedure is kinetically controlled rather than thermodynamically preferred due to fast metal cation diffusion through the oxide. Once the formation of the protective Cr_2O_3 layer is complete, the oxidation kinetics is controlled by the diffusion through the oxide layer. It is reported that the diffusion coefficients (D) decrease in the sequence $D_{Mn} > D_{Fe} > D_{Ni} > D_{Cr}$ in the Cr_2O_3 layer [115]. The outer spinel layer formed at high temperature is due to the outward diffusion of cations such as Fe, Ni, Mn and Cu from alloy through the Cr_2O_3 layer. Also, an Fe-rich oxide can be formed, which grows at a significantly faster rate than the Cr-rich oxide ($FeO : Cr_2O_3 = 1 : 10^{-5}$) [116, 117]. During the oxidation process, Cr_2O_3 was firstly formed on the surface. At the same time, Fe also reacted with O to form FeO. FeO is thermodynamically more stable than Fe_2O_3 and Fe_3O_4. Thus, the Fe-rich oxide observed in Figure 3.6 b) and c) represents the outer oxide with Cr_2O_3 after initial oxidation. The outward diffusion of Fe which is

blocked by the protective Cr_2O_3 layer prevents further formation of an Fe-containing oxide near the grain boundaries. The protective Cr_2O_3 layer is hardly detected in Tip 3 as seen Figure 3.6 d). Instead, the formation of a non-protective Fe oxide is observed because of the favorable reaction of $FeO(s) + Cr_2O_3(s) = FeCr_2O_4(s)$ [118]. It was found that the transition from a protective Cr_2O_3 oxide into a non-protective Fe-rich oxide is governed by the outward diffusion of Fe through the loose Cr_2O_3. Also, an inner oxide layer with spinel crystal structure gradually developed because the inward diffusion of O is also favorable in Fe-rich oxide.

3.4.2 Early (~12 h) & long term (~500 h) stage oxidation

3.4.2.1 Grain refinement effect

The compositions and morphologies of the oxide layers observed on the Cu added austenite stainless steel are similar to the observation by other researchers for steels of similar compositions [67]. At the first regime of early stage oxidation process (~2 h), the oxidation behavior of all samples can be described by the formation of Cr_2O_3 followed by the surface diffusion of Cr and the associated spreading of Cr_2O_3 from the grain boundaries towards the intra grain regions. According to Figure 3.9, the oxidation kinetics of all samples follows a parabolic law by $(\Delta M/S)^2 = A + K_p t$ [105-107], which indicates that the growth of the oxide layer was controlled by diffusion. Because the grain size of the SG sample is evidently smaller than that of the LG and MG sample, the volume fraction of grain boundary area of the SG sample is larger than that of other samples. As a result, the oxidation rate of the SG sample is faster than that of other samples during the first regime (0~2 h) of early stage oxidation. For the LG and MG samples, two different stages of oxidation behavior can be identified from the slope change in the Figure 3.9 b) which indicates the change in parabolic constant. The oxidation rate during the first regime, oxidation rate is slower than during the second regime (2~12 h) of early stage oxidation. The different parabolic rate constants in the same sample are related to the different types of oxides formation. This observation is in agreement with the kinetics,

surface morphology and XRD data shown in Figure 3.9, 3.10 and 3.12 after 2 h oxidation.

The oxidation behavior of the large-grained sample is determined by both outward diffusion of metal cations (mainly as Fe^{2+} and/or Fe^{3+}) resulting in an outer oxide growth, and inward oxygen anion diffusion (O^{2-}) resulting in an inner oxide growth. Outward diffusion of Fe is closely related to the amount of Cr supplied to the oxide. In case of insufficient Cr supply to the intra grain region, fully dense protective Cr_2O_3 oxide cannot be formed. It results in the continuous diffusion of Fe ion to the surface, which allow the formation of thick Fe-rich oxide layer. Due to the relatively high growth rate of the Fe-rich oxide layer [117], the entire surface of the material is readily covered by an Fe-rich oxide. While the Fe-rich oxide containing of Fe_3O_4 and Fe_2O_3 in outer oxide, Cr-rich $FeCr_2O_4$ spinel oxide forms at the inner oxide layer. An effective diffusion coefficient (D_{eff}) of Cr is obtained by a weighted average of the bulk diffusion coefficient (D_L) and the grain boundary (D_{GB}) as given below [119]

$$D_{eff} = (1 - f)D_L + fD_{GB} \qquad \text{(Equation 3.1)}$$

where f is the volume fraction of grain boundaries. When assuming that the grains are cubic, i.e. $f = \frac{2\delta}{d}$ and $D_{GB} \gg D_L$ and d and δ are the grain size

and width of the grain boundary region, respectively, Equation 3.1 can be simplified [57]

$$D_{eff} = D_L + \frac{2\delta}{d}(D_{GB} + D_L) \approx D_L + \frac{2\delta}{d} D_{GB} \qquad \text{(Equation 3.2)}$$

Hence, D_{eff} increases with decreasing grain size d.

These equations were used to interpret the present data. In this study, the grain size of the samples, when neglecting the ∑3 CSL grain boundaries, was 27 µm, 17 µm and 8 µm for the LG, MG and SG sample, respectively. D_{GB}/D_L is assumed to be 10^5 according to Atkinson [120] who assessed that the ratio of the bulk to the grain boundary diffusion coefficients is in the range of 10^4~10^6, and δ is assumed to be 0.5 nm [121]. The ratio of $D_{eff}^{MG}/D_{eff}^{LG}$ and $D_{eff}^{SG}/D_{eff}^{LG}$ are calculated to be 1.44 and 2.87, respectively. This estimate shows that D_{eff} is higher for the SG sample than for the LG sample. As a consequence of the fast diffusion of Cr along the grain boundaries, a fast growing protective Cr_2O_3 layer can be formed on the entire surface of SG sample. The fast growth of Cr_2O_3 in the SG sample is indeed also revealed by the result of the oxidation kinetics shown in Figure 3.9 and Table 3.3.

3.4.2.2 Critical grain size

As shown in this study, the presence of grain boundaries and hence also the grain size are important factors to be considered for understanding the formation of oxide layers. As the grain size of the Cu added stainless steel is reduced, the spacing among the Cr_2O_3 oxide regions formed on the grain boundaries is consequently also reduced. Hence, less time is required for the sideward growth of the oxide nuclei to finally form a continuous protective Cr_2O_3 layer. On the basis of literature data for the Cr diffusion coefficient in the bulk and along the grain boundaries of a Fe-17~18 wt.% Cr-10~12 wt.% Ni steel [122, 123] in combination with the equations developed by Lobb and Evans [80].

$$j_{GB}/j_L = \frac{2\delta}{d}(D_{GB}/D_L)^{1/2} \qquad \text{(Equation 3.3)}$$

where j_{GB}/j_L is flux ratio, δ is the width of the grain boundary region, d is the grain size, D_{GB} and D_L are the grain boundary and the bulk diffusion coefficient, respectively.

From Figure 3.18 reveals that, according to the grain size decrease, the amount of Cr flux is increased due to the increase of the total grain boundary

density. The flux of Cr ions from the grain boundaries to the surface is considerably high if the distance from grain boundary is less than 5 μm. Thus in the SG sample, due to the grain boundaries Cr diffusion to the surface region is enhanced and sideward spreading of the external Cr_2O_3 layer from the grain boundaries towards the grain interiors occurs, enabling the formation of a continuous protective Cr_2O_3 layer over the whole sample surface. In the case of the Cu added austenitic stainless, even 18 wt.% Cr is not always sufficient to form a protective Cr_2O_3 oxide layer covering the entire surface. Instead, the growth of non-protective Fe-oxide leads to the observed mass gain.

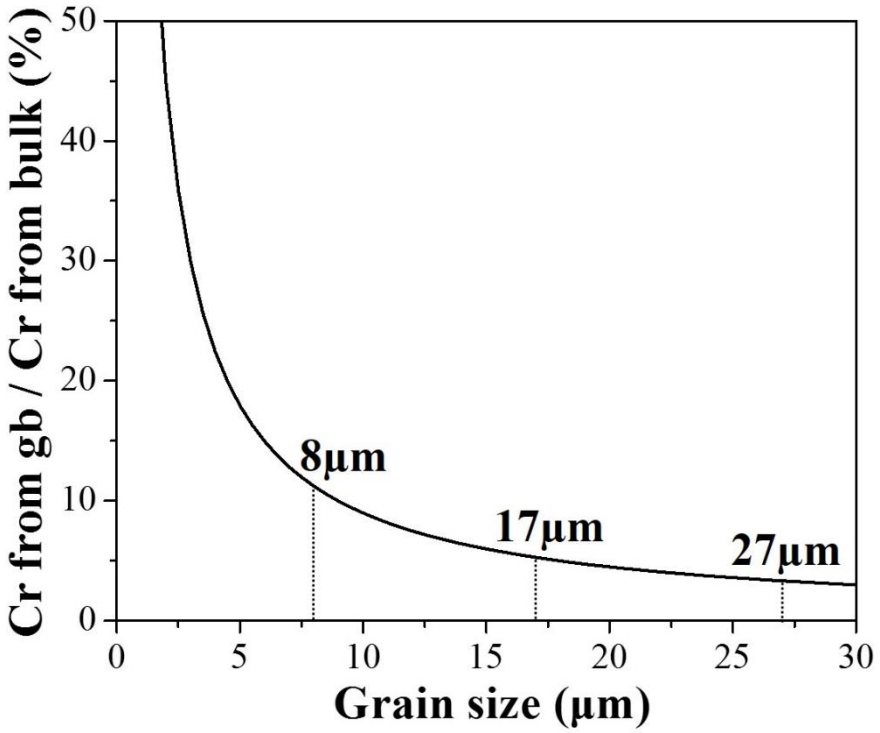

Figure 3.18 Relative increase in the Cr flux via grain boundary diffusion as a function of grain size in Fe-18Cr-10Ni at 700 °C. The grain boundary width (δ) is 0.5 nm.

Figure 3.19 indeed reveals that the Cr wt.% in the outer oxide is strongly influenced by the distance from the grain boundary. The Cr concentration of the outer oxide close to the grain boundaries has around 40 wt.% Cr with the Fe concentration of 30 wt.%. It is important the optimum Cr concentration of range between 23 and 40 wt.% for the maintenance of oxide adhesion and the formation of a protective Cr_2O_3 on Fe-Cr alloys [124] at high temperature. Near the grain boundary, the supply of Cr via both, grain boundary and bulk diffusion is enough to form the protective Cr_2O_3 oxide layer, but, in the intra grain regions apart from grain boundary, the supply of Cr mainly provided by bulk diffusion alone cannot maintain an adequately high Cr concentration to from a protective Cr_2O_3 oxide. In this region, the outer oxide is rendered from a protective Cr-rich oxide to a non-protective Fe-rich oxide such as Fe_3O_4 and Fe_2O_3. This oxide phase transition elucidate the selective oxidation behavior in these Cu added austenitic stainless steels. The formation of Cr_2O_3 is particularly enabled when the distance from a grain boundary is smaller than 4 μm (i.e. for samples with a grain size below 8 μm). The calculated grain size and concentration values of Cr to form the protective Cr_2O_3 layer are in reasonable agreement with the experimental data obtained in this study. Finally, the protective Cr_2O_3 layer at the oxide/matrix interface acts as an effective diffusion barriers against the further transport of oxygen and metal ions.

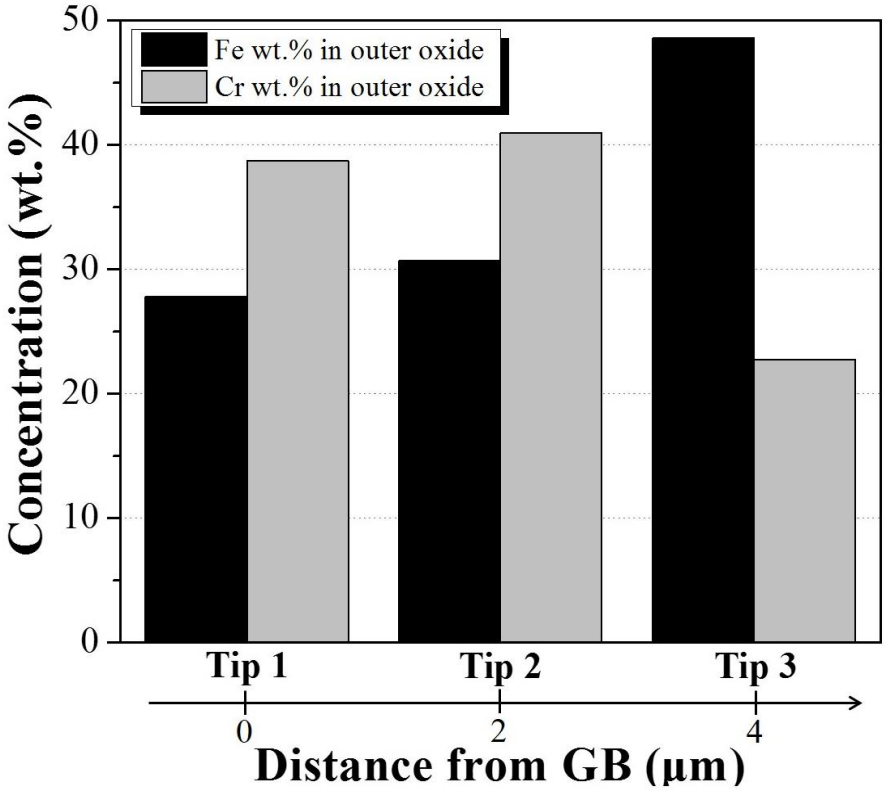

Figure 3.19 Chemical composition (wt.%) of Fe (black bar) and Cr (gray bar) in the entire outer oxide of all tips as measured using APT.

3.5 Summary

High temperature oxidation behavior of Cu added austenitic stainless steel was investigated focused on the grain size effect. A thicker dual layered oxide structure formed on both large grain (27 μm) and medium grain (17 μm) samples with the outer oxide composed of Fe_2O_3, and the inner oxide composed of $FeCr_2O_4$ spinel, but thin Cr_2O_3 oxide single layer was formed in the small grain (8 μm) sample.

Once dense protective Cr-rich oxide is formed, Fe-rich scale cannot grow. In coarse-grained (> 17 μm), Fe-rich oxide only takes place in the grain intra far away about 4 μm from the area around the grain boundaries during the initial stage of oxidation. Therefore, the critical grain size of less than about 8 μm generates dense Cr_2O_3 oxide on the entire surface and cannot be created Fe-rich oxide, the overall oxidation rate can be decreased.

The present study showed that the grain size refinement is an advantageous approach, without increasing the Cr content or adding additional elements, to increase the resistance to high temperature oxidation in humid condition.

Chapter 4

Effect of Alloy element on the structure of oxide layer

: High temperature oxidation behavior of Cu added austenitic stainless steels (Super304H) for the advanced thermal power plant applications

4.1 Introduction

For the last several decades, the formation of oxide layer at high temperatures on heat resistance steel has been extensively studied because it is one of the main sources of the cracks and defects in localized regions [6, 78, 84, 125]. Generally, the oxide layers formed during high temperature oxidation consist of complex and discrete oxides with various microstructures [126, 127]. Conventional analysis techniques such as X-ray diffraction (XRD) and transmission electron microscopy (TEM) are widely used for the complex oxide phase analysis. Recently techniques based on scanning electron microscope (SEM), such as energy dispersive X-ray spectroscopy (EDS), electron probe micro analyzer (EPMA) and electron backscattered diffraction (EBSD) are more frequently used for the oxide phase analysis because they provide phase information with microstructure in a statistically reliable level [93, 126].

Among these techniques, EBSD has the best spatial resolution (several tens of nanometers). EBSD can differentiate phases and provide crystallographic orientation at the same time. However EBSD has limitation for the phase discrimination in case that the candidate phases have the similar crystallographic structures [128]. The accuracy of the phase discrimination of multi-phase materials with similar crystal structure can be enhanced by virtue of chemical information collected by EDS [129-131]. During the last decade EDS signal acquisition speed has extremely enhanced due to the silicon drift detector and the large size EDS detector developments [132]. Now it is comparable with EBSD signal acquisition speed.

The EBSD-EDS real time simultaneous analysis technique has introduced to analyze the complex oxide layers consisting of multi phases with similar crystal structures. In low alloy steels, such as interstitial free steel, the oxide layer consists of three phases; magnetite (Fe_3O_4), hematite (Fe_2O_3), and wüstite (FeO) arranged in order of increasing oxygen content closest to the outer oxide [133-135]. The addition of alloying elements for the better heat resistant properties make the oxidation of steels more complicated and the oxide phases are strongly dependent on the steel composition [136]. In this study, oxide scale of Cu added austenitic stainless steel was investigated. Distribution of hematite (Fe_2O_3), magnetite (Fe_3O_4), chromite ($FeCr_2O_4$), chromia (Cr_2O_3) and Cu containing spinel (Fe_2CuO_4) in internal and external

oxides has discriminated by EBSD-EDS simultaneous analysis technique. Effect of Cu addition on the oxide formation was discussed based on the observed results.

4.2 Experimental

4.2.1 Sample information and preparation

The materials used in this study was a 3wt% Cu added austenitic stainless steels with 18wt% Cr, 8wt% Ni, 0.1wt% C, and 0.38%Nb. Oxidation test with 10 mm x 7 mm x 1.2 mm sample dimension carried out 500 h oxidation at 700 ℃ in air with 20% water vapor. After oxidation, sample was coated using epoxy resin after Au deposition on the oxide surface in order to protect the brittle oxide scale. For the cross-sectional analyses, edges of sample was grinded on silicon carbide paper finishing with 2000 grit and ion milled by cross sectional ion miller (E-3500, Hitachi, Japan).

4.2.2 EBSD-EDS simultaneous analysis

The EBSD-EDS simultaneous analysis was performed using the EBSD (*e*-Flash^{HR}, Bruker, Germany) and EDS (XFlash, Bruker, Germany) mounted on field emission gun SEM (S-4300SE, Hitachi, Japan). All EBSD-EDS maps were processed using the Esprit 1.9.4 software. All the dataset and figures in this chapter present in the original state without data cleaning for the clear understanding about the real microstructures. An EBSD-EDS map of 132,000 points covering an area of 81.92 μm x 30.17 μm was acquired in 20 kV acceleration voltage and 4 nA probe current condition. A fine step size (0.14 μm) was used in order to obtain the detailed information from the fine grains of the oxide layer. Each EBSD-EDS data was acquired for 51 ms integration of 3 frames averaging to get high quality EBSD patterns and enough EDS counts (~3000 counts).

4.3 Results and Discussion

4.3.1 Oxide phase of Cu added austenitic stainless steels

Cu added austenitic stainless steels oxidized at 700 C° are composed of seven different phases: Austenite matrix (γ-Fe), Ferrite (α-Fe), Chromia (Cr_2O_3), Hematite (Fe_2O_3), Magnetite (Fe_3O_4), Chromite ($FeCr_2O_4$) [137] and Cu containing spinel (Fe_2CuO_4). Figure 4.1 shows the crystal structures and the simulated Kikuchi patterns of these various phases. They have different space groups; γ-Fe: $Fm\bar{3}m$, α-Fe: $Im\bar{3}m$, Cr_2O_3: $R\bar{3}c$, Fe_2O_3: $R\bar{3}c$, Fe_3O_4: $Fd\bar{3}m$, $FeCr_2O_4$: $Fd\bar{3}m$ and Fe_2CuO_4: $Fd\bar{3}m$. Three phases of spinel structure and two phase of rhombohedral structure show same EBSD patterns respectively. The EBSD pattern from austenite phase also shows very similar pattern especially for the diffraction bands with high intensity because the iron atoms of austenite matrix and spinel oxide have the same symmetry. The similarities between the EBSD patterns raise the problems in identification of oxide phases. Previous study showed the analysis of oxide can be possible with only EBSD but they analyzed oxidation of ferritic steels [126, 138, 139].

Combined analysis of EBSD and EDS is helpful for accurate phase identification [140, 141]. But it is hard to apply for the complex oxides of multi elements alloyed steels because several steps of subset creations are required. In the simultaneous EBSD-EDS analysis, phase is selected among the candidate

phases based on the fast quantification with EDS data and the phase is confirmed by EBSD analysis. So there is no need for the repeating subset creation steps. For the complicate oxide analysis, real time simultaneous EBSD-EDS analysis is the most efficient solution.

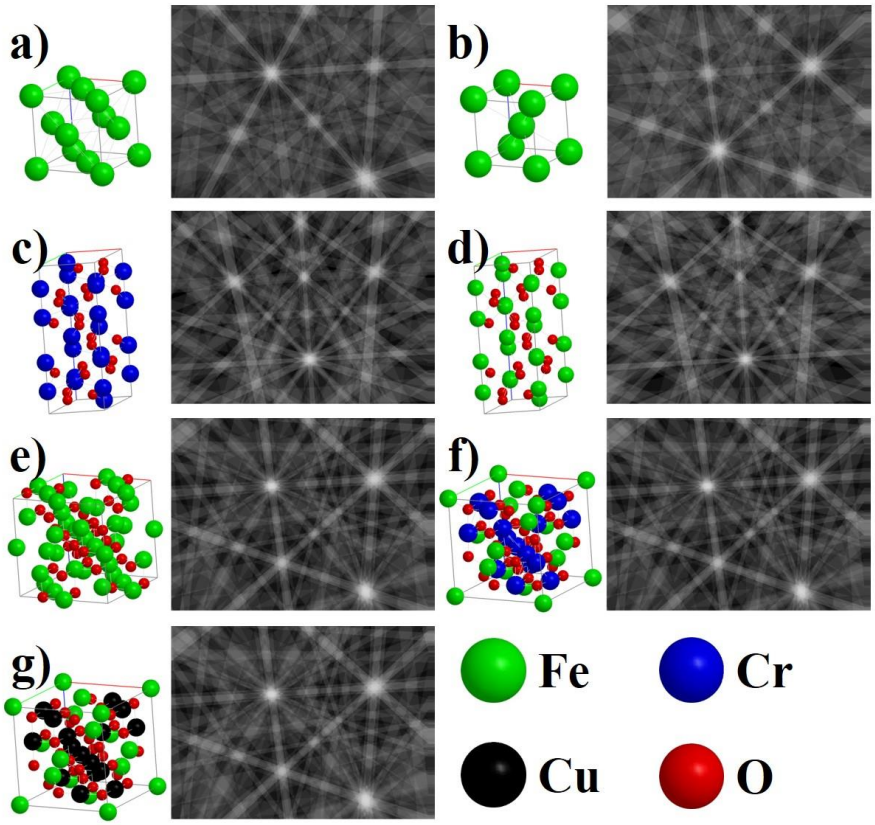

Figure 4.1 The unit cell and the corresponding spherical Kikuchi pattern (kinematic simulation) obtained from each phase; a) Austenite (γ-Fe), b) Ferrite (α-Fe), c) Chromium oxide (Cr_2O_3), d) Hematite (Fe_2O_3), e) Magnetite (Fe_3O_4), f) Chromite ($FeCr_2O_4$) and g) Cuprospinel (Fe_2CuO_4) in [Phi1,Phi,Phi2] = (30;-10;0).

4.3.2 Oxide composition analysis using EDS

Figure 4.2 presents the EDS maps obtained from the cross-section of the oxide scale oxidized at 700 ℃ for 500 h. The composition maps include oxygen, iron, chromium, nickel, manganese, and Cu to identify the various oxide phases. The oxygen map indicates that the oxide layer is formed at the upper portion of the specimen. The other components maps (e.g., iron and chromium) indicate that the oxide layer consists of two distinct layers. According to our previous study, these two layers are composed of an iron-rich external oxide and a chromium-rich internal oxide [84]. The manganese distribution is similar to the distribution of chromium. Nickel is enriched in the internal oxide and at the interface between the external and internal oxide. The Cu map revealed that Cu is enriched not only at the scale/metal interface but also at the top surface of the external oxide. Rosser et al. [142] also identified Cu enrichment at the scale/metal interface in steel with a similar composition; however, Cu enrichment at the top surface of the external oxide is consistent with the previous report by Kondo on the oxidation of steel containing 0.096 wt.% Cu at 1200 ℃ [143, 144].

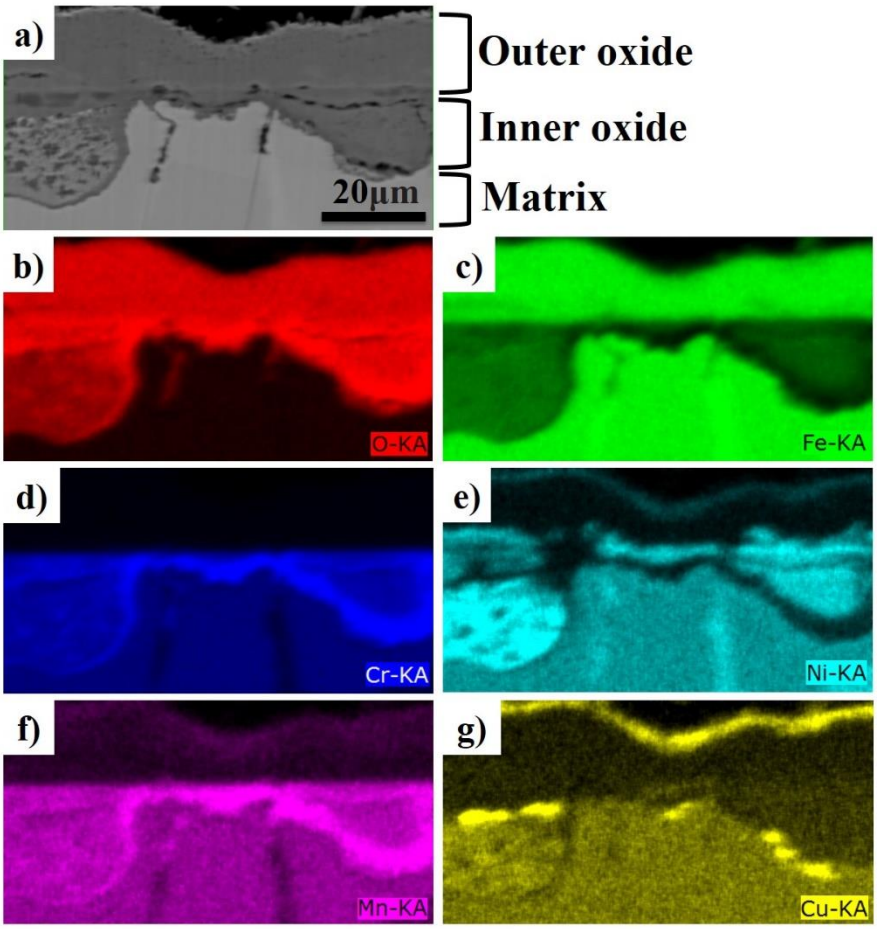

Figure 4.2 Cross sectional energy dispersive spectroscopy (EDS) maps of the oxide layers after 500 h oxidation at 700 ℃ in air with 20% water vapor; a) back scattering electron (BSE) image, b) oxygen map, c) iron map, d) chromium map, e) nickel map, f) manganese and g) cupper map, respectively.

4.3.3 Oxide phase and orientation analysis using EBSD-EDS simultaneous

Figure 4.3 a) presents the pattern quality map obtained from the region shown in Figure 4.2. The microstructure of the steel and iron oxide layers are identified in the pattern quality maps. These maps indicate that several μm-sized equiaxed polygonal oxides formed in the external oxide layer, whereas the oxides grown internally were single grained with the same orientation from the surface (Figure 4.3 b)). Figure 4.3 e) presents the phase map acquired from the EBSD data. As discussed in the previous section, the austenite phase cannot be differentiated from spinel oxide by EBSD analysis alone. Therefore, the oxide and austenite present in the lower part of the map are indexed as a mixture of Cu-containing spinel oxide and austenite. Figure 4.3 f) presents the phase map acquired by real time simultaneous EBSD-EDS analysis. Seven phases can be successfully distinguished in the cross-section. The internal oxide consists mainly of chromite spinel oxide. A small amount of chromium oxide is observed at the interface between the internal oxide and Austenite matrix. Hematite with a rhombohedral structure mainly formed in the external oxide. At the interface between the internal and external oxides, a small amount of magnetite oxides was also observed. Magnetite and Cu-containing spinel oxides were also observed at the top surface of the external oxide. This

observation is confirmed by indexing the EBSD patterns acquired from the top surface area in the spot analysis mode.

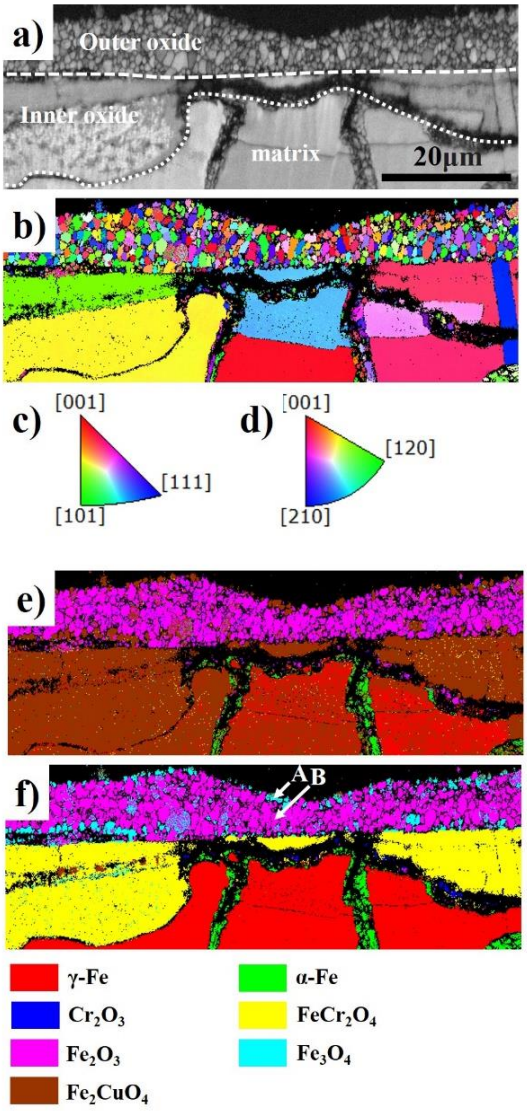

Figure 4.3 a) Pattern Quality map, b) Orientation map, acquired from the same area as Figure 4.2, c) Color key of cubic symmetry materials, d) Color key of rhombohedral symmetry materials, e) Phase map without EDS information and f) Phase map acquired by EBSD-EDS simultaneous analysis.

4.3.4 The formation of Fe_3O_4 and Cu containing spinel oxide at the top surface

In low-alloy steels, such as interstitial-free steels, the oxide layer consists of three phases (wüstite (FeO), magnetite (Fe_3O_4), and hematite (Fe_2O_3)), arranged in proximity to the outer oxide surface according to increasing oxygen partial pressure [2, 134, 135]. It is confirmed by the indexing of the EBSD patterns acquired from the top surface area in spot analysis mode as shown in Figure 4.4. It is reasonable that iron oxide transforms from magnetite to hematite according to the increase in oxygen partial pressure considering the oxygen to iron ratio of both oxides. The transition back to magnetite at the top surface is not immediately apparent, but the Cu distribution presented in Figure 4.2 g) provides an explanation. According to Jacob et al. [145] who constructed phase diagrams of the Fe-Cu-O system in a temperature range between 600 and 1600 ℃, the addition of Cu to hematite induces the formation of a solid solution of magnetite and Cu-containing spinel oxides as shown in Figure 4.5, especially under an oxygen pressure of 1 atm.

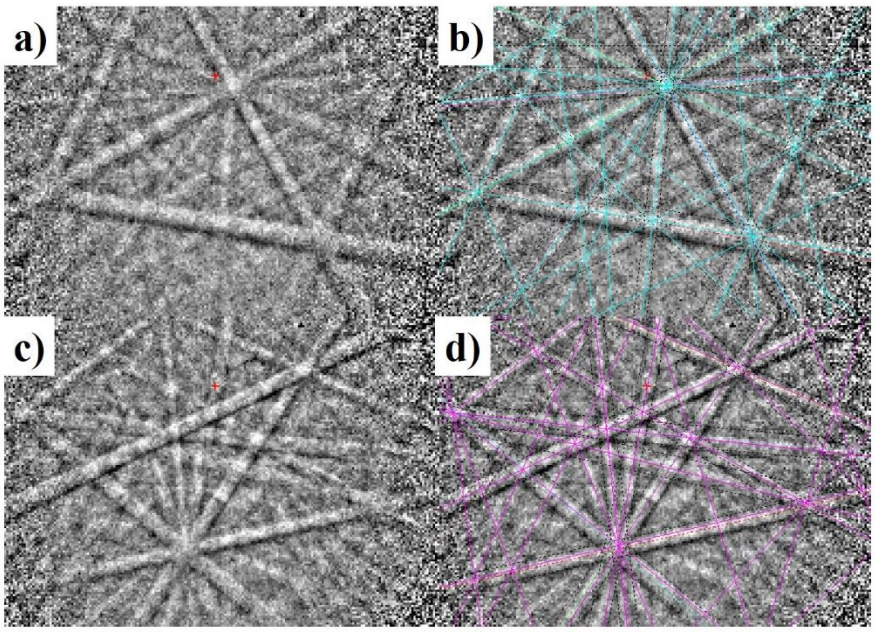

Figure 4.4 a) Original EBSD pattern from site A of Figure 4.3 f), b) EBSD pattern overlay of indexed bands as Fe_3O_4 on a), c) Original EBSD pattern from site B of Figure 4.3 f), and d) EBSD pattern overlay of indexed bands as Fe_2O_3.

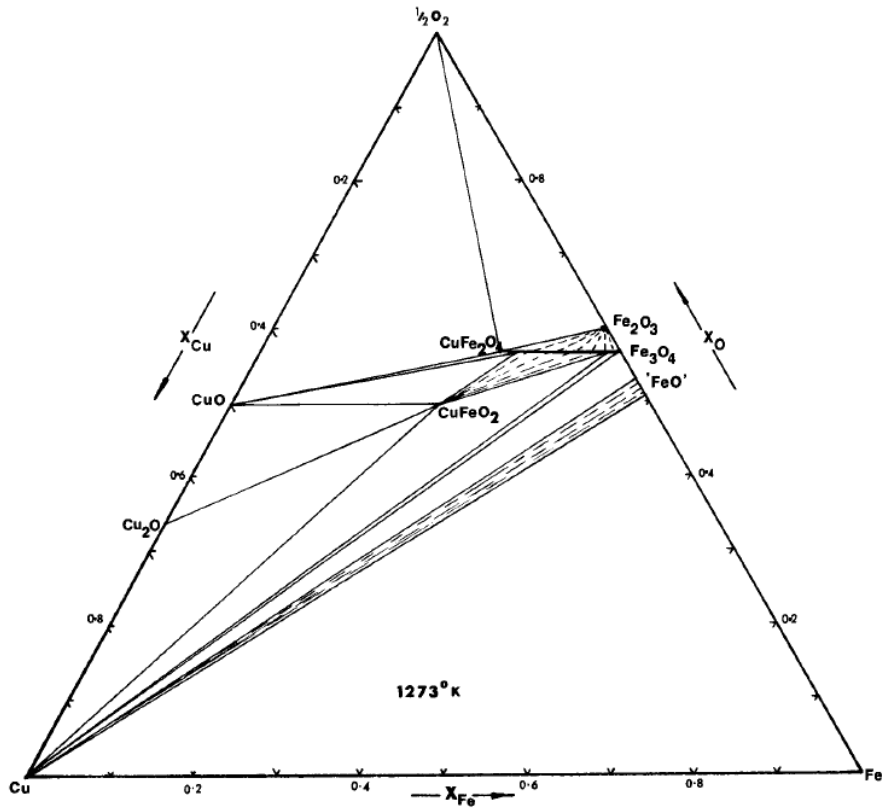

Figure 4.5 Gibbs triangle representation of phase relation in the system Cu-Fe-O at 1000 ℃

Figure 4.6 a) shows the cropped phase map of Figure 4.4 f) at the outer surface area. Figure 4.6 b) shows the EDS spectrum from the site A in Figure 4.6 a) in spot mode. The Cu content of this point increased to 15 wt.%. The formation of magnetite and Cu-containing spinel oxides at the top surface of the external oxide results from Cu enrichment during the oxidation heat treatment. Figure 4.6 c) shows the cropped phase map of Figure 4.4 f) at the internal oxide/matrix interface. Figure 4.6 d) shows the EDS spectrum from the site B in Figure 4.6 c) in spot mode. The chromium content at this point increased to 60 wt.%. Chromium is enriched at the internal oxide/matrix interface, especially at the area near the grain boundary of the austenite matrix, which leads to chromium oxide formation at the interface.

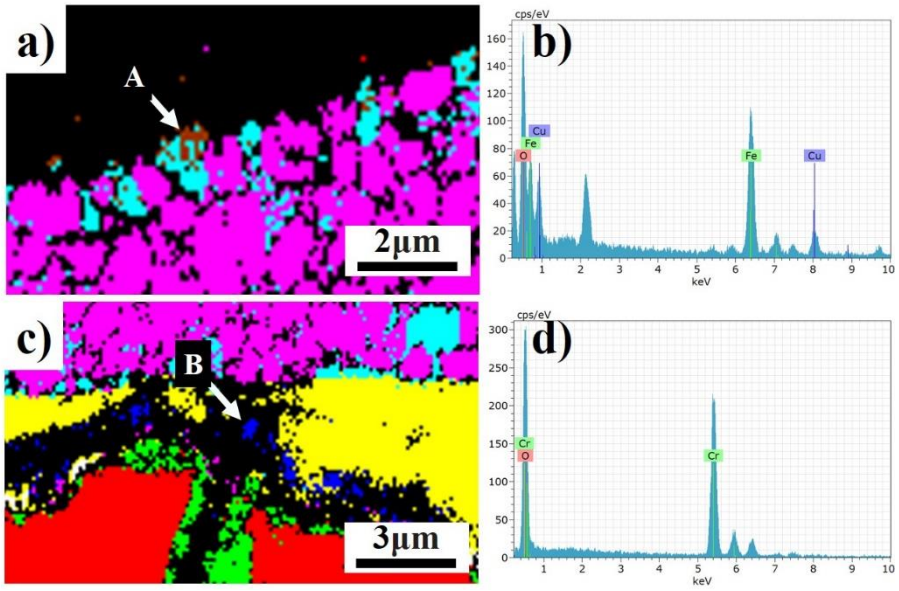

Figure 4.6 a) Cropped phase map taken from the Figure 4.3 f) of the original manuscript at the outer surface area, b) EDS spot mode data of the Cu containing spinel oxide from site A, c) Cropped phase map taken from the Figure 4.3 f) of the original manuscript at the internal oxide/ matrix interface, d) EDS spot mode data of the Cr_2O_3 from site B

4.4 Summary

Oxide layers on Cu add austenitic stainless steel were investigated by simultaneous EBSD-EDS analysis. The internal oxide consists of chromite with small amounts of chromium oxide. The external oxide has a multi-layered structure with a magnetite-Cu-containing spinel oxide solid solution, hematite, and magnetite. The magnetite-Cu-containing spinel oxide solid solution at the top surface of the external oxide results from Cu enrichment during the oxidation heat treatment.

Chapter 5

Effect of Water Vapor

on the Abnormal BCC Phase Transformations

: High temperature oxidation behavior of Cu added austenitic stainless steels (Super304H) for the advanced thermal power plant applications

5.1 Introduction

When the operating condition is higher than 620 ℃, ferrite heat resistant steels are limited to use as superheater and reheater materials in the ultra-supercritical (USC) power plants because of the properties of high temperature creep strength and oxidation resistance [146]. For this reason high temperature materials with improved creep resistant strength and corrosion/oxidation resistance properties over 600 ℃ are required, such as advanced austenitic heat resistant stainless steel [48, 49]. The 304 austenitic stainless steel is generally accepted as high temperature stability, high creep strength and high oxidation resistance and can be widely used in critical components of power plant [147].

In order to further improve high temperature creep strength, Cu has been added to gain distinct Cu-rich phase precipitation strengthening effect, such as Super304H steel [55]. The Cu-rich phase is the most dispersed phase and contributes the most important strengthening effect among all precipitated phases ($M_{23}C_6$, MX and Cu-rich phase) [52]. Also, in order to improve oxidation resistance of this steel at high temperature, extensive studies have been conducted on grain refinement [82, 84] and surface treatment [60, 148] to reduce oxidation rates. However, little attention has been given to the effect of phase transformation during oxidation of Cu added austenitic stainless steel. The microstructure of Cu added austenitic stainless steel consist of γ-austenite phase. Austenite has a face centered cubic (FCC) crystal structure, and is the predominant phase in this alloy. We found the new phase of BCC structure along the grain boundary during the oxidation [101, 149]. Structural (or Phase) transformations at grain boundaries are of fundamental interest and can have a significant impact on microstructure, mechanical behavior, and transport properties of heat resistance steel.

In the paper, direct observations of the ferrite and austenite phase and their transformation dynamics of the Cu added austenitic stainless steel on the high temperature with humid condition was studied, and the SEM, XRD, TEM and 3DAPT techniques were used to analyze the phase transformation from FCC to BCC in combination with Thermal-calc calculation. Using transmission

electron microscopy (TEM), the present study gives detailed information, such as crystallographic structure, morphology and orientation relationship on each grains. Another important goal is to reveal the chemical composition of each grain using atom probe tomography (APT).

5.2 Experimental

5.2.1 Alloy synthesis

The as-received alloy used in this study was basically close to that of well-known Cu added austenitic stainless steel. Its chemical composition as determined by inductively coupled plasma mass spectroscopy (ICP-MS) is as follows (in at.%): 19.11% Cr, 8.67% Ni, 0.78% Mn, 2.56% Cu, 0.39% Si, 0.51 % C, 0.002% B, 0.23% Nb and 0.64% N, with the balance Fe. Details of the thermo-mechanical processing and the sample preparation have been published the previous paper [84, 149]. For phase transformation studies, rectangular samples of 10mm in length, 7mm in width and 2mm in thickness were cut from the center of the bulk material. Subsequently, the samples were electro-chemically polished using an electropolisher (Lectropol-5, Struers, Denmark) in a solution of 59 vol.% of methanol, 35 vol.% of methyl propanol and 6 vol.% of perchloric acid at 18 V and for 30 s at -30 ℃, so as to avoid the deformation-induced phase transformation at surface contact area during mechanical polishing. Then the samples were ultrasonically cleaned in an acetone-ethanol mixture and finally dried.

Among the samples, one sample was as-received sample which is referred to as “Non-Oxidation Sample (NOS)” in the following. Others sample were oxidized at 700 ℃ in air with 20% water vapor for 30 min, 100 h and 500

h which is referred to as “Oxidation Sample (OS)”. High-temperature oxidation experiments have been published the previous paper [149].

Thermodynamic calculations were carried out to give an indication of the phases likely to be present at equilibrium in this study using Thermo-Calc in conjunction with the TCFE2000 database.

5.2.2 X-ray diffraction, Scanning electron microscopy and electron probe microanalysis

The simply phase analysis of the matrix and oxide layers in Non-Oxidation and Oxidation sample was carried out by X-ray diffraction (XRD, Bruker D8 advance diffractometer, Cu k_α radiation: $\lambda = 0.154$ nm, Germany). The XRD data was obtained by point scanning in the 2θ angular range from 15° to 80° with a step size of 0.02° (2θ) and a scan time of 2s per step at room temperature. Diffraction patterns were indexed by using the JCPDS database.

For the cross-sectional analyses of large region after 500 h oxidation, sample was coated using epoxy resin after Au plating on the oxide surface in order to protect the brittle oxide scale on the substrates. Edges of sample was polished on silica carbide paper finishing with 2000 grit and milled by cross-sectional ion miller (E-3500, Hitachi, Japan). The cross-sectional morphology and phase analysis were performed using the EBSD (Bruker, *e*-Flash^{HR}, Germany) mounted on SEM (Hitachi, S-4300SE, Japan). Additionally, the elemental distributions were determined using electron probe microanalysis (EPMA, JXA-8500F, JEOL, Japan).

5.2.3 Transmission electron microscopy and Atom probe tomography

The TEM sample was cut from oxidation sample using a dual-beam focused ion beam (FIB) device (Helios Nanolab 600i, FEI, USA) following the lift-out procedure. The TEM lamella was attached to a Cu grid and thinned by FIB milling to a thickness of ~50 nm. For oxidation sample, transmission electron microscopy (TEM, Tecnai F20, FEI, USA) was used to examine detailed crystal structure of different phases in the matrix at an acceleration voltage of 200keV.

Atomic scale composition analysis of the matrix before and after oxidation was conducted using atom probe tomography (APT). The needle-shaped APT specimens from grain boundary using same FIB device following the lift-out procedure [90, 91]. Selected area sample preparation processing shows in Figure 5.1. Surface of sample was coated using Pt (on the Non-oxidation sample) or Ni (on the Oxidation sample) plating on the oxide surface in order to protect the brittle oxide scale on the substrates. Atom-probe analyses were performed using local electrode atom-probe system (LEAP 3000X HR, Imago Scientific Instrument, USA). APT analysis was performed in laser mode applying laser pulses of 532 nm wavelength at ~60 K (a specimen temperature of about 68.4 K). The pulse frequency and pulse energy employed were 200 kHz and 0.6 nJ, respectively. Data analysis including reconstruction of three-

dimensional (3D) atom maps were carried out using the IVAS 3.6.6 software of Imago Scientific Instrument.

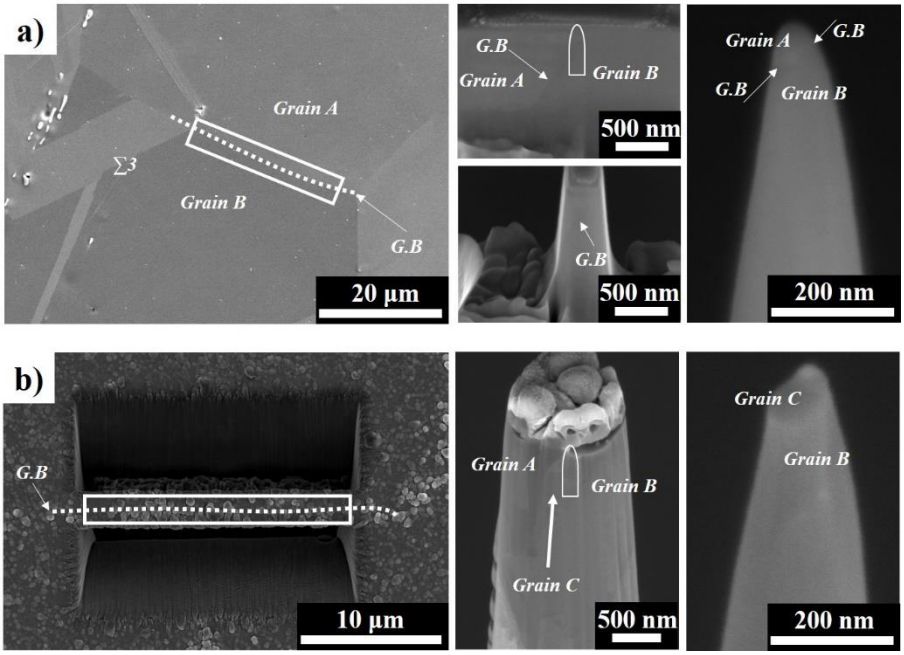

Figure 5.1 Site-specific APT sample preparation processing of selected region. a) Selected region of interest (white box) containing a random grain boundary before oxidation sample, b) Selected region of interest (white box) containing a random grain boundary after 30 min of oxidation at 700 ℃ in air with 20% water vapor and 1st/2nd mill cut for APT samples preparation.

5.3 Results and Discussion

5.3.1 Phase identification of matrix and oxide using XRD

Results of matrix and oxide phase analysis by X-ray diffraction are shows in Figure 5.2. X-ray diffraction analysis of Non-oxidation sample confirmed the presence of γ-Fe (austenitic stainless steel AISI 304, JCPDS 33-0397) in Cu added austenitic stainless steel. Another papers [62, 150] note initially presence of the α´-martensite and the austenite phase. The martensite presence is related to a mechanical polishing effect by plastic deformation. However, the X-ray diffraction results of our experiments detected a strong peak of matrix structure of only austenite. Also precipitates had not yet formed in Non-oxidation sample because other peak characteristic for $M_{23}C_6$ are absent.

However, as a result of the 30 min oxidation at 700 ℃ in air with 20% water vapor, X-ray diffraction shows the presence of α-Fe (JCPDS 85-1410) with the γ-Fe. At the same time, the growth of Cr_2O_3 (JCPDS 38-1479) is also observed in Oxidation sample.

The oxidation leads to the ferrite formation on the alloy surface. Due to the thin thickness of oxide, austenite and ferrite peaks from the matrix were present. As it was observed by other authors [148], the BCC phase was also detected during oxidation.

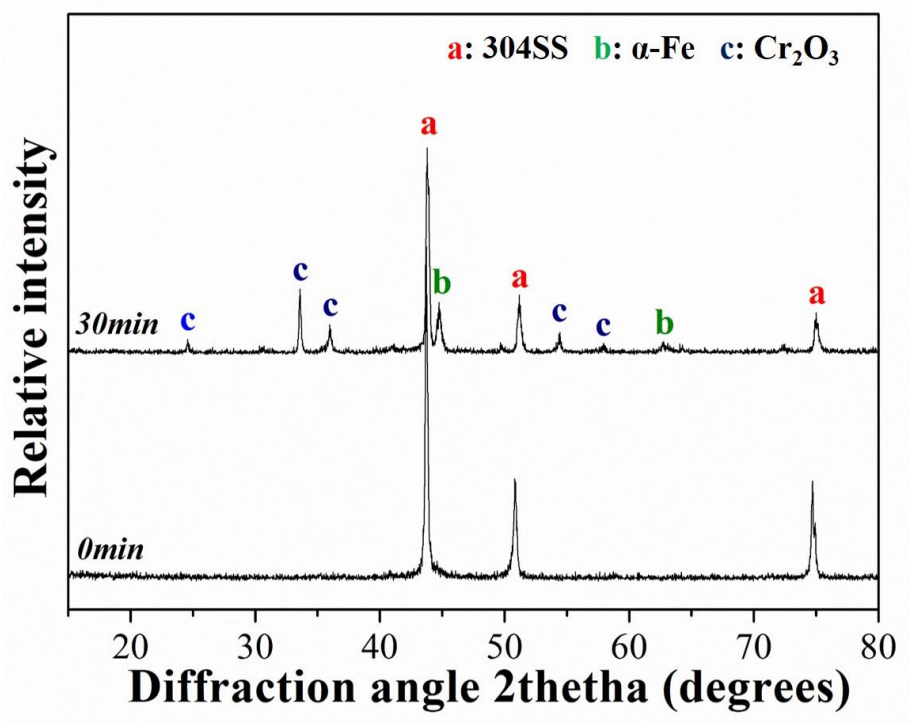

Figure 5.2 XRD analysis of oxide performed on sample during 30min oxidation, at 700 ℃, in 20% humidity.

5.3.2 Cross-sectional morphology analysis using SEM

Figure 5.3 compares the microstructures of Non-oxidation and Oxidation sample of Cu added austenitic stainless steel close to the grain boundary. The schematic images are sketched in right side of SEM images, respectively.

Figure 5.3 a) shows the cross-sectional SEM image of the matrix in Non-oxidation sample. Channeling contrast in scanning electron microscopy secondary electron images can be used to reveal the location of the grain boundary. It shows that two grains and the grain boundary are observed. The grain boundary was confirmed to be a random boundary with 54° misorientation (EBSD data, not presented here). A Pt layer is deposited to protect the surface above the grain boundary in the area chosen of Figure 5.1 a) for sample preparation.

Figure 5.3 b) shows the cross-sectional SEM image of the matrix and oxide layer in oxidation sample after 30 min, at 700 ℃, in 20% humidity. Obviously, it shows that new grain "C" is formed along the prior austenite grain boundary with thin oxide layer. Moreover, the outer diffusion of metal cation can generate voids at oxide/matrix interface [56]. The estimated new grain "C" is consistent with simultaneous EDS-EBSD analysis from previous works [101], confirming that the phase is BCC structure.

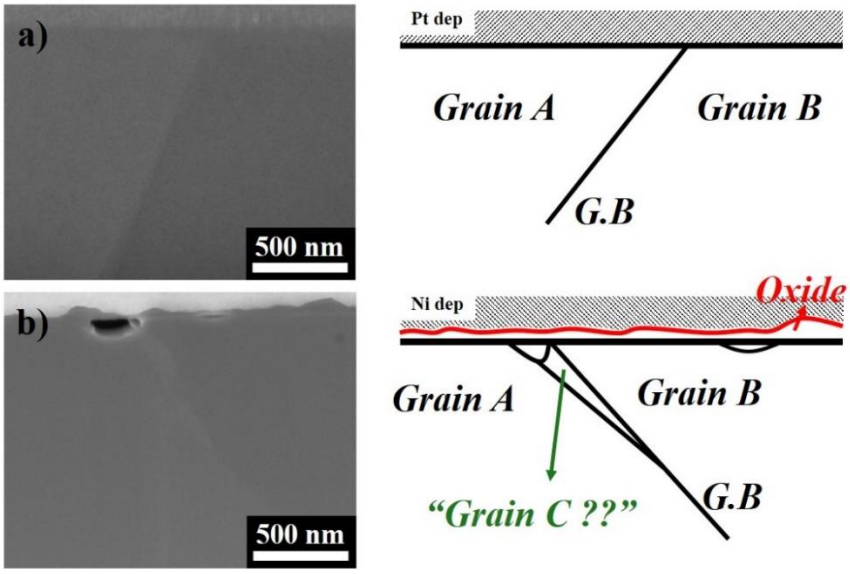

Figure 5.3 Secondary electron (SE) images of cross sectional view contained grain boundary. a) Non-oxidation sample, b) Oxidation sample.

5.3.3 Structure analysis using TEM

As shown Figure 5.3 b), the new grain “C” is generated along the grain boundary between original grains nearby Oxidation sample surface. In gaining a better understanding of the phase transformation processes, detailed phase structure analysis of this new grain “C” was performed by TEM.

Figure 5.4 shows the typical TEM image of a cross-section of Cu added austenitic stainless steel after oxidation, a corresponding selected-area diffraction pattern (SAED) and TEM-EDS mapping. Figure 5.4 a) is a bright-field image (BFI) and clearly shows the surface oxide layer and three different grain (A, B, C). Figure 5.4 b), c) and d) show the SAED pattern of each grain of the Figure 5.4 a). The results of SAED showed that the grain “A” and “B” has the FCC crystallographic structure, but grain “C” has the BCC crystallographic structure, respectively. It is considered that the crystallographic relationship between γ-matrix (FCC) and α-new grain (BCC) follows the Bain and the Nishiyama-Wassermann relationship [151, 152].

Therefore, BCC structure has formed at the previous austenite grain boundary during the oxidation. In addition to Figure 5.4 e) and f) show the TEM-EDS maps of Cr (green) and Ni (cyan) to confirm composition of FCC and BCC grain, whose compositions were slightly different and distinguished. It shows that the FCC grains contained high Cr and low Ni contents. On the

contrary, BCC grain contained low Cr and high Ni contents. This mean that the ferrite region is richer in Ni and depleted in Cr, compared to austenite region.

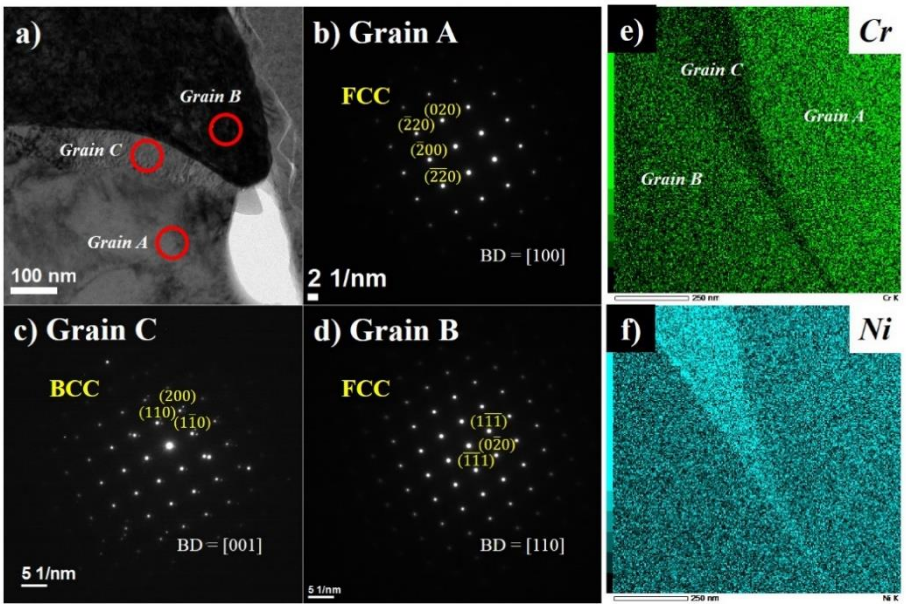

Figure 5.4 TEM analysis of Oxidation sample at 700 ℃, 20% humid condition, a) Bright field image of Figure 5.3 b), b), c) and d) SADP of each grain, e) and f) EDS mapping of Cr and Ni in matrix.

5.3.4 Chemical composition analysis using APT

Figure 5.5 gives the three dimensional atom distribution maps and 1D compositional profile at grain and grain boundary region in Cu added austenitic stainless steel before and after oxidation. The two tips were taken from exactly the same grain in Figure 5.3.

Grain boundary segregation of many elements in Non-oxidation sample shows as in Figure 5.5 a). The atom maps have been oriented so that the views are parallel to the grain boundary plans. Enrichment of C, B and Nb atoms are evident at grain boundary from the atoms map. The carbide still does not nucleate at grain boundary because of the C atoms distributing at the grain boundary plan randomly.

Composition profiles through FCC-FCC grain interfaces can be seen from the 1D depth profiles across the grain boundary in C atom map. It shows that similar compositions were observed in the each FCC grain, but enrichment of Cr, Si, C, Nb in a layer about 5 nm in width at grain boundary. These segregation feature of 304 austenitic stainless steel was also observed in other papers [153].

Composition changes of many elements from the different phase in Oxidation sample show as in Figure 5.5 b). As shown in (Figure. 5.4 e) and f)) (or in accordance with TEM-EDS results result shown in Figure 5.4.), Cr and

Ni-rich and depleted regions are clearly distinguishable. As crystallographic information was available from Figure 5.4, depletion of Cr and enrichment of Ni is evident from the individual atom maps in BCC grain. The atom maps also showed that Cu atom can quickly concentrate in only FCC matrix to form the fine nano-size Cu-rich phase [51].

Composition profiles through BCC-FCC grain interfaces can be seen from the 1D depth profiles across the grain boundary in Cr atom map. It clearly shows that the Cr, Cu, Mn, Si, C and N atoms deplete at the BCC grain in Oxidation sample. It is also clear from APT data in Figure 5.5 b) that there was no significant segregation of elements to the ferrite/austenite interface.

In order to precisely analyze the composition of elements in each grain, more detailed mass spectrum were separately carried out on these specific regions of interest (ROI). They are designated as Region #1, Region #2, Region #3 and Region #4 in Figure 5.5, respectively. Three selected ROIs (Region #1, #2 and #4) in the FCC grain and one selected ROI (Region #3) in the BCC grain are analyzed. The average composition in each ROI characterized by APT is shown in Table 5.1. Similar compositions were observed in boxes of FCC grain. But, the measured composition is a little different from the ICPMS composition. This is because the APT estimate was a simple counting of atoms within the selected volume of the matrix of ferrite and austenite. The composition of N is different the data, because N atoms may be exhausted by NbN precipitated in

the matrix. In case of BCC grain, it contains mainly Fe (76.43 at.%), Ni (13.62 at.%) and small amounts of C (0.06 at.%), N (0.013 at.%).

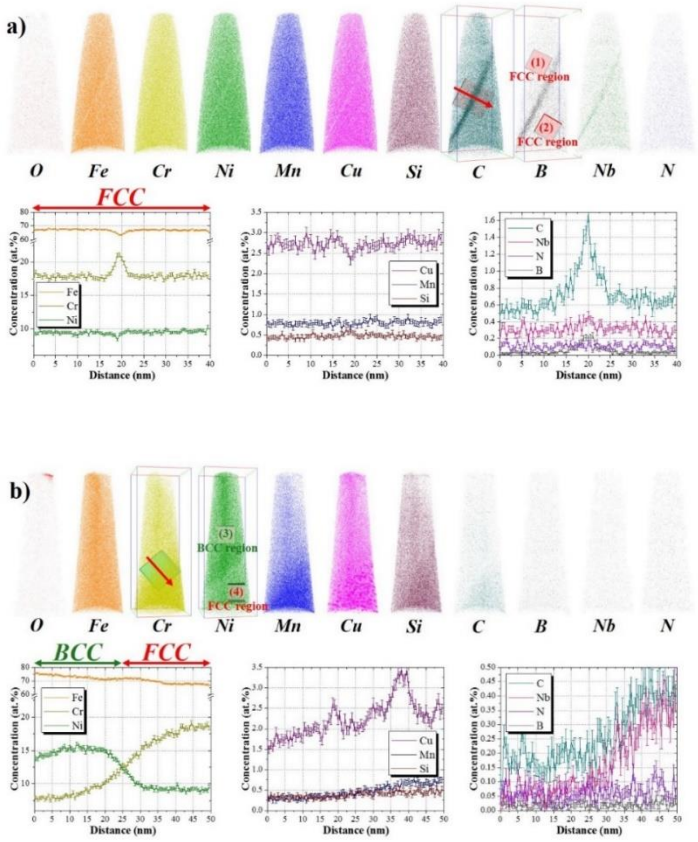

Figure 5.5 3D atom elemental map displaying the overall distribution; a) Non-oxidation sample (60x60x200 nm^3, 0.0169 at.% O), b) Oxidation sample (70x70x200 nm^3, 0.0212 at.% O). And elemental concentration 1D profiles (fixed bin width of 0.5 nm) along the ROI taken across the grain boundary. 1D profiles of all boxes determined with a cube of dimension 15 nm. The red arrows mark the directions along which the concentration profiles are drawn. Error bars represent σ statistical error due to the limited number of atoms in a sample volume.

Table 5.1 The average compositions in each region (all boxes determined with a 25x25x25 nm^3) analyzed by APT (wt.%) from Figure 5.5. The error bars represent 2σ standard deviation.

	Fe	***Cr***	***Ni***	***Mn***	***Cu***
(1) FCC region	67.78 ±0.147	18.10 ±0.064	9.12 ±0.043	0.76 ±0.012	2.55 ±0.022
(2) FCC region	67.39 ±0.200	17.93 ±0.087	9.59 ±0.061	0.78 ±0.017	2.73 ±0.032
(3) BCC region	76.43 ±0.146	7.52 ±0.036	13.62 ±0.049	0.23 ±0.006	1.60 ±0.016
(4) FCC region	67.19 ±0.140	18.59 ±0.062	9.08 ±0.042	0.74 ±0.011	2.86 ±0.023

	Si	***C***	***B***	***Nb***	***N***
(1) FCC region	0.44 ±0.010	0.60 ±0.011	0.002 ±0.0007	0.30 ±0.008	0.065 ±0.004
(2) FCC region	0.43 ±0.012	0.50 ±0.013	0	0.28 ±0.010	0.053 ±0.004
(3) BCC region	0.26 ±0.006	0.06 ±0.003	0.001 ±0.0005	0.03 ±0.002	0.013 ±0.001
(4) FCC region	0.46 ±0.009	0.39 ±0.008	0	0.39 ±0.008	0.057 ±0.003

5.4 Summary

We have studied the phase transformation behavior of the austenite (γ) to ferrite (α) in Cu added austenite stainless steel after oxidation at 700 ℃ in air with 20% water vapor. The results of SEM, XRD and TEM reveal that α-BCC phase formed along the prior γ-FCC grain boundary after oxidation. According to the APT result, Fe and Ni are strongly concentrated and Cr is depleted in α-BCC phase. The intensity of hydrogen-caused γ→α transformation in austenitic steels.

Chapter 6

Effect of Substrate Grain Orientation on the Oxidation Resistance and Electrical Conductivity

: High temperature oxidation behavior of 22 wt.% Cr ferritic stainless steels (Crofer 22 APU) for the solid oxide fuel cells applications

6.1 Introduction

Ferritic stainless steels have been preferred as a material for interconnects in solid oxide fuel cells (SOFC) because of their high electrical and thermal conductivity, good mechanical properties, good formability, affordable price and similar thermal expansion coefficient (TEC) to the other cell components. The SOFCs operate in the temperature to an intermediate range of 650~800 ℃ [154, 155]. At these temperatures, the major concerns are the oxidation resistance and the electrical conductivity in an outer layer of the oxide scales. In order to increase the oxidation resistance and the electrical conductivity, typically either chemical composition such as Mn, Ti, Al [155-157] and Si alloy elements is controlled or interconnects is given a surface

treatment [158, 159]. Specially, Mn has been used as an alloy element in ferritic stainless steel to increase the electric conductivity of the scale [160]. Oxidation resistance is also improved by coating such as $La_{0.8}Sr_{0.2}CrO_3$ (LSC), $La_{0.8}Sr_{0.2}FeO_3$ (LSF) [159], $MnCo_2O_4$ spinel layer [161] and ion implantation [158].

In ferritic stainless steel with more than 20 wt.% Cr contents, Cr_2O_3 oxide has formed at the early stage of oxidation and $(Cr, Mn)_3O_4$ spinel oxide has formed at the later stage of oxidation [162]. In previous study, Ferritic stainless steel has shown that selective oxidation behavior depends on the grain orientation and the grain boundary characteristics [93, 94]. In the present study, we investigated the effect of crystallographic orientation on the oxidation resistance and electrical conductivity of the oxide scales that forms in the intra grain during the oxidation of the 22 wt.% Cr containing ferritic stainless steel, Crofer 22 APU.

6.2 Experimental

The selected alloy samples with dimension of 10 mm x 7 mm x 1.5 mm were cut from the commercially available Crofer22 APU plate. Chemical composition of the investigated steel is given in Table 6.1. The samples were ground using 1200 grids SiC abrasive paper. Ground samples were electro polished to get the fine surface for the electron back scattered diffraction (EBSD) analysis. Then the samples were ultrasonically cleaned in acetone and finally dried prior to oxidation. The oxidation tests were conducted at 800 ℃ for 10 min, 1 h and 100 h, following by air cooling.

The oxidation mechanism of these samples was analyzed by scanning electronic microscopy (SEM, Hitachi SE-4300E, Japan) combined EBSD (NordlysMax, Horiba-HKL Technology, UK and *e*-FlashHR, Bruker, Germany). Grain orientation distribution was analyzed using EBSD data reprocessing software (HKL Technology Channel 5 and Esprit 1.9.4). The phase analysis of the oxide layer was carried out X-ray diffraction (XRD, Bruker D8, Germany) using Cu Kα radiation.

The nanoindentor with nanoscale electrical contact resistance (ECR) experiments were performed using on a TriboScan system (TriboScan 8, Hysitron, USA) with a conductive flat ended cube corner tip indenter (diameter: 4 μm), as shown in Figure 6.1. To measure the electrical resistance during an

indentation, we made pillar of different single-crystal orientation with oxide on substrate and the resistance was measured by applying a 5 V voltage across the sample after depth-control. This method measures contact area between the indenter and sample directly. Before the ECR experiments, gold specimen is used as a reference material. For the cross-sectional analyses and ECR, samples were coated using Pt on the sample surface in order to protect the brittle oxide scale on the substrates and milled by focused ion beam (FIB) technique (FEI Helios NanoLab 600, USA).

Table 6.1 Chemical Compositions of Crofer 22 APU (in wt.%).

	Cr	***Fe***	***C***	***Mn***	***Si***	***Cu***	***Al***	***S***	***P***	***Ti***	***La***
Min.	20.0	Bal.		0.30						0.03	0.04
Max.	24.0	Bal.	0.03	0.80	0.50	0.50	0.50	0.02	0.05	0.20	0.20

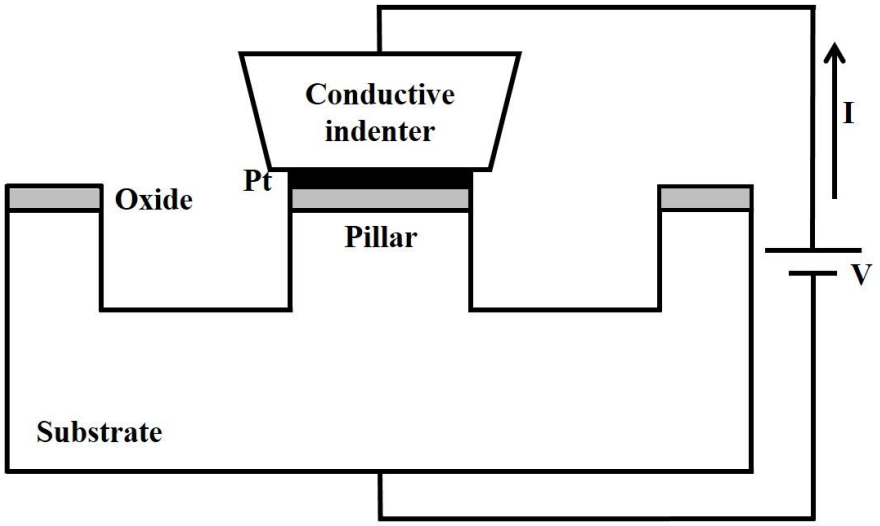

Figure 6.1 Schematic illustration of the indentation experiment with a conductive indenter.

6.3 Results

6.3.1 Grain size and surface morphology of initial oxidation

In order to acquire the orientation information, more than 100 grains in each sample were analyzed using EBSD with a step size 1 μm and the average grain size of samples was 20 μm. As shown in Figure 6.2, Surface morphologies of the grains at the early stage oxidation after 10 min at 800 ℃ are different from grain to grain especially according to their orientation. Orientation of the grains are classified to (100), (110), (111) and (112) grains according to the surface normal direction of the samples. By comparison, before and after oxidation, some grains show brighter contrast than others in SE mode. Oxides on the (100) grains have a dark and bright mixture color, oxides on the (110) grains have a dark color, oxides on the (111) grains have a bright color and oxides on the (112) grains have a medium gray color.

Figure 6.3 a) shows microstructure of oxide scale surfaces of Crofer 22 APU tilted 70 degrees oxidized at 800 ℃ for 100 h. After 100 h of oxidation, oxide crystals appear with different shapes on the substrate of sample. The morphology of intra grain oxides is more clearly shown in the high magnification (Figure 6.3 b)). In particular, oxides on the (110) grains were observed in the flat shapes, oxides on the (111) grains were observed in the shape of granular shapes.

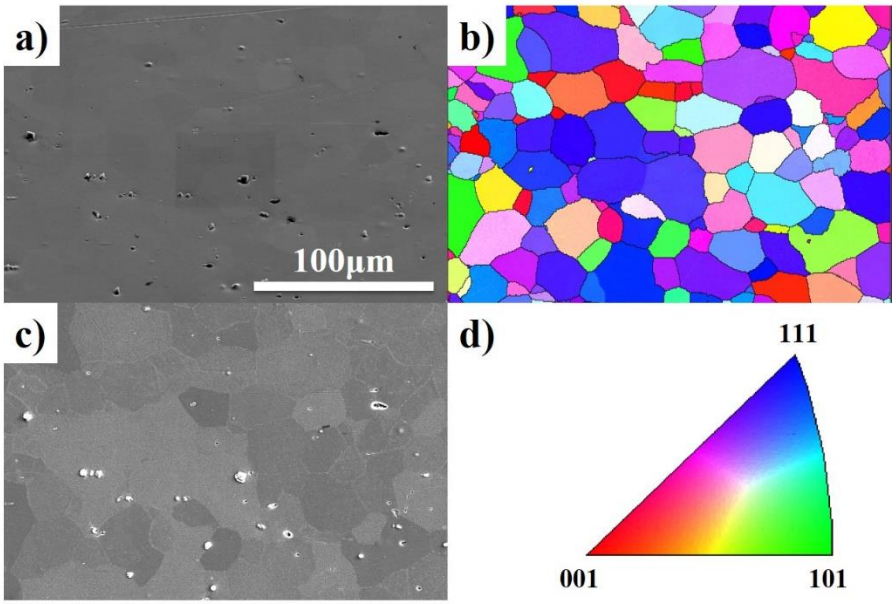

Figure 6.2 a) Secondary electron (SE) image before oxidation, b) Orientation map acquired before oxidation, c) SE image after 10 min oxidation at 800 ℃ and d) Color key of cubic symmetry materials for EBSD orientation map.

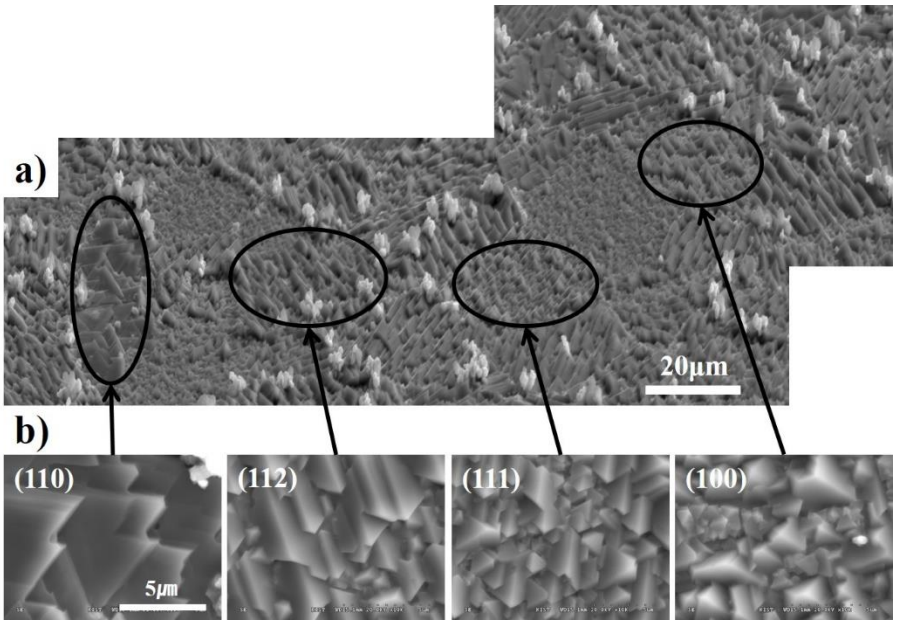

Figure 6.3 Secondary electron (SE) images obtained on the surface of the scale formed after 100 h oxidation, at 800 ℃; a) Tilt SE image of total oxide shape, b) Oxide shape of selected grains (high magnification)

6.3.2 Phase analysis using X-ray diffraction

Figure 6.4 shows the presence of the Fe-Cr stainless steel (Joint Committee Powder Diffraction Standard file: JCPDS 54-0331), Cr_2O_3 (JCPDS: 38-1479), $MnCr_2O_4$ (JCPDS: 54-0876) spinels. As in previous studies [94], the oxide layer developed on Crofer 22APU consists mainly of Cr_2O_3 and $MnCr_2O_4$ spinel. Fe-Cr stainless steel peaks from the matrix were observed because of the thin oxide thickness. Cr_2O_3 peaks were observed from the beginning of the oxidation. After 1 h oxidation, a change in the structure of the oxide layer takes place, the $MnCr_2O_4$ peaks grows together with the initially formed oxides.

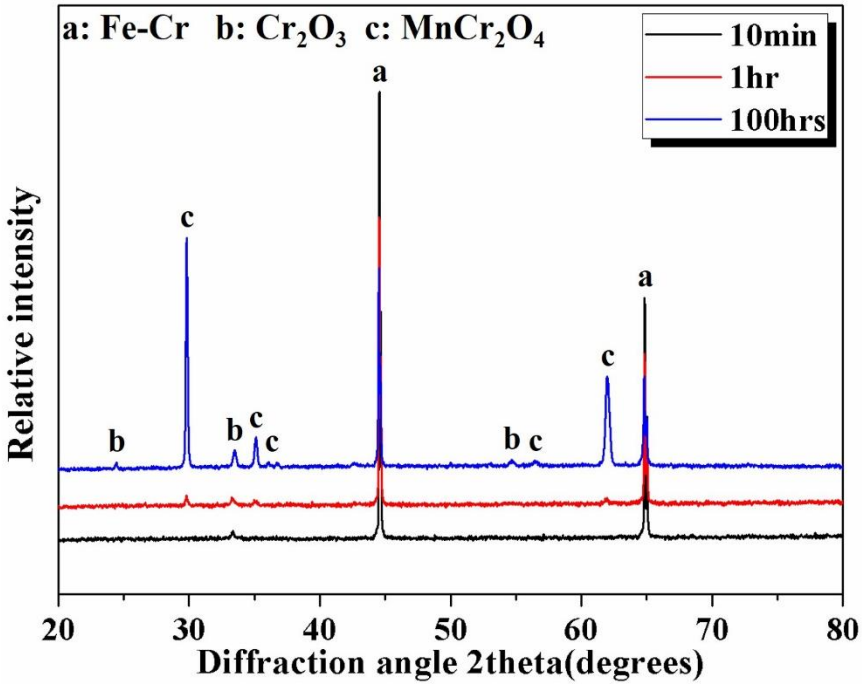

Figure 6.4 X-ray diffraction pattern obtained from the surface of samples after 10 min, 1 h and 100 h of oxidation at 800 ℃.

6.3.3 Oxide thickness analysis for the study of oxidation kinetics

Figure 6.5 shows the cross sectional microstructures of cross section at the substrate and oxide scale after oxidation at 800 ℃ for 1 h. Selected grains were prepared by FIB from oxidation layer after oxidation. The oxide layer was identified as dark parts on the sample substrate with an average thickness of about 50 ~ 90 nm. After 100 h oxidation, the oxide scale is not uniform and the average thickness is from about 650 to 800 nm, respectively. It is shown that the thickness of oxide layer is thickest in (111) grains.

The oxidation rate constant (K_P) can be calculated using equation [163] and are reported in Table 6.2.

$$X^2 = K_P \cdot t \qquad \text{(Equation 6.1)}$$

in which X is the thickness of oxide layer and t is the oxidation time. The values of the oxide layer thickness, X, are given in Figure 6.5 e). The oxidation rate of (111) grain is faster than that of (100), (110) and (112) grain. According to the thickness analysis of Crofer APU oxide scale, grain orientation affects the oxidation resistance and the relative order of oxidation rates is (111) > (112) > (100) > (110) grains when oxidized at 800 ℃ for 100 h.

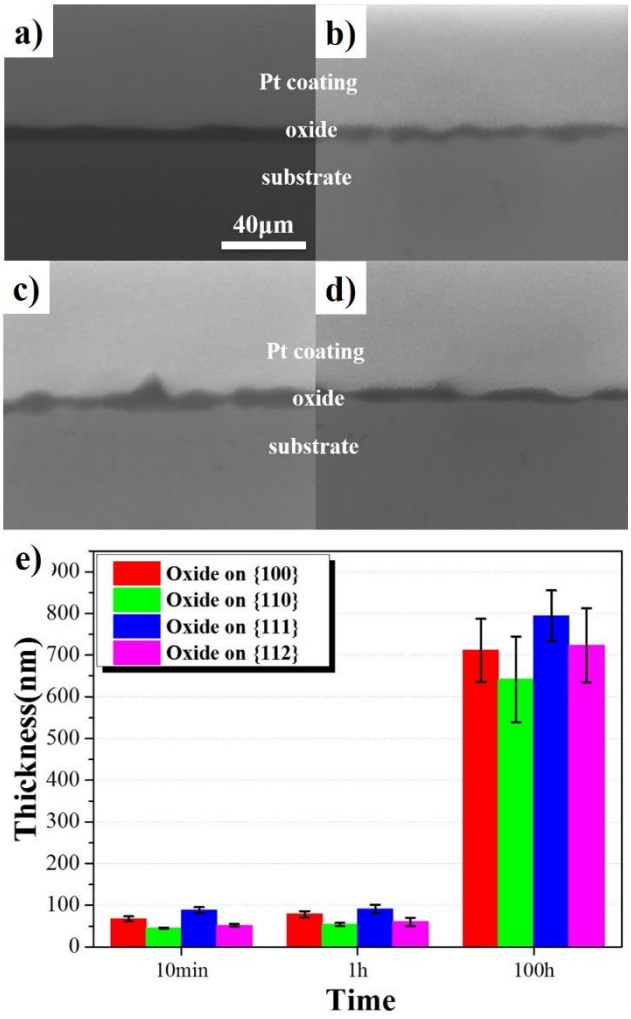

Figure 6.5 Secondary electron (SE) image obtained on cross sections of the scales formed after 1 h oxidation at 800 ℃; a) (100) plane, b) (110) plane, c) (111) plane, d) (112) plane and e) oxide scale thickness of selected grains.

Table 6.2 Oxidation rate constant of various orientation after oxidation at 800 ℃ for 100 h.

	(100)	(110)	(111)	(112)
K_P ($\mu m^2/s^{-1}$)	1.45 x 10^{-4}	1.18 x 10^{-4}	1.80 x 10^{-4}	1.49 x 10^{-4}

6.3.4 Oxide orientation analysis by using EBSD

As shown in Figure 6.6, in order to investigate the oxidation kinetics differences in grains, the EBSD data were analyzed and the presence of texture in the oxides was revealed. EBSD phase analysis can easily distinguish Cr_2O_3 oxide (rhombohedral crystal structure) and Cr_2MnO_4 spinel oxide (cubic crystal structure). The Cr_2O_3 phases (green color in the phase map) are dominantly observed on the adherent subscale after 10 min oxidation at 800 ℃. After 1 h oxidation, a change in the phase of the oxide and Cr_2MnO_4 spinel phases (blue color in the phase map) are formed in the scale. On the other hand, the Cr_2MnO_4 spinel phases are dominantly observed at the top oxide surfaces from the most substrate grains after 100 h oxidation at 800 ℃.

The oxides phase changes in the layer composition seem to be related to the change of the oxidation kinetics. Oxide orientation map also shows the orientation dependency between the substrate grain and the oxide scale and it was reproduced in the oxidation at 800 ℃. Cr_2O_3 on the (100) substrate grains shows (100) plane and Cr_2MnO_4 spinel on Cr_2O_3 oxides are formed random crystal plane. On the (110) substrate grains, Cr_2O_3 are formed with unique (100) plane and almost all Cr_2MnO_4 spinel on them have the same (111) plane. On the (111) substrate grains, Cr_2O_3 and Cr_2MnO_4 spinel are formed with random crystal plane. Finally, on the (112) substrate grains, Cr_2O_3 are formed with (100) plane and Cr_2MnO_4 spinel on them have the same (110) plane.

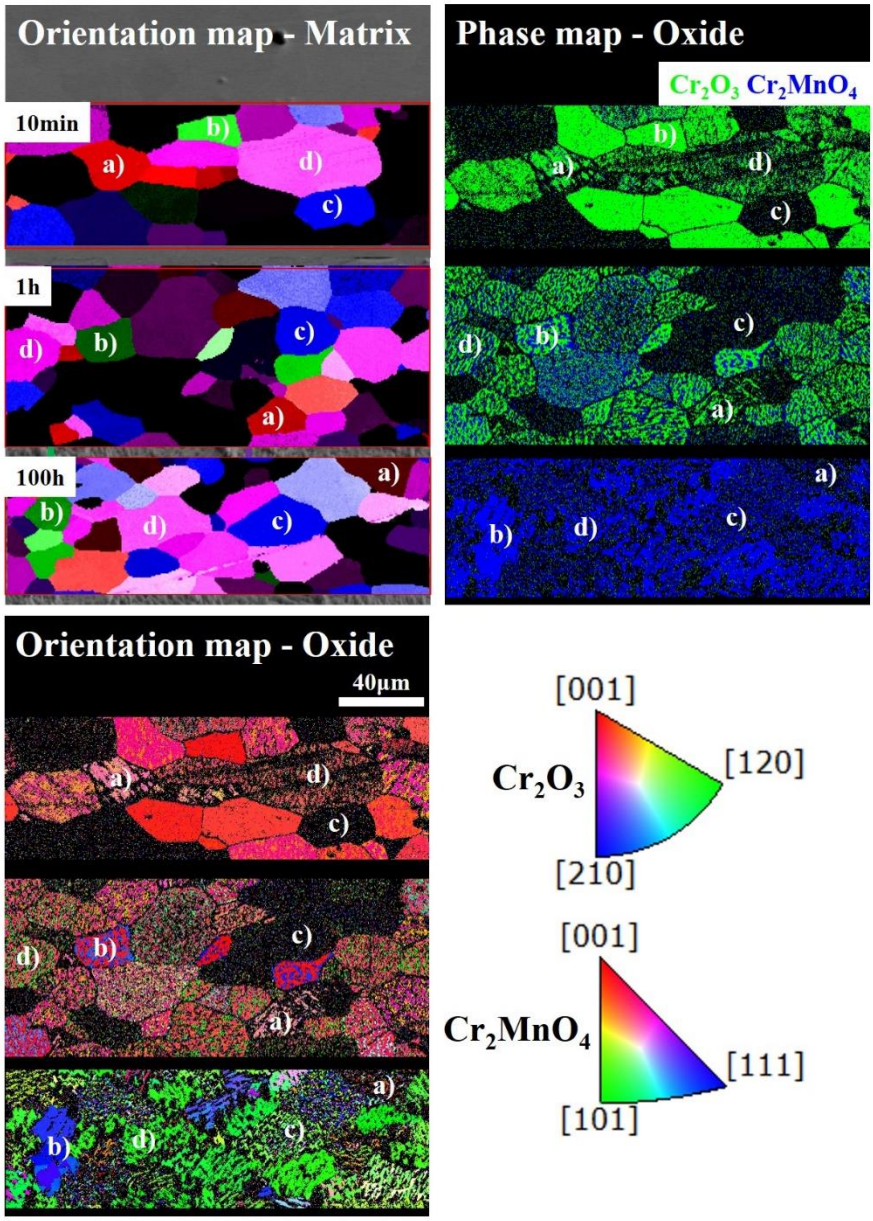

Figure 6.6 EBSD area mapping acquired for each oxidation time and selected grain; a) (100), b) (110), c) (111) and d) (112) surface.

6.3.5 Electrical contact resistance of oxide layer analysis by using ECR

Figure 6.7 shows SEM images of each pillar before ECR test on (100), (110), (111) and (112) substrate grains after 100 h oxidation at 800 ℃. The main geometry parameter for area-specific resistance (ASR), diameter (D) was measured in the SEM and pillar areas are listed in Table 6.3.

The depth-time curves and current for each of the pillars was measured and the results are shown in Figure 6.8. The test was performed under a maximum depth of 75 nm and the corresponding load-displacement curve was also recorded. When the applied depth reached a critical value, holding at this point, the I-V is measured. Then unloading proceeds and the tip are retracted away.

The ASR can be calculated using equation [154] and are reported in Table 6.3.

$$ASR = R \cdot A \qquad \text{(Equation 6.2)}$$

which R is the resistance, A is the contact surface area of the oxide layer.

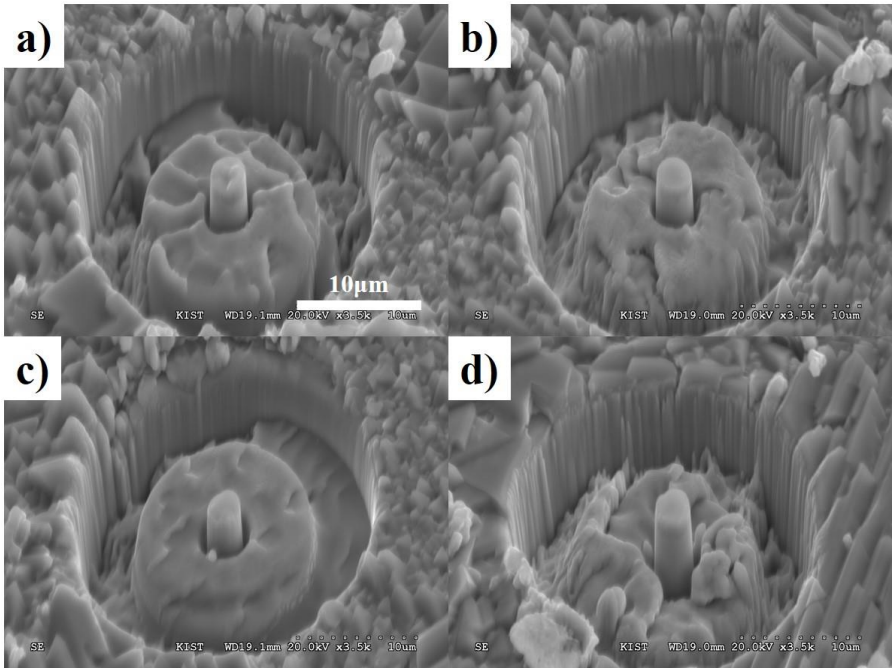

Figure 6.7 Secondary electron (SE) image of a representative single orientation pillar by FIB milling; a) (100), b) (110), c) (111) and d) (112) surface. All images were taken at a ~52° stage tilt.

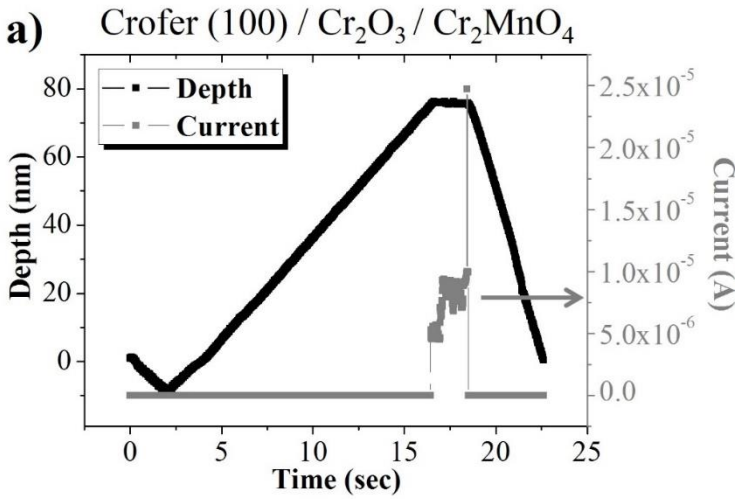
a)
Crofer (100) / Cr_2O_3 / Cr_2MnO_4
Depth
Current
Depth (nm)
Current (A)
Time (sec)
0
20
40
60
80
0.0
5.0x10-6
1.0x10-5
1.5x10-5
2.0x10-5
2.5x10-5
0
5
10
15
20
25

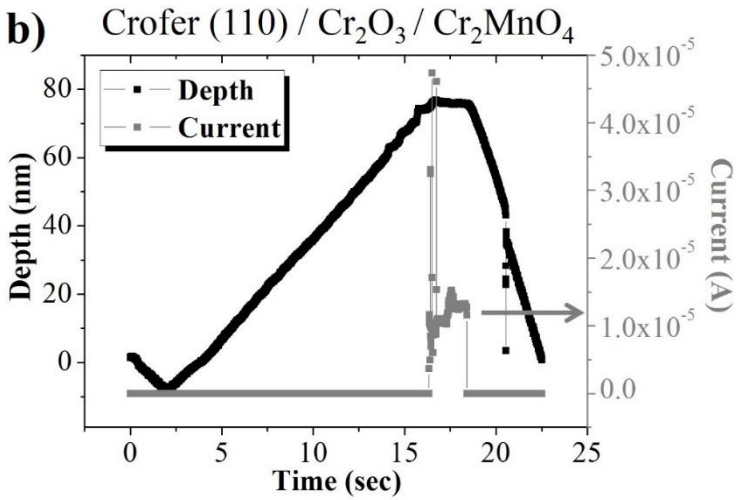
b)
Crofer (110) / Cr_2O_3 / Cr_2MnO_4
Depth
Current
Depth (nm)
Current (A)
Time (sec)
0
20
40
60
80
0.0
1.0x10-5
2.0x10-5
3.0x10-5
4.0x10-5
5.0x10-5
0
5
10
15
20
25

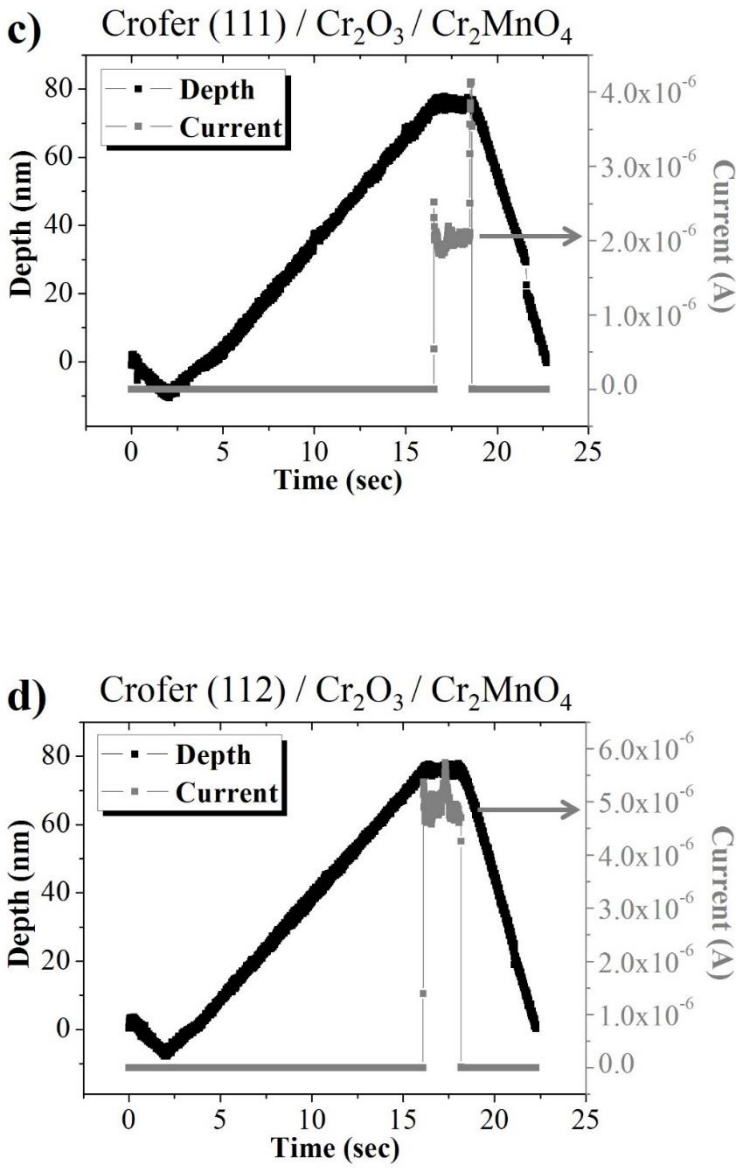

Figure 6.8 Nano-indentation acquired for each electrical current of selected grain after 100 h oxidation at 800 ℃. a) (100), b) (110), c) (111), d) (112)

Table 6.3 ECR properties of oxide scale obtained from nano-indentation test (displacement: 75 nm).

Orientation	Voltage (V)	Current (A)	Resistance (Ω)	Pillar Area (cm^2)	Ares Specific Resistance (Ωcm^2)
(100)	5	7.59E-06	6.59E+05	1.67E-07	1.10E-01
(110)	5	1.20E-05	4.16E+05	1.39E-07	5.81E-02
(111)	5	2.09E-06	2.39E+06	1.53E-07	3.66E-01
(112)	5	4.90E-06	1.02E+06	1.97E-07	2.01E-01

The ASRs of oxides formed on all grains obtained after oxidation at 800 ℃ for 100 h are reported in Table 6.3. The resistances of oxides were increasing from 0.416 to 2.39 MΩ with orientation. The reason why the electrical resistance of oxide was increasing in specific grain, is suggestion that the thickness of oxide layer was increasing during the oxidation. Traditionally it is believed that, an oxide formed on the surface of contact materials may give rise to an additional electrical resistance. In our study, the resistance of oxide were increased with oxide thickness increase. The (110) plane has the best electrical conductivity; the oxide ASR is 0.0581 Ωcm^2. Based on the above results, the oxide scale on the Crofer 22 APU shows the orientation effect. The relative order in oxide ASR is (111) > (112) > (100) > (110) grains after oxidation at 800 ℃ for 100 h.

6.4 Discussion

6.4.1 Orientation relationship between matrix and oxides

The oxidation behavior analysis reveals that the surface orientation plays an important role on the oxidation. Cr_2O_3 oxide formed during the early stage of oxidation has close orientation relationship with the substrate grain orientation. In this study, the (110) substrate grain a (001) oriented Cr_2O_3 oxide has formed. From the orientation relationship between the substrate and the oxide, we can deduce a closed packed oxide structure (HCP) forms on the closed packed plane of the substrate (BCC). It is considered that the orientation relationship between the surface (BCC) and the Cr_2O_3 (HCP) follows the Pitsch-Schrader relationship [164]. After 10 h oxidation, the Cr_2MnO_4 oxides observed as small particles on Cr_2O_3 oxide layer. Whereas the particles of the oxides covered whole oxide surface after 100 h oxidation.

The Cr_2MnO_4 on (110) grain has a (111) orientation, on (100) surface occurs a (110) oriented oxide layer and on (111) surface occurs a random oriented oxide layer. It is considered that the orientation relationship between the surface (BCC) and the Cr_2MnO_4 oxide (FCC) follows the Nishiyama-Wassermann relationship [151, 152]. But, the Cr_2MnO_4 forms on the Cr_2O_3 instead of BCC substrate so it is more reasonable to understand that Cr_2MnO_4 close packed structure forms on the Cr_2O_3 close packed structure. As indicated

above, this selective oxidation is mainly due to the short-circuit diffusion paths on surfaces. These short-circuit diffusion paths are generated because an oxide scale contains a number of structural defects. It has also been confirmed that the oxide layer on the (111) surface produce of grain boundaries and granular shapes for fine random orientation. A higher concentration of grain boundaries may promote higher diffusion than the surface. Therefore, the surfaces with different crystallographic orientations exhibit differences in oxidation rate.

6.4.2 Contact resistance of oxides

The contact resistance of an oxidized metallic interconnect is usually characterized by the ASR, which is the product of electrical resistivity of the oxide layer and oxide thickness. As it was already mentioned Equation 6.1 in this paper can be as follow:

$$ASR = \rho \cdot X \qquad \text{(Equation 6.3)}$$

which ρ is the resistivity and X is the thickness of the oxide layer. ρ take into account that:

$$\rho = \frac{1}{\sigma} \qquad \text{(Equation 6.4)}$$

The conductivity (σ) can be calculated from the formula:

$$\sigma = \frac{1}{T} f \, exp\left(\frac{-E_a}{RT}\right) \qquad \text{(Equation 5.5)}$$

in which f is a pre-exponential constant, E_a is the activation energy, R is the universal gas constant and T the temperature [165]. It is possible to predict for a particular temperature. The temperature dependence of the electrical conductivity of the oxide layers compared with literature data for Cr_2O_3 [166] and Cr_2MnO_4 [167] in Figure 6.9. From the slop of plot, the activation energy and the pre-exponential constant for electrical conductivity were calculated for each oxide. That means that the predicted behavior of the conductivity for room temperatures using literature date and above equation. The calculated values show that the conductivity increases with increasing temperature so the resistivity at room temperature will be higher than at high temperature.

To be able to compare the measured resistance results with the conductivity data in literature, the ASRs were calculated to conductivity thereby measured oxide thicknesses in Figure 6.5. Although the results in Figure 6.9 clearly show conductivity of oxide layer on Crofer 22 APU shows orientations dependency, it is not a strict way to compare the absolute values determined from previously reported literature data with actual measured data, it is interesting that the measured data are in a range comparable with the value of reported literature.

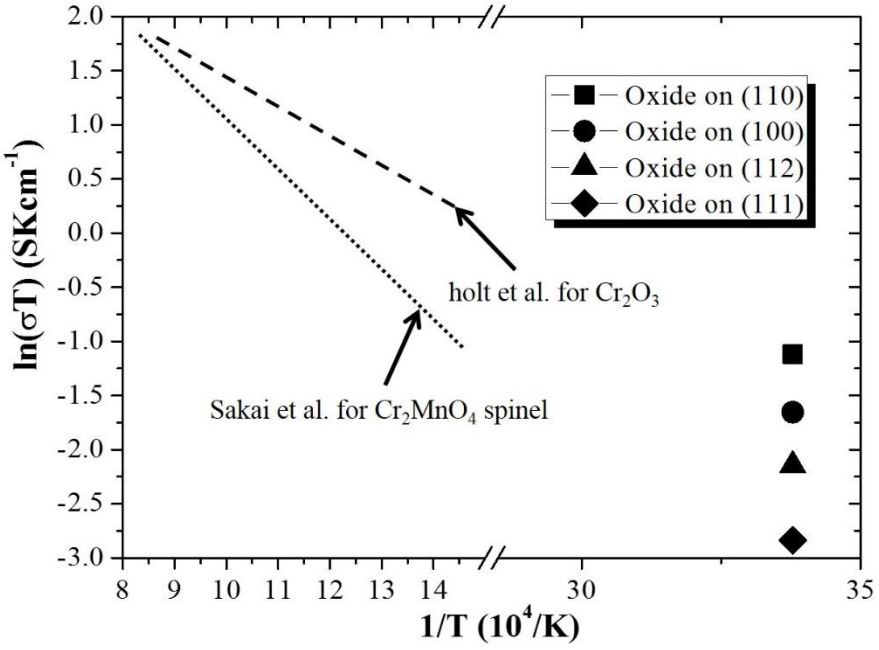

Figure 6.9 Plot of ln(σT) versus 1/T, electrical conductivity of oxide on each orientation in this work with literature data for Cr_2O_3 and Cr_2MnO_4.

6.5 Summary

The aim of this study was to investigate the effects of orientation on the oxidation behavior of Crofer 22APU. Oxide thickness and electrical contact resistance results showed that the grain orientation can affect the oxidation rate of ferritic stainless steels.

Grain orientation was classified to some representative orientations of (100), (110), (111) and (112) grains. The effect of grain orientation on the oxidation resistance and electrical conductivity of oxide layers on Crofer 22 APU has been investigated. (110) surface is the most effective orientation because the oxide on (110) surface decrease the oxidation rate as well as the area-specific resistance.

Chapter 7

Conclusions

7.1 Cu added austenitic stainless steels (Super304H)

The high temperature oxidation behavior of a Cu added austenitic stainless steel has been studied with respect to the role of the grain boundaries and the resulting critical grain size to form a uniform protective Cr_2O_3 oxide. The following conclusions can be drawn:

1) Selective oxidation of high oxidation resistance is observed within a certain distance from random grain boundaries towards the grain interiors. Σ3 CSL grain boundaries do not affect selective oxidation. Thus, the oxidation rate depends on the grain size neglecting Σ3 boundaries.

2) For the initial stage (~30 min) oxidation, the outer oxide layers formed < 4 μm within from random grain boundaries and are mainly composed of a protective Cr_2O_3 with rhombohedral crystal structure with thin Fe-rich $(Fe,Cr)_3O_4$ on top. On the other hand, in case of the outer oxide layer formed more than 4 μm away from random grain boundaries it consists of thick Fe-rich $(Fe,Cr)_3O_4$ oxide with a spinel crystal structure containing

small amounts of Ni, Mn and Cu while the inner layer consists mainly of Cr-rich $(Fe,Cr)_3O_4$ oxide with a spinel crystal structure.

3) In the later stage (2 h~) oxidation samples with large grain size (> 8 μm) form a duplex oxide. A thick Fe-oxide is formed on the intra grain regions while a thinner Cr-rich oxide is manufactured at the grain boundaries. These results are in contrast to the observation of samples with a small grain size (< 8 μm) for which a uniform protective Cr-rich oxide is formed. As a result, the overall oxidation of small-grained sample can be suppressed.

4) In small grain (8 μm) sample, oxidation kinetics follow a parabolic raw caused by the formation of protective Cr-rich oxide on the sample surface, but the large grain sample shows the relatively fast oxidation rate due to the formation of a non-protective iron oxide (Fe-rich oxide is present on the outer surface as nodules). The protective oxidation behavior of small grain sample is result from the slow oxidation rate attributed by the dense Cr_2O_3 oxide layer due to enough Cr supply through the high density grain boundary area.

5) The present study shows that grain size refinement (with a critical grain size of 8 μm) is an advantageous approach, without increasing the Cr content or adding additional elements, to increase the resistance to the high temperature oxidation under a humid air conditions.

6) Also, the effect of Cu addition to the austenitic stainless steel after 500 h oxidation at 700 ℃ was successively investigated by EBSD-EBSD simultaneous analysis technique. Inner oxide consists of $FeCr_2O_4$ with small amount of Cr_2O_3. Outer oxide has multi layered structure with magnetite-Cu containing spinel oxide (Fe_2CuO_4) solid solution, Fe_2O_3, and Fe_3O_4. Fe_2CuO_4 solid solution at the top surface of the outer oxide results from the Cu enrichment during the oxidation heat treatment.

7.2 22 wt.% Cr ferritic stainless steels (Crofer 22 APU)

The effect of grain orientation 22 wt.% Cr containing ferritic stainless steel (Crofer 22 APU) on the oxidation behavior and electrical conductivity on crofer 22 APU has been investigated. Oxide thickness and electrical contact resistance results showed that the surface orientation can have an effect on the oxidation resistance and electrical conductivity.

1) The oxide thickness and oxide granule shape of Crofer 22 APU varies according to the grain orientation during the high temperature oxidation.

2) By correlating results from EBSD and SEM, the oxides formed on (111) matrix grain exhibits a higher K_P value than the oxide formed on (100), (110) and (112) matrix grain.

3) The oxide on (110) grain has the best electrical conductivity after oxidation. Moreover, the ASR value is lower than $0.10 \Omega cm^2$ for the Crofer 22 APU during operating temperature of SOFC at 800 ℃.

4) (110) surface is the most effective orientation for decreasing the oxidation rate as well as the area-specific resistance of the oxide formed on Crofer 22 APU steel.

Bibliography

[1] P. Kofstad, High Temperature Oxidation of Metals, John Wiley & Son, New York, NY, 1966.

[2] N. Birks, G.H. Meier, F.S. Pettit, Introduction to the High Temperature Oxidation of Metals, 2nd ed., Cambridge University Press, Cambridge, 2006.

[3] P. Sarrazin, A. Galerie, J. Fouletier, Mechanisms of High Temperature Corrosion: a Kinetic Approach, Trans Tech Publications Ltd., Zurich, Switzerland, 2008.

[4] J.M. West, Basic Corrosion and Oxidation, John Wiley and Sons Inc., New York, NY, 1986.

[5] A.J. Sedriks, Corrosion of Stainless Steels,, 2nd ed., Wiley-Interscience, Canada, 1996.

[6] G.C. Wood, The oxidation of iron-chromium alloys and stainless steels at high temperatures, Corrosion Science, 2 (1962) 173-196.

[7] D.J. Young, High temperature oxidation and corrosion of metals, Elsevier Ltd., Oxford, UK, 2008.

[8] D.R. Gaskell, Introduction to the Thermodynamics of Materials, 4th ed., Taylor & Francis, London, 2003.

[9] S. Osgerby, Development of de-alloyed zones during oxidation: effects on microstructure and spallation behaviour, Materials Science and Technology, 16

(2000) 1233-1237.

[10] J.P.T. Vossen, P. Gawenda, K. Rahts, M. Rohrig, M. Schorr, M. Schutze, Limits of the oxidation resistance of several heat-resistant steels under isothermal and cyclic oxidation as well as under creep in air at 650-degrees-c Materials at high temperatures 14 (1997) 387-401.

[11] S.R.J. Saunders, M. Monteiro, F. Rizzo, The oxidation behaviour of metals and alloys at high temperatures in atmospheres containing water vapour: A review, Progress in Materials Science, 53 (2008) 775-837.

[12] E.J. Opila, Volatility of Common Protective Oxides in High-Temperature Water Vapor: Current Understanding and Unanswered Questions, Materials Science Forum, 461-464 (2004) 765-774.

[13] A. Fry, S. Osgerby, M. Wright, Oxidation of Alloys in Steam Environments: a Review, in, NPL Report MATC(A) 90, NPL Materials Centre, 2002, pp. 1-39.

[14] C.T. Fujii, R.A. Meussner, The Mechanism of the High-Temperature Oxidation of Iron-Chromium Alloys in Water Vapor, Journal of The Electrochemical Society, 111 (1964) 1215-1221.

[15] C.T. Fujii, R.A. Meussner, Oxide Structures Produced on Iron-Chromium Alloys by a Dissociative Mechanism, Journal of The Electrochemical Society, 110 (1963) 1195-1204.

[16] Y. Ikeda, K. Nii, Mechanism of accelerated oxidation of Fe-Cr alloys in water vapor containing atmosphere, Transactions of National Research Institute

for Metals, 26 (1984) 52-62.

[17] Y. Ikeda, K. Nii, Microcrack generation and its healing in the oxide scale formed on Fe-Cr alloys, Oxidation of Metals, 12 (1978) 487-502.

[18] P.L. Surman, J.E. Castle, Gas phase transport in the oxidation of Fe and steel, Corrosion Science, 9 (1969) 771-777.

[19] P.L. Surman, The oxidation of iron at controlled oxygen partial pressures - I. Hydrogen/water vapour, Corrosion Science, 13 (1973) 113-124.

[20] F. Armanet, A. Vejux, G. Beranger, Behaviour of High Temperature Alloys in Aggressive Environments, The Metals Society, London, 1980.

[21] A. Galerie, Y. Wouters, M. Caillet, The kinetic behaviour of metals in water vapour at high temperatures: Can General rules be proposed?, Materials Science Forum, Trans Tech Publ, 2001, pp. 231-238.

[22] D. Abriou, J. Jupille, Self-inhibition of water dissociation on magnesium oxide surfaces, Surface Science, 430 (1999) L527-L532.

[23] S. Warren, W.R. Flavell, A.G. Thomas, J. Hollingworth, P.M. Dunwoody, S. Downes, C. Chen, Adsorption of H_2O on single crystal CuO, Surface Science, 436 (1999) 1-8.

[24] N. Otsuka, H. Fujikawa, Scaling of austenitic stainless steels and nickel-base alloys in high-temperature steam at 973 K, Corrosion, 47 (1991) 240-248.

[25] J.R. Davis, Stainless steels, ASM international, 1994.

[26] H. Fujikawa., S.B. Newcomb, High Temperature Oxidation Behaviour of High Al Content Ferritic and Austenitic Stainless Steels With and Without

Rare-Earth Element Addition, Oxidation of Metals, 77 (2012) 85-92.

[27] Y. Otoguro, M. Sakakibara, T. Saito, H. Ito, Y. Inoue, Oxidation behavior of austenitic heat-resisting steels in a high temperature and high pressure steam environment, ISIJ International, 28 (1988) 761-768.

[28] H. Teranishi, Y. Sawaragi, M. Kubota, Y. Hayase, Fine-Grained TP347H Steel Tubing with High Elevated-Temperature Strength and Corrosion Resistance for Boiler Applications, The Sumitomo Search, 38 (1989) 63-74.

[29] H. Teranishi, Application of Finegrained Austenitic Stainless Steel Tubes to Superheaters in Power Boilers, International Conference on Creep, Tokyo, 1986, pp. 223-238.

[30] O. Engler, V. Randle, Introduction to Texture Analysis: Macrotexture, Microtexture, and Orientation Mapping, 2nd ed., CRC Press, Boca Raton, 2009.

[31] J. Goldstein, D. Newbury, D. Joy, L. C, P. Echlin, E. Lifshin, L. Sawyer, J. Michael, Scanning Electron Microscopy and X-Ray Microanalysis, Kluwer Academic, Plenum Publishers, New York, 2003.

[32] Y. Leng, Materials Characterization: Introduction to Microscopic and Spectroscopic Methods, 2nd ed., Wiley-VCH, 2013.

[33] A.J. Schwartz, M. Kumar, B.L. Adams, D.P. Field, Electron Backscatter Diffraction in Materials Science, 2nd ed., Springer, 2009.

[34] Y. Waseda, E. Matsubara, K. Shinoda, X-Ray Diffraction Crystallography, 1st ed., Springer-Verlag Berlin Heidelberg, 2011.

[35] G. Gottstein, Physical Foundations of Materials Science, Springer, Berlin,

2005.

[36] C.A. Volkert, A.M. Minor, Focused Ion Beam Microscopy and Micromachining, MRS Bulletin, 32 (2007) 389-399.

[37] L.A. Giannuzzi, F.A. Stevie, Introduction to Focused Ion Beams, Springer US, NY, 2005.

[38] N. Yao, Focused Ion Beam Systems : Basics and Applications, Cambridge University Press, NY, 2011.

[39] FEI, http://www.fei.com/products/dualbeam/helios-nanolab-600i-for-materials-science/, 2015.

[40] MYScope, http://www.ammrf.org.au/myscope/tem/introduction/, 2013.

[41] D.B. Williams, C.B. Carte, Transmission Electron Microscopy: A Textbook for Materials Science, Springer US, NY, 2009.

[42] O. Engler, V. Randle, Introduction to texture analysis: macrotexture, microtexture, and orientation mapping, 2nd ed., CRC press, 2009.

[43] T.F. Kelly, M.K. Miller, Atom probe tomography, Review of Scientific Instruments, 78 (2007) 031101.

[44] E.W. Müller, The atom-probe field ion microscope, Naturwissenschaften, 57 (1970) 222-230.

[45] E.W. Müller, K. Bahadur, Field Ionization of Gases at a Metal Surface and the Resolution of the Field Ion Microscope, Physical Review, 102 (1956) 624-631.

[46] E.W. Müller, J. Panitz, The Atom-Probe Field Ion microscope, the 14th

International Field Emission Symposium, National Bureau of Standards, Washington, DC, 1967.

[47] B. Gault, M.P. Moody, J.M. Cairney, S.P. Ringer, Atom probe microscopy, Springer Science & Business Media, New York, 2012.

[48] A. Zieliński, Austenitic steels for boiler elements in USC power plants, Journal of Achievements in Materials and Manufacturing Engineering, 57 (2013) 68-75.

[49] C. Chi, H. Yu, X. Xie, Advanced Austenitic Heat-Resistant Steels for Ultra-Super-Critical (USC) Fossil Power Plants, InTech, 2011.

[50] C.A. Powell, B.D. Morreale, Materials Challenges in Advanced Coal Conversion Technologies, MRS Bulletin, 33 (2008) 309-315.

[51] C. Chi, H. Yu, J. Dong, X. Xie, Z. Cui, X. Chen, F. Lin, Strengthening effect of Cu-rich phase precipitation in 18Cr9Ni3CuNbN austenitic heat-resisting steel, Acta Metall. Sin.(Engl. Lett.), 24 (2011) 141-147.

[52] C. Chi, H. Yu, J. Dong, W. Liu, S. Cheng, Z. Liu, X. Xie, The precipitation strengthening behavior of Cu-rich phase in Nb contained advanced Fe-Cr-Ni type austenitic heat resistant steel for USC power plant application, Progress in Natural Science: Materials International, 22 (2012) 175-185.

[53] B.M. Gonzalez, C.S.B. Castro, V.T.L. Buono, J.M.C. Vilela, M.S. Andrade, J.M.D. Moraes, M.J. Mantel, The influence of copper addition on the formability of AISI 304 stainless steel, Materials Science and Engineering A, 343 (2003) 51-56.

[54] Y. Sawaragi, S. Hirano, The Development of a New 18-8 Austenitic Stainless Steel (0.1C-18Cr-9Ni-3Cu-Nb, N) with High Elevated Temperatures Strength for Fossil Power Boilers, in: M.J. Inoue (Ed.) Mechanical Behaviour of Materials VI, Pergamon, Oxford, 1992, pp. 589-594.

[55] Y. Sawaragi, N. Otsuka, H. Senba, S. Yamamoto, Properties of a new 18-8 austenitic steel tube (SUPER 304H) for fossil fired boilers after service exposure with high elevated temperature strength, Sumitomo Search, (1994) 34-43.

[56] F. Riffard, H. Buscail, E. Caudron, R. Cueff, C. Issartel, S.E. Messki, S. Perrier, A new interpretation of the "breakaway" oxidation behaviour observed at high temperature on 304 stainless steel, Materials Science Forum, 461-464 (2004) 175-182.

[57] X. Peng, J. Yan, Y. Zhou, F. Wang, Effect of grain refinement on the resistance of 304 stainless steel to breakaway oxidation in wet air, Acta Materialia, 53 (2005) 5079-5088.

[58] S. Cissé, L. Laffont, B. Tanguy, M.-C. Lafont, E. Andrieu, Effect of surface preparation on the corrosion of austenitic stainless steel 304L in high temperature steam and simulated PWR primary water, Corrosion Science, 56 (2012) 209-216.

[59] F. Riffard, H. Buscail, E. Caudron, R. Cueff, C. Issartel, S. Perrier, Effect of yttrium addition by sol–gel coating and ion implantation on the high temperature oxidation behaviour of the 304 steel, Applied Surface Science, 199

(2002) 107-122.

[60] F.J. Pérez, M.J. Cristóbal, M.P. Hierro, F. Pedraza, G. Arnau, P. Merino, Effect of yttrium and erbium ion implantation on the oxidation behaviour of the AISI 304 austenitic steel, Surface and Coatings Technology, 126 (2000) 116-122.

[61] F.J. Pérez, E. Otero, M.P. Hierro, C. Gómez, F. Pedraza, J.L.d. Segovia, E. Román, High temperature corrosion protection of austenitic AISI 304 stainless steel by Si, Mo and Ce ion implantation, Surface and Coatings Technology, 108-109 (1998) 127-131.

[62] C. Issartel, H. Buscail, E. Caudron, R. Cueff, F. Riffard, S.E. Messki, S. Perrier, P. Jacquet, M. Lambertin, Nitridation effect on the oxidation of a austenitic stainless steel AISI 304 at 900 ℃, Applied Surface Science, 225 (2004) 14-20.

[63] M.D. Merz, The oxidation resistance of fine-grained sputter-deposited 304 stainless steel, Metallurgical Transactions A, 10 (1979) 71-77.

[64] T. Tanabe, S. Imoto, Surface Oxidation of Type 316 Stainless Steel, Transactions of the Japan Institute of Metals, 20 (1979) 507-515.

[65] M.J. Capitán, A. Paúl, J.L. Pastol, J.A. Odriozola, X-Ray Diffraction Study of Oxide Scales Formed at High Temperatures on AISI 304 Stainless Steel After Cerium Deposition, Oxidation of Metals, 52 (1999) 447-462.

[66] G. Betz, G.K. Wehner, L. Toth, A. Joshi, Composition-vs-depth profiles obtained with Auger electron spectroscopy of air-oxidized stainless-steel

surfaces, Journal of Applied Physics, 45 (1974) 5312-5316.

[67] L. Dong-Sheng, D. Qi-Xun, C. Xiao-Nong, W. Rong-Rong, H. Yan, High-Temperature Oxidation Resistance of Austenitic Stainless Steel Cr18Ni11Cu3Al3MnNb, Journal of Iron and Steel Research, International, 19 (2012) 74-78.

[68] E.A. Gulbransen, K.F. Andrew, Oxidation Studies on 304 Stainless Steel, Journal of The Electrochemical Society, 109 (1962) 560-564.

[69] H. Asteman, J.-E. Svensson, M. Norell, L.-G. Johansson, Influence of Water Vapor and Flow Rate on the High-Temperature Oxidation of 304L; Effect of Chromium Oxide Hydroxide Evaporation, Oxidation of Metals, 54 (2000) 11-26.

[70] H. Asteman, J.-E. Svensson, L.-G. Johansson, Oxidation of 310 steel in H_2O/O_2 mixtures at 600 °C: the effect of water-vapour-enhanced chromium evaporation, Corrosion Science, 44 (2002) 2635-2649.

[71] G.C. Allen, J.M. Dyke, S.J. Harris, A. Morris, A surface study of the oxidation of type 304L stainless steel at 600 K in air, Oxidation of Metals, 29 (1988) 391-408.

[72] D.R. BAER, Protective and non-protective oxide formation on 304 stainless steel, Applications of Surface Science, 7 (1981) 69-82.

[73] D.P. Whittle, J. Stringer, Improvements in High Temperature Oxidation Resistance by Additions of Reactive Elements or Oxide Dispersions, Philosophical Transactions of the Royal Society of London A: Mathematical,

Physical and Engineering Sciences, 295 (1980) 309-329.

[74] G.J. Yurek, D. Eisen, A. Garratt-Reed, Oxidation behavior of a fine-grained rapidly solidified 18-8 stainless steel, Metallurgical and Materials Transactions A, 13 (1982) 473-485.

[75] F.H. Stott, G.C. Wood, J. Stringer, The influence of alloying elements on the development and maintenance of protective scales, Oxidation of Metals, 44 (1995) 113-145.

[76] N. Karimi, F. Riffard, F. Rabaste, S. Perrier, R. Cueff, C. Issartel, H. Buscail, Characterization of the oxides formed at 1000 ℃ on the AISI 304 stainless steel by X-ray diffraction and infrared spectroscopy, Applied Surface Science, 254 (2008) 2292-2299.

[77] S.E. Ziemniak, M. Hanson, Corrosion behavior of 304 stainless steel in high temperature, hydrogenated water, Corrosion Science, 44 (2002) 2209-2230.

[78] A.M. Huntz, A. Reckmann, C. Haut, C. Sévérac, M. Herbst, F.C.T. Resende, A.C.S. Sabioni, Oxidation of AISI 304 and AISI 439 stainless steels, Materials Science and Engineering: A, 447 (2007) 266-276.

[79] H.E. Evans, D.A. Hilton, R.A. Holm, Chromium-depleted zones and the oxidation process in stainless steels, Oxidation of Metals, 10 (1976) 149-161.

[80] R.C. Lobb, H.E. Evans, Formation of protective oxide film on chromium-depleted stainless steel, Metal Science, 15 (1981) 267-274.

[81] I.G. Wright, B.A. Pint, An Assessment of the High Temperature Oxidation

Behavior of Fe-Cr Steels in Water Vapor and Steam, CORROSION 2002, NACE International, 2002.

[82] D.R. Baer, M.D. Merz, Differences in oxides on large-and small-grained 304 stainless steel, Metallurgical and Materials Transactions A, 11 (1980) 1973-1980.

[83] S.N. Basu, G.J. Yurek, Effect of alloy grain size and silicon content on the oxidation of austenitic Fe-Cr-Ni-Mn-Si alloys in pure O_2, Oxidation of Metals, 36 (1991) 281-315.

[84] J.-H. Kim, D.-I. Kim, S. Suwas, E. Fleury, K.-W. Yi, Grain-Size Effects on the High-Temperature Oxidation of Modified 304 Austenitic Stainless Steel, Oxidation of Metals, 79 (2013) 239-247.

[85] S.G. Wang, M. Sun, H.B. Han, K. Long, Z.D. Zhang, The high-temperature oxidation of bulk nanocrystalline 304 stainless steel in air, Corrosion Science, 72 (2013) 64-72.

[86] T. Terachi, T. Yamada, T. Miyamoto, K. Arioka, K. Fukuya, Corrosion Behavior of Stainless Steels in Simulated PWR Primary Water - Effect of Chromium Content in Alloys and Dissolved Hydrogen, Journal of Nuclear Science and Technology, 45 (2008) 975-984.

[87] K. Kruska, S. Lozano-Perez, D.W. Saxey, T. Terachi, T. Yamada, G.D.W. Smith, Nanoscale characterisation of grain boundary oxidation in cold-worked stainless steels, Corrosion Science, 63 (2012) 225-233.

[88] C. Oberdorfer, P. Stender, C. Reinke, G. Schmitz, Laser-Assisted Atom

Probe Tomography of Oxide Materials, Microscopy and Microanalysis, 13 (2007) 342-346.

[89] S. Lozano-Perez, D.W. Saxey, T. Yamada, T. Terachi, Atom-probe tomography characterization of the oxidation of stainless steel, Scripta Materialia, 62 (2010) 855-858.

[90] K. Thompson, D. Lawrence, D.J. Larson, J.D. Olson, T.F. Kelly, B. Gorman, In situ site-specific specimen preparation for atom probe tomography, Ultramicroscopy, 107 (2007) 131-139.

[91] J. Takahashi, K. Kawakami, Y. Yamaguchi, M. Sugiyama, Development of atom probe specimen preparation techniques for specific regions in steel materials, Ultramicroscopy, 107 (2007) 744-749.

[92] M.K. Miller, K.F. Russell, Atom probe specimen preparation with a dual beam SEM/FIB miller, Ultramicroscopy, 107 (2007) 761-766.

[93] M.P. Phaniraj, D.-I. Kim, Y.W. Cho, Effect of grain boundary characteristics on the oxidation behavior of ferritic stainless steel, Corrosion Science, 53 (2011) 4124-4130.

[94] D.-I. Kim, S.H. Hong, M.P. Phaniraj, H.N. Han, J.-P. Ahn, Y.W. Cho, Microstructural analysis of oxide layer formation in ferritic stainless steel interconnects, Materials at High Temperatures, 28 (2011) 285-289.

[95] B. Chattopadhyay, G.C. Wood, The Transient Oxidation of Fe-Cr and Ni-Cr Alloys, Journal of The Electrochemical Society, 117 (1970) 1163-1171.

[96] M.G.C. Cox, B. McEnaney, V.D. Scott, Vacancy condensation and void

formation in duplex oxide scales on alloys, Philosophical Magazine, 28 (1973) 309-319.

[97] C. Desgranges, F. Lequien, E. Aublant, M. Nastar, D. Monceau, Depletion and Voids Formation in the Substrate During High Temperature Oxidation of Ni-Cr Alloys, Oxidation of Metals, 79 (2013) 93-105.

[98] Y.F. Gong, B.C.D. Cooman, Kirkendall Void Formation During Selective Oxidation, Metallurgical and Materials Transactions A, 41 (2010) 2180-2183.

[99] N. Otsuka, Y. Shida, H. Fujikawa, Internal-external transition for the oxidation of Fe-Cr-Ni austenitic stainless steels in steam, Oxidation of Metals, 32 (1989) 13-45.

[100] C. Chi, J. Dong, W. Liu, X. Xie, 3DAP investigation of precipitation behavior of Cu-rich phase in Super304H heat resistant steel, Jinshu Xuebao/Acta Metallurgica Sinica, 46 (2010) 1141-1146.

[101] J.-H. Kim, D.-I. Kim, J.-H. Shim, K.-W. Yi, Investigation into the high temperature oxidation of Cu-bearing austenitic stainless steel using simultaneous electron backscatter diffraction-energy dispersive spectroscopy analysis, Corrosion Science, 77 (2013) 397-402.

[102] J.-H. Kim, D.-I. Kim, P.-P. Choi, D. Raabe, K.-W. Yi, Atomic scale observations of Phase transformations (FCC→BCC) along the grain boundary during oxidation of Cu added Austenite stainless steel at 700 ℃, in preparation.

[103] N.K. Das, K. Suzuki, K. Ogawa, T. Shoji, Early stage SCC initiation analysis of fcc Fe-Cr-Ni ternary alloy at 288 ℃: A quantum chemical molecular

dynamics approach, Corrosion Science, 51 (2009) 908-913.

[104] T. Terachi, K. Fujii, K. Arioka, Microstructural characterization of SCC crack tip and oxide film for SUS 316 stainless steel in simulated PWR primary water at 320 ℃, Journal of Nuclear Science and Technology, 42 (2005) 225-232.

[105] C. Wagner, Atom Movements American society of metals, Cleveland, 1951.

[106] B. Pieraggi, Calculations of parabolic reaction rate constants, Oxidation of Metals, 27 (1987) 177-185.

[107] C. Wagner, Journal of Physical Chemistry, Journal of Physical Chemistry, B21 (1933) 25.

[108] A.F. Smith, The oxidation of an 18/8 type stainless steel in CO_2, Materials and Corrosion, 30 (1979) 100-104.

[109] G.C. Wood, High-temperature oxidation of alloys, Oxidation of Metals, 2 (1970) 11-57.

[110] S.J. Rothman, L.J. Nowicki, G.E. Murch, Self-diffusion in austenitic Fe-Cr-Ni alloys, Journal of Physics F: Metal Physics, 10 (1980) 383.

[111] D. Caplan, P.E. Beaubien, M. Cohen, Effect of Manganese on the High-Temperature Oxidation of Fe-26Cr Alloy, Transactions of the Metallurgical Society of AIME, AIME, 1965, pp. 766.

[112] F.H. Stott, F.I. Wei, C.A. Enahor, The influence of manganese on the High-temperature oxidation of iron-chromium alloys, Materials and Corrosion,

40 (1989) 198-205.

[113] V.K. Ledjeff, A. Rahmel, M. Schorr, Oxidation and Carburization of High Alloyed Materials for Cracking Tubes Part 1: The Oxidation Behaviour in Air, Materials and Corrosion, 30 (1979) 767-784.

[114] P. Kofstad, K.P. Lillerud, On High Temperature Oxidation of Chromium: II . Properties of and the Oxidation Mechanism of Chromium, Journal of The Electrochemical Society, 127 (1980) 2410-2419.

[115] R.E. Lobnig, H.P. Schmidt, K. Hennesen, H.J. Grabke, Diffusion of cations in chromia layers grown on iron-base alloys, Oxidation of Metals, 37 (1992) 81-93.

[116] F.H. Stott, Influence of alloy additions on oxidation, Materials Science and Technology, 5 (1989) 734-740.

[117] A.F. Smith, The oxidation of 18/8 type stainless steel in high pressure CO_2/2% CO, Materials and Corrosion, 32 (1981) 1-7.

[118] J. Ehlers, D.J. Young, E.J. Smaardijk, A.K. Tyagi, H.J. Penkalla, L. Singheiser, W.J. Quadakkers, Enhanced oxidation of the 9%Cr steel P91 in water vapour containing environments, Corrosion Science, 48 (2006) 3428-3454.

[119] E.W. Hart, On the role of dislocations in bulk diffusion, Acta Metallurgica, 5 (1957) 597.

[120] A. Atkinson, Diffusion along grain boundaries and dislocations in oxides, alkali halides and carbides, Solid State Ionics, 12 (1984) 309-320.

[121] B. Fultz, H.N. Frase, Grain boundaries of nanocrystalline materials - their widths, compositions, and internal structures, Hyperfine Interactions, 130 (2000) 81-108.

[122] R.A. Perkins, R.A. Padgett, N.K. Tunali, Tracer diffusion of ^{59}Fe and ^{51}Cr in Fe-17 Wt Pet Cr-12 Wt Pet Ni austenitic alloy, Metallurgical Transactions, 4 (1973) 2535-2540.

[123] I. Kaur, W. Gust, Fundamentals of Grain and Interface Boundary Diffusion, Ziegler Press Stuttgart, Chichester 1989.

[124] D.P. Whittle, G.C. Wood, Chromium Oxide Scale Growth on Iron-Chromium Alloys: II. Influence of Alloy Composition, Journal of The Electrochemical Society, 115 (1968) 133-142.

[125] M.P. Brady, Y. Yamamoto, M.L. Santella, B.A. Pint, Effects of minor alloy additions and oxidation temperature on protective alumina scale formation in creep-resistant austenitic stainless steels, Scripta Materialia, 57 (2007) 1117-1120.

[126] R.L. Higginson, B. Roebuck, E.J. Palmiere, Texture development in oxide scales on steel substrates, Scripta Materialia, 47 (2002) 337-342.

[127] R.Y. Chen, W.Y.D. Yuen, Review of the High-Temperature Oxidation of Iron and Carbon Steels in Air or Oxygen, Oxidation of Metals, 59 (2003) 433-468.

[128] J.-Y. Kang, D.H. Kim, S.-I. Baik, T.-H. Ahn, Y.-W. Kim, H.N. Han, K.H. Oh, H.-C. Lee, S.H. Han, Phase Analysis of Steels by Grain-averaged EBSD

Functions, ISIJ International, 51 (2011) 130-136.

[129] M.M. Nowell, S.I. Wright, Phase differentiation via combined EBSD and XEDS, Journal of microscopy, 213 (2004) 296-305.

[130] D. Dingley, Progressive steps in the development of electron backscatter diffraction and orientation imaging microscopy, Journal of microscopy, 213 (2004) 214-224.

[131] D.J. Child, G.D. West, R.C. Thomson, The use of combined three-dimensional electron backscatter diffraction and energy dispersive X-ray analysis to assess the characteristics of the gamma/gamma-prime microstructure in alloy 720Li, Ultramicroscopy, 114 (2012) 1-10.

[132] T. Salge, M. Falke, D. Goran, Recent Advances in EDS and EBSD Technology: Revolutionizing the Chemical Analysis of Chondritic Meteorites at the Micro and Nanometer Scale, 42nd Lunar and Planetary Science Conference, Berlin, 2011.

[133] N. Birks, G.H. Meier, F.S. Pettit, Introduction to the High Temperature Oxidation of Metals, 2nd ed., Cambridge University Press, 2006.

[134] G.D. West, S. Birosca, R.L. Higginson, Phase determination and microstructure of oxide scales formed on steel at high temperature, Journal of microscopy, 217 (2005) 122-129.

[135] D.P. Burke, R.L. Higginson, Characterisation of multicomponent scales by electron back scattered diffraction (EBSD), Scripta Materialia, 42 (2000) 277-281.

[136] K. Sachs, C.W. Tuck, Surface oxidation of steel in industrial furnaces, in: Reheating for hot working, The Iron and Steel Institute, London, 1968, pp. 1-17.

[137] C. Issartel, H. Buscail, E. Caudron, R. Cueff, F. Riffard, S. Perrier, P. Jacquet, M. Lambertin, Influence of nitridation on the oxidation of a 304 steel at 800 °C, Corrosion Science, 46 (2004) 2191-2201.

[138] L. Tan, Y. Yang, T.R. Allen, Oxidation behavior of iron-based alloy HCM12A exposed in supercritical water, Corrosion Science, 48 (2006) 3123-3138.

[139] B.-K. Kim, J.A. Szpunar, Orientation imaging microscopy for the study on high temperature oxidation, Scripta Materialia, 44 (2001) 2605-2610.

[140] L. Tan, M.T. Machut, K. Sridharan, T.R. Allen, Corrosion behavior of a ferritic/martensitic steel HCM12A exposed to harsh environments, Journal of Nuclear Materials, 371 (2007) 161-170.

[141] S. Birosca, D. Dingley, R.L. Higginson, Microstructural and microtextural characterization of oxide scale on steel using electron backscatter diffraction, Journal of microscopy, 213 (2004) 235-240.

[142] J.C. Rosser, M.I. Bass, C. Cooper, T. Lant, P.D. Brown, B.J. Connolly, H.E. Evans, Steam oxidation of Super 304H and shot-peened Super 304H, Materials at High Temperatures, 29 (2012) 95-106.

[143] Y. Kondo, Behaviour of Copper during High Temperature Oxidation of Steel Containing Copper, ISIJ International, 44 (2004) 1576-1580.

[144] Y. Kondo, Behaviour of Copper and Nickel during High Temperature Oxidation of Steel Containing Them, Materials Science Forum, High-Temperature Oxidation and Corrosion 2005 (2006) 53-60.

[145] K.T. Jacob, K. Fitzner, C.B. Alcock, Activities in the spinel solid solution, phase equilibria and thermodynamic properties of ternary phases in the system Cu-Fe-O, MTB, 8 (1977) 451-460.

[146] R. Viswanathan, W. Bakker, Materials for ultrasupercritical coal power plants - Boiler materials: Part 1, Journal of Materials Engineering and Performance, 10 (2001) 81-95.

[147] T. Sourmail, Precipitation in creep resistant austenitic stainless steels, Materials Science and Technology, 17 (2001) 1-14.

[148] Q. Wu, J. Zhang, Y. Sun, Oxidation behavior of TiC particle-reinforced 304 stainless steel #5(31), Corrosion Science, 52 (2010) 1003-1010.

[149] J.-H. Kim, B.K. Kim, D.-I. Kim, P.-P. Choi, D. Raabe, K.-W. Yi, The role of grain boundaries in the initial oxidation behavior of austenitic stainless steel containing alloyed Cu at 700 ℃ for advanced thermal power plant applications, Corrosion Science, 96 (2015) 52-66.

[150] F.J. Pérez, M.J. Cristóbal, M.P. Hierro, F. Pedraza, G. Arnau, T.P. Merino, Effect of yttrium and erbium ion implantation on the oxidation behaviour of the AISI 304 austenitic steel, Surface and Coatings Technology, 126 (2000) 116-122.

[151] Z. Nishiyama, X-ray investigation on the mechanism of the

transformation from face-centered cubic lattice to body-centered cubic lattice, Science Reports of the Research Institutes, Tohoku Univ., 185 (1934) 637-664.

[152] G. Wasserman, Ueber den Mechanismus der α-γ-Umwandlung des Eisens, Mitt. K.-Wilh.Inst. Eisenforsch., 17 (1935) 149-155.

[153] H. Li, S. Xia, W. Liu, T. Liu, B. Zhou, Atomic scale study of grain boundary segregation before carbide nucleation in Ni-Cr-Fe Alloys, Journal of Nuclear Materials, 439 (2013) 57-64.

[154] W.Z. Zhu, S.C. Deevi, Opportunity of metallic interconnects for solid oxide fuel cells: a status on contact resistance, Mater. Res. Bull., 38 (2003) 957-972.

[155] H.S. Seo, G. Jin, J.H. Jun, D.-H. Kim, K.Y. Kim, Effect of reactive elements on oxidation behaviour of Fe-22Cr-0.5Mn ferritic stainless steel for a solid oxide fuel cell interconnect, J. Power Sources, 178 (2008) 1-8.

[156] S.J. Geng, J.H. Zhu, Z.G. Lu, Evaluation of several alloys for solid oxide fuel cell interconnect application, Scripta Materialia, 55 (2006) 239-242.

[157] T. Horita, H. Kishimoto, K. Yamaji, Y. Xiong, N. Sakai, M.E. Brito, H. Yokokawa, Effect of grain boundaries on the formation of oxide scale in Fe-Cr alloy for SOFCs, Solid State Ionics, 179 (2008) 1320-1324.

[158] S.H. Hong, M.P. Phaniraj, D.-I. Kim, J.-P. Ahn, Y.W. Cho, S.H. Han, H.N. Han, Improvement in Oxidation Resistance of Ferritic Stainless Steel by Carbon Ion Implantation, Electrochem. Solid State Lett., 13 (2010) B40-B42.

[159] Z. Yang, G.-G. Xia, G.D. Maupin, J.W. Stevenson, Conductive protection

layers on oxidation resistant alloys for SOFC interconnect applications, Surface and Coatings Technology, 201 (2006) 4476-4483.

[160] Z. Lu, J. Zhu, E.A. Payzant, M.P. Paranthaman, Electrical Conductivity of the Manganese Chromite Spinel Solid Solution, Journal of the American Ceramic Society, 88 (2005) 1050-1053.

[161] H. Kurokawa, C.P. Jacobson, L.C. DeJonghe, S.J. Visco, Chromium vaporization of bare and of coated iron-chromium alloys at 1073 K, Solid State Ionics, 178 (2007) 287-296.

[162] J. Froitzheim, G.H. Meier, L. Niewolak, P.J. Ennis, H. Hattendorf, L. Singheiser, W.J. Quadakkers, Development of high strength ferritic steel for interconnect application in SOFCs, J. Power Sources, 178 (2008) 163-173.

[163] N. Shaigan, W. Qu, D.G. Ivey, W. Chen, A review of recent progress in coatings, surface modifications and alloy developments for solid oxide fuel cell ferritic stainless steel interconnects, J. Power Sources, 195 (2010) 1529-1542.

[164] U. Dahmen, Orientation relationships in precipitation systems, Acta Metallurgica, 30 (1982) 63-73.

[165] P. Kofstad, Nonstoichiometry, diffusion, and electrical conductivity in binary metal oxides. , illustrated ed., Wiley-Interscience, 1972.

[166] A. Holt, P. Kofstad, Electrical conductivity and defect structure of Cr_2O_3. II. Reduced temperatures (< 1000 ℃), Solid State Ionics, 69 (1994) 137-143.

[167] N. Sakai, T. Horita, Y.P. Xiong, K. Yamaji, H. Kishimoto, M.E. Brito, H. Yokokawa, T. Maruyama, Structure and transport property of manganese-

chromium-iron oxide as a main compound in oxide scales of alloy interconnects for SOFCs, Solid State Ionics, 176 (2005) 681-686.

국문 초록

에너지 분야에서 효율을 높이기 위해 고민되는 여러 가지 시도 중 가장 쉽게 접근할 수 있는 방법으로는 시스템의 작동 온도를 높임으로써 연소 또는 변환 효율을 높이려는 시도를 들 수 있다.

전 세계적으로 가장 많은 발전량을 갖고 있는 화력발전에서는 수증기 온도를 700 ℃ 이상으로 올림으로써 발전 효율을 48%까지 끌어 올리는 차세대 화력발전소인 초초임계압 화력발전소의 개발이 이루어지고 있다. 화력발전소에 사용되는 보일러는 과열기/재열기, 절탄기 및 수냉벽으로 구성되어 있으며, 이들은 많은 파이프로 구성되어 있다. 파이프는 보일러에 사용되는 설비에 가장 핵심이 되는 부품으로 내부에 유체가 흐르고 외부에서 전달되는 열을 내부의 유체에 전달하는 주요한 역할을 하며, 이러한 파이프는 보일러가 대용량화 되어감에 따라, 점차 많은 양의 파이프가 배치된다. 기존 연구에 의하면 오스테나이트 스테인리스 강에 구리를 첨가하면 크리프 강도가 증가하고, 고온 내식성이 향상된다고 보고되고 있다. 이러한 오스테나이트 스테인리스 강은 우수한 고온 크리프 특성으로 차세대 화력발전소인 초초임계압 화력발전소의 과열기와 재열기 안에 스팀 파이프로 고려되고 있다. 하지만, 지난 몇 년 동안 고온

에서 내열강의 산화층 분석은 광범위하게 연구되었으며, 이는 극한 환경에서의 내열강 표면에 산화물의 박리로 인한 여러 가지 문제가 발생하였기 때문이다.

세계적인 에너지 문제 해결을 위한 청정 신재생 에너지원으로 다양한 종류의 연료전지 시스템 중 800 ℃ 부근에서 작동하는 고체연료 산화물 연료전지가 높은 효율과 탄력적인 연료 사용성으로 큰 관심을 받고 있다. 고체 산화물 연료전지 분리판용 재료는 가공성과 가격을 이유로 기존의 세라믹재료에서 금속재료로 빠르게 대체되고 있다. 페라이트계 스테인리스 강은 생성되는 산화물의 높은 전기전도도 뿐 아니라 소재 자체의 뛰어난 기계적 특성, 가공성, 경제성 및 다른 고체연료 산화물 연료전지 구성요소와 유사한 열팽창계수로 인해 분리판용 소재로 크게 각광받고 있다. 고체연료 산화물 연료전지의 작동온도는 650~800 ℃ 이며 이러한 온도에서 주요 관심사는 내산화성과 산화물의 형성으로 인한 전기전도도이다. 일반적으로 내산화성 개선을 위해서는 티타늄, 알루미늄등의 합금원소가 첨가되며 특히 망간은 페라이트 스테인리스 강에서 생성되는 산화물층의 전기전도도를 증가 시키기 위한 합금원소로 사용되고 있다.

이와 같은 고온 작동 조건에서 가장 문제가 되는 부분은 재

료의 고온 안정성 문제로, 특히 고온 산화에 의한 재료의 열화를 극복하는 것이 가장 중요한 이슈 중 하나이다. 이러한 고온 산화 문제를 해결하기 위한 방법으로는 다양한 합금원소를 첨가함으로써 재료내의 확산을 제어하려는 접근이 주로 이루어지고 있는데, 최근 가격 절감 문제와 재료의 재활용 가능성 저하 문제로 인하여 합금 원소의 첨가를 줄이면서 기존 재료 이상의 물성을 얻고자 하는 시도가 조금씩 증가하고 있다.

본 논문에서는 기존의 소재와 같은 소재를 이용하면서도 재료의 결정립계 특성 또는 우선 결정방위를 제어함으로써 재료의 고온 내산화성을 개선할 수 있는 방안을 소개하고자 한다.

재료의 이방성이 적은 오스테나이트계 스테인리스 소재에서는 재료의 결정방위보다는 결정립계가 내산화성에 큰 영향을 미치는데, 에너지적으로 안정적인 Σ3 입계 등 특수 결정립계에서는 내산화성을 나타내지 못하지만, 15° 이상의 어긋남각을 갖는 고경각입계 주위에서는 뛰어난 내산화성을 나타내고 있으며, 결정립의 크기를 제어하는 것 만으로도 50배 이상의 산화속도 차이를 나타낼 수 있다. 따라서 결정립을 미세화 시킴으로써 내산화성을 증가 시킬 수 있으며, 결정립계를 따라 선택적 산화로 인하여 임계결정립 크기를

확인 하였다.

이에 반해 재료의 이방성이 큰 페라이트계 스테인리스 소재에서는 결정 방위가 더 큰 영향을 나타내는데, 모재의 결정학적 방위와 내산화성, 전기전도도의 관계를 이해하기 위해 {100}, {110}, {111}과 {112} 방위의 결정립에 형성된 산화물의 구조를 분석하였다. 충진도가 높은 {110} 결정면에서는 생성되는 산화물이 판상 형태를 갖는 고밀도의 산화물이 형성되는 것을 확인 할 수 있으며, 충진도가 낮은 {111} 결정면에서는 산화물의 형상이 입자 형태를 나타내고 밀도도 비교적 낮게 나타나는 것을 알 수 있었다. 따라서 모재의 {110} 결정면에서 내산화성과 전기전도도가 다른 결정면에 비해 우수하게 나타났으며, 이를 바탕으로 결정 방위 분포의 강도에 따른 내산화성과 전기전도도의 특성의 변화를 확인 하였다.

주요어: 오스테나이트 스테인리스 강, 페라이트 스테인리스 강, 고온산화, 내산화성, 결정입계, 결정방위

학 번: 2010-20589

Curriculum Vitae

Kim Ju-Heon

2juheonkim@gmail.com

+82-10-9099-4886

Education & Research Experience

Mar 2010 – Aug 2015	**Ph.D student (The Integrated MA/Ph. D Course)** Seoul National University, Department of Materials Science and Engineering Seoul, South Korea
Dec 2008 – Aug 2015	**Research Assistant / Student Researcher** Korea Institute of Science and Technology, High Temperature Energy Materials Research Center Seoul, South Korea
Aug 2013 – Jul 2014	**Guest (Visiting) Scientist** Max-Planck-Institut für Eisenforschung GmbH, Department of Microstructure Physics and Alloy Design Düsseldorf, Germany

Awards & Grants

Mar 2014 Scholarship: Deutscher Akademischer Austausch Dienst (DAAD) scholarship for doctoral candidates and young academics and scientists

Aug 2013 Scholarship: Max-Planck Institut für Eisenforschung (MPIE) scholarship

Apr 2011 Award: The Award-Winning Laboratory Notebook

Dec 2010 Award: Campus Patent Strategy Universiade

Skills and Expertise

High Temperature Oxidation, Heat Resistant Stainless Steel, Material Characterization, Grain Boundaries, Microstructure, Mechanical Properties, Mechanical Behavior of Materials, Recrystallisation, Electron Backscatter Diffraction, Atom Probe Tomography, Iron Oxidation, Structural Stability, Materials Engineering, Metallurgical Engineering, Materials, Metals, Mechanical Testing, Heat Treatment, Materials Processing, Plasticity, Advanced Materials, Dislocation Mechanics, High Temperature Materials, Tensile Testing, Crystal Plasticity, Fracture Mechanics, Failure Analysis, Light Metals, Severe Plastic Deformation, Texture Mapping, Metal Forming, Welding, Mechanics, Solidification, Casting, Materials Testing

Journal Publications

1. Hae-A-Seul Shin, Byoung-Joon Kim, ***Ju-Heon Kim***, Sung-Hwan Hwang, Arief Suriadi Budiman, Ho-Young Son, Kwang-Yoo Byun, Nobumichi Tamura, Martin Kunz, Dong-Ik Kim, Young-Chang Joo: *Microstructure Evolution and Defect Formation in Cu Through-Silicon Vias (TSVs) During Thermal Annealing*. Journal of Electronic Materials 04/2012; 41(4):712-719.

2. ***Ju-Heon Kim***, Dong-Ik Kim, Satyam Suwas, Eric Fleury, Kyung-Woo Yi: *Grain-Size Effects on the High-Temperature Oxidation of Modified 304 Austenitic Stainless Steel*. Oxidation of Metals 12/2012; 79(3-4):239-247.

3. ***Ju-Heon Kim***, Dong-Ik Kim, Jong Seok Kim, Shi-Hoon Choi, Kyung-Woo Yi, Kyu Hwan Oh: *Technical Investigation into the In-situ Electron Backscatter Diffraction Analysis for the Recrystallization Study on Extra Low Carbon Steels*. Applied Microscopy. 06/2013; 43(2):88-97.

4. ***Ju-Heon Kim***, Dong-Ik Kim, Jae-Hyeok Shim, Kyung-Woo Yi: *Investigation into the high temperature oxidation of Cu-bearing austenitic stainless steel using simultaneous electron backscatter diffraction-energy dispersive spectroscopy analysis*. Corrosion Science 12/2013; 77:397-402.

5. Sung-Jin Jung, ***Ju-Heon Kim***, Dong-Ik Kim, Seong Keun Kim, Hyung-Ho Park, Jin-Sang Kim, Dow-Bin Hyun, Seung-Hyub Baek: *Strain-assisted, low-temperature synthesis of high-performance thermoelectric materials.*. Physical Chemistry Chemical Physics 01/2014; 16(8):3529-3533.

6. D.-I. Kim, J.S. Kim, ***J.-H. Kim***, S.-H. Choi: *A study on the annealing behavior of Cu-added bake-hardenable steel using an in situ EBSD technique*. Acta Materialia 04/2014; 68:9-18.

7. Deuk-Hee Lee, Jae-Uk Lee, Sung-Jin Jung, Seung-Hyub Baek, ***Ju-Heon Kim***, Dong-Ik Kim, Dow-Bin Hyun, Jin-Sang Kim: *Effect of Heat Treatment on the Thermoelectric Properties of Bismuth-Antimony-Telluride Prepared by Mechanical Deformation and Mechanical Alloying*. Journal of Electronic Materials 06/2014; 43(6):2255-2261.

8. ***Ju-Heon Kim***, Byung Kyu Kim, Dong-Ik Kim, Pyuck-Pa Choi, Dierk Raabe, Kyung-Woo Yi: *The role of grain boundaries on the initial oxidation in Cu added austenitic stainless steels at 700 °C for advanced thermal power plant applications.* Corrosion Science 07/2015; 96:52-66.

9. M.P. Phaniraj, ***Ju-Heon Kim***, Han-Jin Kim, Young-Su Lee, Dong-Ik Kim, Jin-Yoo Suh, Jae-Hyeok Shim, Seong-Jun Park: *Effect of thermal charging of hydrogen on the microstructure of 304-type austenitic stainless steel*, International Journal of Hydrogen Energy revising.

10. ***Ju-Heon Kim***, Dong-Ik Kim, Pyuck-Pa Choi, Dierk Raabe, Kyung-Woo Yi: *Atomic scale observations of Phase transformations (FCC→BCC) along the grain boundary during oxidation of Cu added Austenite stainless steel at 700 ℃,* in preparation.

11. ***Ju-Heon Kim***, Dong-Ik Kim, Kyung-Woo Yi: *Effect of Crystallographic Orientation on Oxidation Resistance and Electrical Conductivity of Ferritic Stainless Steel for SOFC interconnect,* in preparation.

Patents

1. 내산화성 페라이트계 스테인리스강, 그 제조 방법 및 이를 사용한 연료 전지 접속자 (Ferritic stainless steel with excellent oxidation resistance, manufacturing method thereof and fuel cell interconnector using the same), KR20110080650A (KOR), 13/227,987 (USA), 11180707.9 (EU), 08/2011.

2. 내산화성 페라이트계 스테인리스강, 그 제조 방법 및 이를 사용한 연료 전지 접속자 (Oxidation resistant ferritic stainless steel, method of manufacturing the steel, and fuel cell interconnect using the steel), KR20120118679A(KOR), 13/686,124(USA) 10/2012.

Conference (International)

1. ***Ju-Heon Kim***, Dong-Ik Kim, Satyam Suwas, Eric Fleury, Kyung-Woo Yi: *Grain-Size Effects on the High-Temperature Oxidation of Cu added Austenitic stainless steel*, POSTER, 8th International Symposium on High-Temperature Corrosion and Protection of Materials (HTCPM), 20-25th of May 2012, Les Embiez (Var), FRANCE.

2. ***Ju-Heon Kim***, Byung Kyu Kim, Dong-Ik Kim, Pyuck-Pa Choi, Dierk Raabe, Kyung-Woo Yi: *The Role of Grain Boundaries during the Initial Oxidation Stages in Cu added Austenitic Stainless Steel at 700 °C Studied at the Atomic Scale,* ORAL, 227th ECS Meeting, 24-28th of May 2015, Chicago, Illinois, USA.